



The  
University  
Of  
Sheffield.

# **Micro-structural and optical investigation of semi-polar (11-22) III-nitrides overgrown on regularly arrayed micro-rods**

**By:**

Yun Zhang

A thesis submitted in partial fulfilment of the requirements for the degree of  
Doctor of Philosophy

The University of Sheffield  
Department of Electronic and Electrical Engineering

August 2017



# Abstract

---

This project aims to systematically study the micro-structure and optical properties of semi-polar (11-22) GaN with a step-change in crystal quality achieved by means of overgrowth on regularly arrayed micro-rods. The optical properties of (11-22) InGaN-based quantum wells grown on such high quality GaN templates have been investigated in comparison with their *c*-plane counterparts.

The overgrowth of semi-polar (11-22) GaN grown is performed using a metal organic chemical vapour deposition (MOCVD) technique on specially designed micro-rod arrays on standard *m*-plane sapphire. Owing to the specially designed patterns of the micro-rod template, our overgrowth technique effectively mitigates the intrinsic issue of the anisotropic lateral growth rate. Thanks to the massive overgrowth work of semi-polar (11-22) GaN on sapphire which were mainly carried out by Dr. Yipin Gong, I have the chance to investigate the defect reduction mechanism in details by using transmission electron microscopy (TEM) measurements. It has been found that most of the dislocations and the basal stacking faults (BSFs) have been effectively blocked by the SiO<sub>2</sub> masks on each micro-rod and then the coalescence processes during the overgrowth. By favouring the growth along the *c*-direction (the *c*-direction growth leads to free-defect, while the defects can be penetrated through the growth along the *a*-direction), the defects as a result of the growth along the *a*-direction could be blocked. As a type of two-dimensional defect, BSFs can expand within the basal plane, propagating with a component parallel the *m*-direction. This leads to a distribution of BSF-free regions periodically separated by the BSF regions along the [-1-123] direction. Furthermore, each BSF region typically consists of low density BSF clusters and high density BSF clusters with a periodic distribution along the *m*-direction. Finally, a defect reduction model has been established in order to study the influence of the micro-patterning on defect reduction.

Further investigation was also carried out on the influence of micro-rod diameter on the crystal quality of overgrown semi-polar (11-22) GaN in order to optimize our micro-rod design. It has been found that the BSF density decreases monotonically with increasing micro-rod diameter from 2 to 5  $\mu\text{m}$ , and then starts to be saturated when the micro-rod

diameter further increases. However, the dislocation density reduces significantly when the micro-rod diameter increases from 2 to 4  $\mu\text{m}$ , and then increases slightly with further increasing the diameter to 5  $\mu\text{m}$ . In addition, it has been found that it is effective to employ shorter micro-rods to further reduce BSFs, allowing for further improvement in crystal quality. The best crystal quality of the overgrown (11-22) GaN has been achieved by overgrowth on micro-rods with a 4  $\mu\text{m}$  diameter and a 0.4  $\mu\text{m}$  height, corresponding to a dislocation density of  $2.0 \times 10^8 \text{ cm}^{-2}$  which is better or at least equivalent to standard *c*-plane GaN with a similar thickness grown on *c*-plane sapphire. The best sample achieved so far exhibits a BSF density of  $2.8 \times 10^4 \text{ cm}^{-1}$ .

In this project, a number of advance optical characterization methods have been performed on a large number of semi-polar (11-22) InGaN/GaN MQWs with a wide spectral range of up to yellow spectra region grown on high quality semi-polar GaN, aiming to systemically investigate the mechanisms which form the large Stokes shift that generally occurs to InGaN/GaN MQWs. This is a long-standing issue. The semi-polar (11-22) samples exhibit a lower Stokes shift than their *c*-plane counterparts, although they show larger exciton localization than their *c*-plane counterparts. The Stokes shift in the semi-polar samples shows a linear relationship with the emission energy in long wavelength region, but with a smaller gradient compared with that in the *c*-plane counterparts. The time-resolved photoluminescence (PL) measurements reveal a significant reduction in the piezoelectric fields of the semi-polar sample. It is suggested that the piezoelectric field induced polarization is the major mechanism for causing the large Stokes shift in conventional *c*-plane InGaN/GaN MQWs.

At the same time, room temperature confocal PL measurements with a high spatial resolution have been performed on the high quality semi-polar (11-22) InGaN/GaN SQW samples overgrown on regularly arrayed micro-rods, aiming to investigate the influence of BSFs on the optical properties of the semi-polar InGaN/GaN SQW. The results clearly show that unlike dislocations, BSFs don't affect the optical properties significantly.

# List of publications

---

## Journal publications

1. B. Xu, L. Jiu, Y. Gong, **Y. Zhang**, L. C. Wang, J. Bai, and T. Wang  
*Stimulated emission from semi-polar (11-22) GaN overgrown on sapphire*  
AIP Advances **7**, 045009 (2017)
2. Z. Li, L. Wang, L. Jiu, J. Bruckbauer, Y. Gong, **Y. Zhang**, J. Bai, R. Martin, and T. Wang,  
*Optical Investigation of Semi-polar (11-22) Al<sub>x</sub>Ga<sub>1-x</sub>N with High Al Composition*  
Appl. Phys. Lett. **110**, 091102 (2017)
3. Z. Li, L. Jiu, Y. P. Gong, L. Wang, **Y. Zhang**, J. Bai and T. Wang,  
*Semi-polar (11-22) AlGa<sub>N</sub> on overgrown GaN on micro-rod templates: simultaneous management of crystal quality improvement and cracking issue*  
Appl. Phys. Lett. **110**, 082103 (2017)
4. **Y. Zhang**, J. Bai, Y. Hou, X. Yu, Y. Gong, R. M. Smith, and T. Wang,  
*Microstructure investigation of semi-polar (11-22) GaN overgrown on different designed micro-rod array templates*  
Appl. Phys. Lett. **109**, 241906 (2016)
5. X. Yu, Y. Hou, S. Shen, J. Bai, Y. Gong, **Y. Zhang** and T. Wang,  
*Semi-polar (11-22) GaN grown on patterned (113) Si substrate*  
Phys. Status Solidi C, **13**: 190–194 (2016)
6. **Y. Zhang**, J. Bai, Y. Hou, R. M. Smith, X. Yu, Y. Gong, and T. Wang,  
*Defect reduction in overgrown semi-polar (11-22) GaN on a regularly arrayed microrod array template*  
AIP Advances **6**, 025201 (2016)
7. **Y. Zhang**, R. M. Smith, Y. Hou, B. Xu, Y. Gong, J. Bai, and T. Wang,  
*Stokes shift in semi-polar (11-22) InGa<sub>N</sub>/Ga<sub>N</sub> multiple quantum wells.*  
Appl. Phys. Lett. **108**, 031108 (2016).
8. Z. Zhuang, X. Guo, B. Liu, F. Hu, J. Dai, **Y. Zhang**, Y. Li, T. Tao, T. Zhi, Z. Xie, H. Ge, X. Wang, M. Xiao, T. Wang, Y. Shi, Y. Zheng, and R. Zhang,  
*Great enhancement in the excitonic recombination and light extraction of highly ordered InGa<sub>N</sub>/Ga<sub>N</sub> elliptic nanorod arrays on a wafer scale,*  
Nanotechnology, **27**, 015301 (2016).
9. M. Athanasiou, R. M. Smith, Y. Hou, **Y. Zhang**, Y. Gong, and T. Wang,  
*Enhanced polarization of (11-22) semi-polar InGa<sub>N</sub> nanorod array structure,*  
Appl. Phys. Lett. **107**, 141110 (2015).
10. J. Bai, X. Yu, Y. Gong, Y. N. Hou, **Y. Zhang** and T. Wang,

*Growth and characterization of semi-polar (11-22) GaN on patterned (113) Si substrates*,  
Semicond. Sci. Technol. **30**, 065012 (2015).

### Conference contributions

1. B. Xu, **Y. Zhang**, L. Jiu, Y. Gong, L. C. Wang, J. Bai and T. Wang  
*Stimulated Emission from Semi-polar (11-22) GaN Overgrown on Sapphire*  
UK Nitrides Consortium (UKNC) Winter Conference, Oxford, UK (2017).
2. **Y. Zhang**, X. Yu, K. Xing, Y. Gong, J. Bai, R. M. Smith and T. Wang,  
*Overgrowth and Microstructural Investigation of Semi-Polar (11-22) GaN on Arrayed Micro-Rods with Different Diameters*.  
International Workshop on Nitride Semiconductors, Orlando, US. (Oct. 2016) [poster]
3. **Y. Zhang**, X. Yu, K. Xing, Y. Gong, J. Bai, R. M. Smith, T. Wang,  
*Microstructure investigation of semipolar (11-22) GaN overgrown on different size micro-rod array templates*.  
UK Nitrides Consortium (UKNC) Summer Conference, Sheffield, UK (2016).
4. **Y. Zhang**, F. Guzman, B. Xu, X. Yu, Y. Gong, Y. Hou, J. Bai, and T. Wang,  
*Long wavelength semi-polar InGaN LEDs from green to amber overgrown on regularly arrayed micro-rod templates*,  
Semiconductor and Integrated OptoElectronics (SIOE) Conference, Cardiff, UK (2016).
5. **Y. Zhang**, J. Bai, B. Xu, K. Xing, X. Yu, Y. Gong, Y. Hou, and T. Wang,  
*(11-22) semipolar InGaN emitters from green to amber overgrown on GaN micro-rod templates*.  
UK Nitrides Consortium (UKNC) Winter Conference, Cambridge, UK (2016).
6. **Y. Zhang**, J. Bai, R. M. Smith, Y. Hou, Y. Gong, and T. Wang,  
*Defect Reduction in the Overgrown (11-22) GaN Layer on Regularly Arrayed Microrod Templates*.  
International Workshop on Future Light Technology and Human Health, University of Surrey, Guildford, UK, (21-22 September 2015)
7. **Y. Zhang**, R.M. Smith, B. Xu, Y. Hou, Y. Gong, and T. Wang,  
*Stokes Shift In (11-22) Green To Yellow Emitting Semi-Polar InGaN/GaN Multiple Quantum Wells*  
the 11th International Conference on Nitride Semiconductors (ICNS-11), Beijing, China (2015). [poster]
8. **Y. Zhang**, R. Smith, B. Xu, Y. Hou, Y. Gong and T. Wang,  
*Stokes Shift in (11-22) Semi-polar InGaN/GaN Multiple Quantum Wells On Overgrown Semi-polar GaN*,  
UK Nitrides Consortium (UKNC) Winter Conference, Nottingham, UK (2015).
9. Y. Hou, R. Smith, **Y. Zhang**, J. Bai and T. Wang,  
*Influence of nanorod diameter on InGaN/GaN nanorod based hybrid plasmonic nanolaser*  
UK Nitrides Consortium (UKNC) Summer Conference, Sheffield, UK (2014).

# Contents

---

## Abstract

## List of publications

## Contents

### Chapter 1

Introduction .....	1
1.1 Introduction.....	1
1.2 Challenges in III-nitrides .....	3
1.2.1 Quantum Confined Stark Effect .....	3
1.2.2 Green/Yellow Gap.....	4
1.2.3 Efficiency Droop .....	5
1.2.4 Defect issues .....	6
1.3 Motivation.....	7
1.4 Thesis outline .....	8
References.....	9

### Chapter 2

Background .....	11
2.1 Introduction of III-nitrides .....	11
2.1.1 Crystal structure.....	11
2.1.2 Spontaneous and piezoelectric polarization .....	13
2.1.3 Band Structure .....	14
2.2 Prospects of semi-polar and non-polar III-nitrides .....	16
2.2.1 Semi-polar and non-polar orientations .....	16
2.2.2 Reduced or eliminated piezoelectric field .....	18
2.2.3 Indium incorporation .....	19
2.2.4 Doping .....	19
2.2.5 Development of semi-polar and non-polar III-nitrides.....	20
2.3 Heteroepitaxy of semi-polar and non-polar III-nitrides.....	23

2.3.1	Substrates for heteroepitaxy.....	23
2.3.2	Growth techniques for improving crystal quality .....	25
2.4	Defects in semi-polar and non-polar III-nitrides.....	29
2.4.1	Defect type .....	29
2.4.2	Defect observation techniques .....	32
2.4.3	Initiation, propagation and termination of defects.....	34
2.5	Optical properties of semi-polar and non-polar III-nitrides .....	35
2.5.1	Radiative recombination and non-radiative recombination.....	35
2.5.2	Stokes shift in III-nitrides .....	37
2.5.3	Carrier dynamics in InGaN/GaN MQWs along a semi-polar or non-polar orientation.....	39
	References .....	45

### Chapter 3

	Experimental techniques.....	53
3.1	Optical characterization.....	53
3.1.1	Photoluminescence .....	53
3.1.2	Photoluminescence excitation.....	54
3.1.3	Time-resolved photoluminescence .....	56
3.1.4	Confocal microscopy .....	58
3.2	Transmission electron microscopy characterization .....	60
3.2.1	Transmission electron microscopy .....	60
3.2.2	Specimen preparation.....	62
3.3	Metal organic chemical vapour deposition .....	65
3.4	Micro-rod template overgrowth approach.....	66
	References .....	68

### Chapter 4

	Defect reduction in overgrown semi-polar (11-22) GaN on a regularly arrayed micro-rod array template.....	69
4.1	Introduction .....	69
4.2	Overgrowth process.....	70
4.3	Defect reduction mechanism.....	72

4.3.1	Dislocation reduction during the overgrowth .....	72
4.3.2	BSF reduction during the overgrowth .....	75
4.4	Defect reduction model.....	78
4.5	Summary .....	82
	References.....	83

## Chapter 5

	Microstructure investigation of semi-polar (11-22) GaN overgrown on differently designed micro-rod array templates .....	85
5.1	Introduction.....	85
5.2	BSF reduction with different micro-rod sizes.....	87
5.2.1	BSF reduction with different micro-rod diameters.....	87
5.2.2	BSF reduction with different micro-rod heights.....	90
5.3	Dislocation reduction with different micro-rod sizes .....	93
5.4	Summary .....	98
	References.....	99

## Chapter 6

	Stokes Shift in Semi-polar (11-22) InGaN/GaN Multiple Quantum Wells .....	101
6.1	Introduction.....	101
6.2	Stokes shift in semi-polar (11-22) MQWs.....	103
6.2.1	Semi-polar (11-22) InGaN/GaN MQWs .....	103
6.2.2	Stokes shift .....	104
6.2.3	QCSE in InGaN/GaN MQWs .....	107
6.2.4	Localization in InGaN/GaN MQWs.....	109
6.3	Summary .....	111
	References.....	112

## Chapter 7

	Confocal photoluminescence investigation on semi-polar (11-22) InGaN/GaN single quantum well overgrown on regularly arrayed micro-rods.....	115
7.1	Introduction.....	115
7.2	Results and discussion .....	117
7.3	Summary .....	123

References ..... 125

**Chapter 8**

Summary and future work..... 127

8.1 Summary ..... 127

8.2 Future work ..... 129

8.2.1 Defect reduction in non-polar *a*-plane GaN overgrown on regularly arrayed micro-rod template ..... 129

8.2.2 Optical characterization of semi-polar (11-22) InGaN/GaN single quantum well by using a novel nano-patterning approach ..... 130

**Abbreviations**

**Acknowledgements**

## Introduction

---

### 1.1 Introduction

Electricity plays an essential role in many aspects of human's daily lives, such as lighting, heating, industry, transport, communication, etc. The last few decades have seen an exponential increase in electricity consumption as a result of industrial development and population growth. To meet the significantly increasing demand on electricity, more fossil fuels including coal, natural gas and petroleum have had to be used in order to produce more electricity, leading to an acceleration in worsening environment and thus threatening human's viability. This has posed a number of global challenges, such as global warming, extreme weather occurring globally and regularly, acid rain, water and air pollution, etc. Therefore, it is becoming increasingly urgent to develop new technologies for efficient consumption of energy and sustainable energy sources.

One of the major sources for electricity consumption across the world is due to lighting. An incandescent light bulb, which was invented in the late 19<sup>th</sup> century, exhibits 16 lm/W, which is equivalent to a luminous efficiency of around 2%.<sup>1,2</sup> This means that most of the electricity used is actually converted into heat rather than visible light. Consequently, the lifetime of incandescent light bulbs also becomes another challenge in addition to the luminous efficiency issue. In the early 20<sup>th</sup> century, fluorescent tubes appeared and then have been widely used. Compared with incandescent light bulbs, the luminous efficiency of fluorescent tubes has been significantly improved, typically reaching 70 lm/W. In the meantime, the lifetime issue has also been improved, although it is still far from satisfactory in terms of optical efficiency. The fabrication of fluorescent lamps typically involves toxic elements which are not environmentally friendly. As a result, EU have implemented a strict regulation, aiming to stop the manufacture of fluorescent tubes, in particular the least efficient and lowest performance fluorescent tubes.

Developments in solid-state lighting (SSL) are occurring at pace. SSL is mainly based on III-nitride semiconductor light-emitting diodes (LEDs). This is expected to result in a fundamental change in the concept of illumination. In theory, the luminous efficiency of semiconductor-based LEDs can be up to 300 lm/W, which is almost 20 times higher than traditional incandescent bulbs.<sup>3</sup> In addition to the significant energy saving, LEDs also demonstrate a number of other major advantages, such as longevity, intrinsic compactness, smart lighting, flexibility for special applications, significant reduction in maintenance cost, etc.

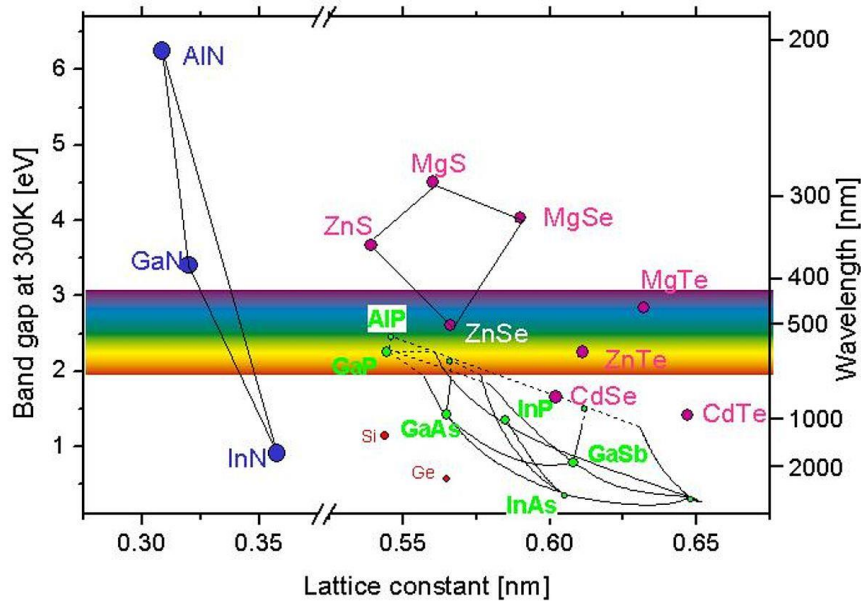


Figure 1.1: Bandgaps of semiconductors as a function of their lattice constants.<sup>5</sup>

III-nitride semiconductors, consisting of aluminum nitride (AlN), gallium nitride (GaN), indium nitride (InN) and their ternary or quaternary alloys, all exhibit direct bandgap structures. Figure 1.1 presents the bandgaps and emission wavelengths of all major semiconductor materials as a function of their lattice constants. The bandgap of III-nitride group varies from 6.0 eV (AlN), through 3.4 eV (GaN), to 0.7 eV (InN), covering a wide spectral region from the deep ultraviolet, through the whole visible range, to the infrared.<sup>6</sup> III-nitride materials with these unique properties are well suitable for visible and ultraviolet optoelectronics and high temperature & high frequency electronic devices working in harsh environments.

In the last two decades, great achievements have been made in III-nitride based LED and laser diode (LD) devices. Commercialization of GaN related white LEDs and blue LDs have been realized in the areas of general illumination, display and data storage. In 2014, the Nobel

Prize in Physics was jointly awarded to Isamu Akasaki, Hiroshi Amano and Shuji Nakamura for their great contributions to the invention of efficient blue LEDs which has enabled bright and energy-saving white light sources.<sup>7</sup>

## 1.2 Challenges in III-nitrides

The last two decades have seen unprecedented developments in the field of III-nitride optoelectronics. However, most of the achievements are limited to *c*-plane (0001) GaN. This polar orientation poses a number of fundamental limitations, hampering the further development and commercial application of GaN-based optoelectronics, in particular longer wavelength emitters in the green and yellow spectral region.

### 1.2.1 Quantum Confined Stark Effect

Generally speaking, an InGaN/GaN quantum well structure grown along the *c*-direction suffers from a compressive strain due to the large lattice mismatch between the InGaN quantum well and the GaN barrier. As a result, polarization fields which are parallel to the growth direction are introduced to the strained InGaN quantum well layers. The resultant built-in electric phenomenon generate the so-called “Quantum Confined Stark Effect” (QCSE).<sup>8</sup>

One of the direct consequences of the QCSE is due to the reduced overlap between electron-hole wave-functions, as shown in Figure 1.2. It is well-known that a radiative recombination rate is proportional to the square of the overlap between electron and hole wave-functions. Consequently, the QCSE is expected to lead to a reduction in optical efficiency. Furthermore, the QCSE also brings down the energy levels of electrons and holes, lowering the transitional energy between electrons and holes.<sup>8</sup>

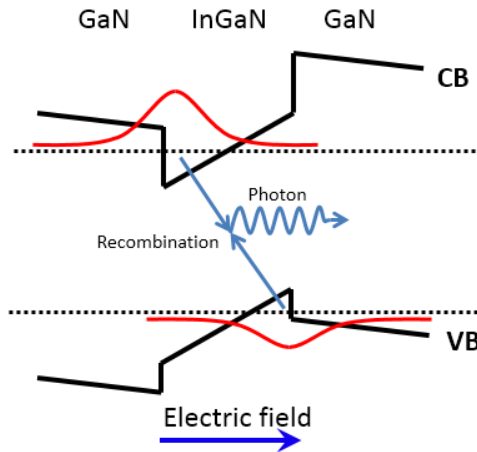


Figure 1.2: Band diagram of a *c*-plane InGaN/GaN quantum well suffering polarization induced electric fields.

### 1.2.2 Green/Yellow Gap

An emission wavelength from a ternary InGaN-based structure can be tuned via altering its alloy composition. Higher indium composition is required in order to achieve longer emission wavelengths such as green and yellow emission. However, the quantum efficiency of InGaN-based LEDs drops rapidly with increasing emission wavelength as described in Figure 1.3, where InGaN-based LEDs exhibit a reduction in optical efficiency with increasing emission wavelength, in particular in the green and yellow spectral region. On the other hand, the optical efficiency of AlGaInP which can also be used for the fabrication of visible LEDs decreases with decreasing emission wavelength, and drops down significantly when they approach the green and yellow spectral region. Consequently, a gap in the green and yellow spectral region in terms of optical efficiency has been generated, which is the so-called "green/yellow gap".

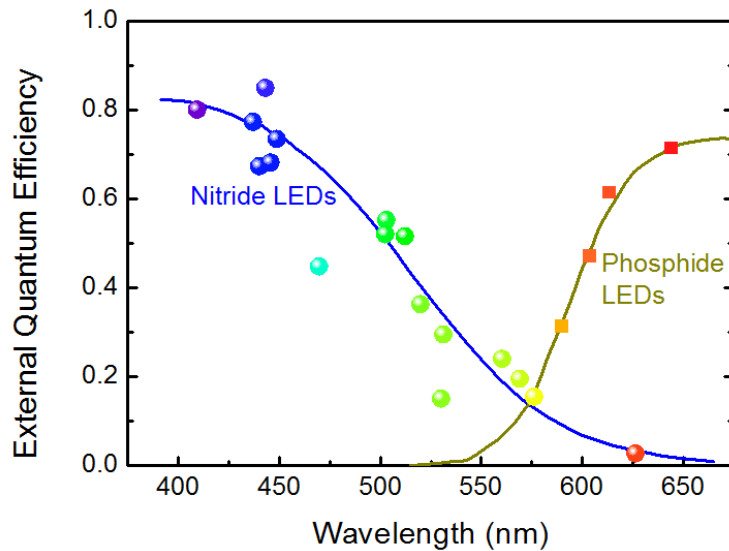


Figure 1.3: External quantum efficiency of commercial LEDs reported in the recent years.<sup>10</sup> The lines are guides to the eye.

Currently, white LEDs which are commercially available are achieved by combining a blue LED and a down-conversion yellow phosphor.<sup>9</sup> Such a white LED exhibits a number of drawbacks, such as a low colour rendering index and down-conversion energy loss. An important, but often neglected, issue for the fabrication of phosphor-conversion white LEDs is due to the self-absorption of the phosphor involved in producing the white light. This puts additional limits on the overall efficiency and also further affects the colour rendering. To meet the demand of a high colour rendering index for general illumination, a mixture of blue, green and red lights from high efficiency LEDs is the best option, which can replicate the white light from the Sun. However, the missing component is due to highly efficient green LEDs

### 1.2.3 Efficiency Droop

The ratio of the total number of photons emitted from a LED device to the number of injected electrons under a certain current density is defined as external quantum efficiency (EQE). As an example, Figure 1.4 presents a typical EQE of a standard *c*-plane green InGaN/GaN LED with a standard size of  $300 \times 300 \mu\text{m}^2$  as a function of injection current.<sup>11</sup> The EQE initially increases with increasing injection current and then reaches a maximum value at around 3 mA, and then starts to decrease with further increasing injection current. The EQE at 100 mA is almost 59% of the peak value at 3 mA. This phenomenon has been widely

observed on almost all InGaN based LEDs grown on *c*-plane GaN, and has been referred to as "Efficiency Droop".

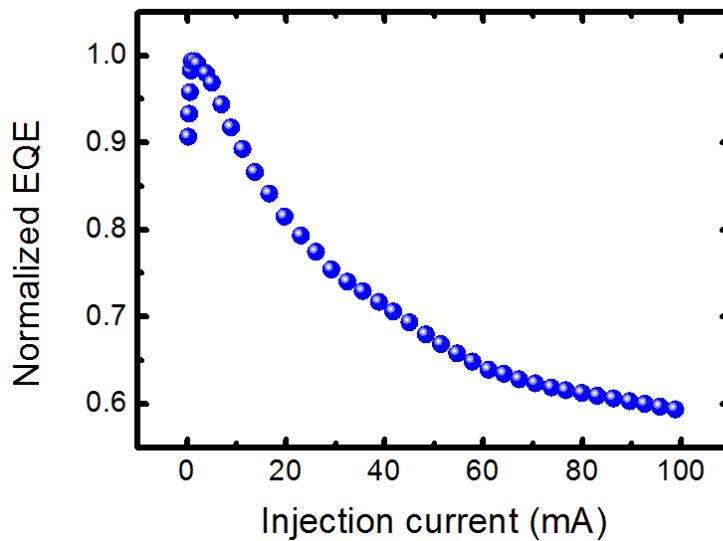


Figure 1.4: Normalized EQE of a *c*-plane green InGaN/GaN LED as a function of injection current.<sup>11</sup>

A number of mechanisms have been proposed to explain the efficiency droop, although they are still under debate, such as Auger recombination, carrier delocalization, electron overflowing, current crowding and defect-assisted tunnelling.<sup>12</sup> From recent studies, it has been suggested that Auger recombination might be the dominant mechanism for the efficiency droop.<sup>13</sup> Auger recombination is defined as a non-radiative recombination process involving three particles, where the released energy from the recombination of an electron-hole pair is re-absorbed by an additional particle (either electron or hole), leading to the third particle being excited into a higher energy level. It is crucial to overcome the efficiency droop in order to achieve high output power.

#### 1.2.4 Defect issues

Homoepitaxial growth of GaN is ideal, but is not sustainable as a result of the lack of affordable GaN substrates, in particular for the growth and fabrication of high brightness LEDs for general illumination, where the major concerns are due to high costs. Currently, GaN films are typically obtained via heteroepitaxial growth mainly on sapphire, and also on silicon as the second alternative option. Due to the large lattice-mismatch, GaN grown on sapphire GaN usually contains a high density of dislocations, typically on an order of  $10^9$ - $10^{10}$  cm<sup>-2</sup>. The

situation for GaN grown on silicon is even worse, as there is an extra issue as a result of the large difference of the thermal expansion coefficients between GaN and silicon. Nevertheless, high brightness LEDs on either sapphire or silicon have been achieved, but are limited to the blue/violet spectral region. Therefore, more efforts need to be devoted to the development of longer wavelength such as green and yellow LEDs. The growth of GaN along a semipolar or nonpolar direction has been proposed. However, the major challenge is due to the crystal quality of either semipolar or nonpolar GaN, which is far from satisfactory. It is well-known that dislocations has been generally regarded as nonradiative recombination centres, leading to a reduction in optical performance. Furthermore, it has also been found that charged dislocation lines could scatter electrons or holes limiting their transport properties.<sup>14</sup> Therefore, it is still vitally important to reduce the defect density in GaN films in order to further improve the optical performance of InGaN based emitters, which is particularly important for developing highly efficient InGaN-related emitters in the longer wavelength such as green and yellow spectral region.

### **1.3 Motivation**

To address the QCSE caused as a result of the piezoelectric fields occurring to *c*-plane InGaN/GaN based emitters, a promising approach is to grow the InGaN quantum wells along a semi-polar or non-polar orientation as mentioned above. Furthermore, it has also been predicted that efficiency droop can be potentially improved by the growth of InGaN/GaN LEDs along a semi-polar direction.<sup>15</sup> Compared with polar and non-polar GaN, semi-polar (11-22) GaN surface has been predicted to exhibit a significantly lower indium chemical potential,<sup>16</sup> potentially enhancing the incorporation of more indium into GaN, which is crucial for the realization of InGaN-based emitters in the longer wavelength spectral region. Our group have developed a number of novel but cost-effective overgrowth approaches to the growth of high quality semipolar (11-22) GaN on sapphire. The aim of the research presented in this PhD thesis is to perform structural and optical investigation of the semipolar (11-22) GaN overgrown on patterned templates, aiming to understand the mechanisms of defect reduction and then further develop high-efficiency InGaN based emitters in the longer wavelength such as green and yellow spectral region.

## 1.4 Thesis outline

This thesis is divided into 8 chapters:

Chapter 1 presents a brief introduction on the development of III-nitride semiconductors for solid-state lighting and the current challenges in developing longer wavelength emitters with high efficiency, followed by the motivation of the research for the thesis.

Chapter 2 presents the details of semi-polar and non-polar III-nitrides in terms of the crystal structure, current development, heteroepitaxial growth, defects involved and optical properties.

Chapter 3 describes a number of structural and optical characterization methods used for this thesis.

Chapter 4 presents the microstructural investigation of the semi-polar (11-22) GaN overgrown on regularly arrayed micro-rods by means of transmission electron microscopy, where the mechanism for the defect reduction has been investigated and a model has been established.

Chapter 5 provides a systematic study on the microstructure of the semi-polar (11-22) GaN overgrown on microrod templates as a function of microrod diameter, demonstrating that the reduction in dislocations exhibit a different behaviour from that for basal stacking faults (BSFs).

Chapter 6 provides a systematic investigation on the Stokes shift and exciton localization of semi-polar (11-22) InGaN/GaN multiple quantum well (MQW) structures with a wide range of indium composition, which has also been compared to their counterparts grown on *c*-plane GaN.

Chapter 7 presents a comparative study on the emission properties from the quantum well regions with and without BSFs in semi-polar (11-22) InGaN/GaN single quantum well (SQW) structures overgrown on micro-rod templates.

Chapter 8 gives a summary of presented work and an outlook for further research.

## References

- 1 P. Waltereit, O. Brandt, A. Trampert, H. Grahn, J. Menniger, M. Ramsteiner, M. Reiche, and K. Ploog, *Nature* **406**, 865 (2000).
- 2 D. C. Agrawal, H. S. Leff, and V. J. Menon, *Am. J. Phys.* **64**, 649 (1996).
- 3 S. Nakamura, *Rev. Mod. Phys.* **87**, 1139 (2015).
- 4 S. Nakamura, *Science* **281**, 956 (1998).
- 5 Compound semiconductors: Physics, technology and device concepts. <http://www-opto.e-technik.uni-ulm.de/lehre/cs/>
- 6 T. Y. Seong, J. Han, H. Amano, and H. Morkoc, *III-Nitride Based Light Emitting Diodes and Applications* (Springer Netherlands, 2013).
- 7 [https://www.nobelprize.org/nobel\\_prizes/physics/laureates/2014/](https://www.nobelprize.org/nobel_prizes/physics/laureates/2014/)
- 8 D. A. B. Miller, D. S. Chemla, T. C. Damen, A. C. Gossard, W. Wiegmann, T. H. Wood, and C. A. Burrus, *Phys. Rev. Lett.* **53**, 2173 (1984).
- 9 S. Pimputkar, J. S. Speck, S. P. DenBaars, and S. Nakamura, *Nat. Photonics* **3**, 180 (2009).
- 10 M. Auf der Maur, A. Pecchia, G. Penazzi, W. Rodrigues, and A. Di Carlo, *Phys. Rev. Lett.* **116**, 27401 (2016).
- 11 J. Bai, B. Xu, F. G. Guzman, K. Xing, Y. Gong, Y. Hou, and T. Wang, *Appl. Phys. Lett.* **107**, 261103 (2015).
- 12 G. Verzellesi, D. Saguatti, M. Meneghini, F. Bertazzi, M. Goano, G. Meneghesso, and E. Zanoni, *J. Appl. Phys.* **114**, 71101 (2013).
- 13 J. Iveland, L. Martinelli, J. Peretti, J. S. Speck, and C. Weisbuch, *Phys. Rev. Lett.* **110**, 177406 (2013).
- 14 N. G. Weimann, L. F. Eastman, D. Doppalapudi, H. M. Ng, and T. D. Moustakas, *J. Appl. Phys.* **83**, 3656 (1998).
- 15 C. C. Pan, S. Tanaka, F. Wu, Y. Zhao, J. S. Speck, S. Nakamura, S. P. DenBaars, and D. Feezell, *Appl. Phys. Express* **5**, 62103 (2012).
- 16 J. E. Northrup, *Appl. Phys. Lett.* **95**, 10 (2009).



## Background

---

III-nitrides are known as the third generation semiconductor materials with a great prospect as a result of their unique properties, such as wide direct bandgap and excellent stability under extreme environmental conditions. However, due to a number of fundamental problems mentioned in the 1<sup>st</sup> Chapter, it is difficult to achieve high efficiency InGaN based emitters in the longer wavelength such as green and yellow spectral region. GaN grown along semi-polar and non-polar orientations has emerged as a promising way to overcome the green/yellow gap issue. This chapter will introduce the advantages, current development, epitaxial techniques and defect reduction in III-nitrides grown along semi-polar and non-polar orientations

### 2.1 Introduction of III-nitrides

#### 2.1.1 Crystal structure

III nitride materials have three different types of crystal structures: Wurtzite ( $\alpha$ -phase), zinc-blende ( $\beta$ -phase), and rocksalt structures.<sup>1</sup> III-nitrides with a rocksalt structure could only appear due to a phase transition from the wurtzite structure under an extremely high pressure (>37 GPa), but it is unstable under ambient pressure.<sup>2</sup> Most of the III-nitrides achieved in practice exhibit a wurtzite structure or a zinc-blende structure. Figure 2.1 (a) and (b) illustrate the atomic arrangements of III-nitrides with a wurtzite structure and a zinc-blende structure, respectively. In both structures, each Ga (In, Al) atom is surrounded by four N atoms, while each N atom is also surrounded by four Ga (In, Al) atoms. This configuration forms a tetrahedrally coordinated structure. The difference between a wurtzite structure and a zinc-blende structure is due to their layer stacking sequence. Along the  $c$ -direction which is vertical to the hexagonal basal plane, a wurtzite structure shows a stacking sequence of AaBbAaBbAaBb..., where the capital and lowercase letters represent the group III element (i.e., Ga (In, Al) atom) and the group V element (i.e., N atom), respectively, and the letters A and B indicate different atomic positions. On the other hand, the stacking order in a zinc-

blende structure is  $AaBbCcAaBbCc\dots$ , where the third layer is located at a different position labeled as position C, as illustrated in Figure 2.1c. In a wurtzite structure, the distance between two nearest Ga atoms (or N atoms) along the  $c$ -direction is defined as the lattice constant  $c$ , while the distance between two nearest Ga atoms (N atoms) within the hexagonal basal plane is defined as the lattice constant  $a$ . In a zinc-blende structure, the lattice constant  $a$  in a cubic unit cell is defined using the distance between two nearest Ga atoms (N atoms) along the  $[001]$  direction. The  $[001]$  direction has an inclination angle of around  $55^\circ$  to the hexagonal basal plane.

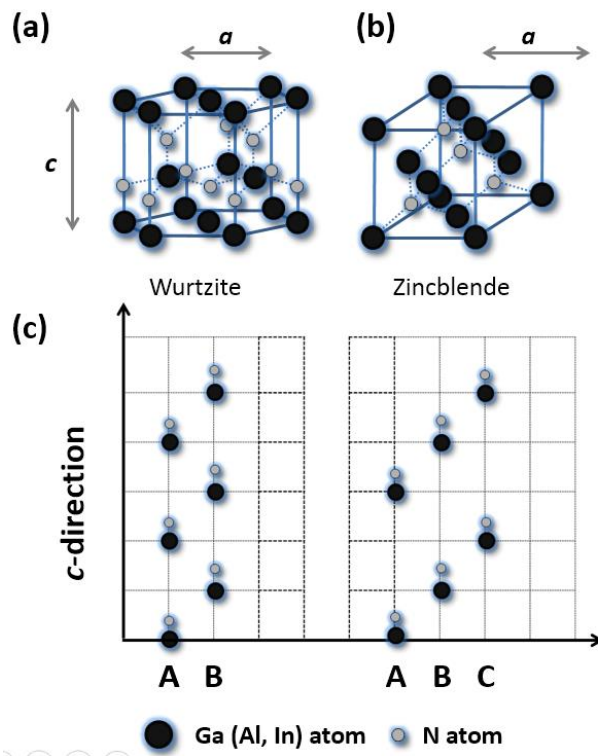


Figure 2.1: III-nitrides of a wurtzite structure (a) and a zinc-blende structure (b) with their corresponding stacking sequences illustrated in (c).

Table 2.1 summarizes the lattice constants of III-nitrides with a wurtzite structure or a zinc-blende structure at room temperature. It has been reported that a phase transition in GaN films from a wurtzite structure to a zinc-blende structure could be observed by means of a radio-frequency planar magnetron sputtering growth technique when decreasing the pressure of the used nitrogen gas from 30 to 10 mTorr.<sup>3</sup> Compared with the zinc-blende structure, the wurtzite structure is more thermodynamically stable,<sup>4</sup> demonstrating a great advantage in

practical applications. As a result, the study is focused on III-nitrides with a wurtzite structure in this thesis.

Table 2.1: Lattice parameters of III-nitride materials at room temperature.<sup>5-7</sup>

		GaN	InN	AlN
Wurtzite	$a(\text{Å})$	3.1893	3.5380	3.1130
	$c(\text{Å})$	5.1851	5.7020	4.9816
	$c/a$	1.6258	1.6116	1.6003
Zincblende	$a(\text{Å})$	4.52	4.98	4.38

### 2.1.2 Spontaneous and piezoelectric polarization

In an ideal wurtzite structure, the ratio of the lattice constants  $c$  to  $a$  is  $c/a = \sqrt{8/3} = 1.633$ . However, the ratio values of III-nitride materials are all smaller than the standard value, which makes the centres of Ga (In, Al) atoms (negative charge) and N atoms (positive charge) locate in different positions in a unit cell. This lack of the inversion symmetry in wurtzite III-nitrides leads to the presence of spontaneous polarization  $\mathbf{P}_s$ , along the  $-c$  direction. The spontaneous polarizations are  $-0.029$ ,  $-0.032$  and  $-0.081$  C/m<sup>2</sup> for unstrained GaN, InN and AlN, respectively.<sup>8</sup> A negative sign indicates the direction of spontaneous polarization field is from Ga-face to N-face, opposite to the (0001) direction. Among III-nitrides, AlN exhibits the largest spontaneous polarization as a result of the smallest ratio of lattice parameters.

In addition to the spontaneous polarization, there also exists a strain-induced polarization field, which can be described by piezoelectric polarization  $\mathbf{P}_p$ . Piezoelectric polarization could be observed in InGaN (AlGaIn) layer grown on GaN substrate as a result of their lattice mismatch. For an InGaIn/GaN heterostructure, the direction of piezoelectric polarization is opposite to the direction of spontaneous polarization, as an InGaIn layer suffers from a compressive strain on a GaN surface. For an AlGaIn/GaN heterostructure, the AlGaIn layer experiences a tensile strain, making the piezoelectric polarization and spontaneous polarization along the same direction. The total polarization  $\mathbf{P}$  in III-nitride materials includes spontaneous polarization and piezoelectric polarization, described below.

$$\mathbf{P} = \mathbf{P}_s + \mathbf{P}_p \quad (2.1)$$

Piezoelectric polarization  $\mathbf{P}_p$  is related to the piezoelectric coefficient  $e$  of materials and the strain tensor  $\varepsilon$ ,  $\mathbf{P}_p = e_{ij}\varepsilon_{mn}$  ( $ij, mn = xx, yy, zz, yz, zx, xy$ ).<sup>9</sup> For a (0001)-orientated III-nitrides, the strain-induced piezoelectric field can be described by Equation 2.2

$$\mathbf{P}_p = e_{zz}\varepsilon_{zz} + e_{zx}(\varepsilon_{xx} + \varepsilon_{yy}) \quad (2.2)$$

where the relationship between a strain tensor and lattice mismatch follows the equations  $\varepsilon_{xx} = \varepsilon_{yy} = \frac{a-a_0}{a_0}$  and  $\varepsilon_{zz} = \frac{c-c_0}{c_0}$ . For an alloy grown on an unstrained GaN layer along the  $c$ -direction, it can be assumed that there is a symmetric biaxial stress in the growth plane<sup>10</sup> In that case, a relationship between the strain tensors parallel and perpendicular to the growth direction can be obtained:  $\varepsilon_{zz} = -2\frac{C_{13}}{C_{33}}\varepsilon_{xx}$ , where  $C_{13}$  and  $C_{33}$  are components of an elastic tensor. Then, Equation 2.2 can be simplified into:

$$\mathbf{P}_p = 2\left(e_{zx} - \frac{C_{13}}{C_{33}}e_{zz}\right)\frac{a-a_0}{a_0} \quad (2.3)$$

Fixed sheet charges can be generated in a (0001)-orientated GaN-based heterostructure as a result of the polarization discontinuity, which can affect the optical performance of heterostructure devices, such as InGaN/GaN based LEDs.

### 2.1.3 Band Structure

#### Direct bandgap

For a single crystal, the energy difference between the minima of a conduction band and the maxima of a valence band is defined as a bandgap, which determines the electrical conductivity of the crystal. Based on a bandgap, materials can be divided into three categories: an insulator with a large bandgap (there is no a specific value) such as SiO<sub>2</sub>; a conductor with a small or zero bandgap such as a metal. Between them is a semiconductor.

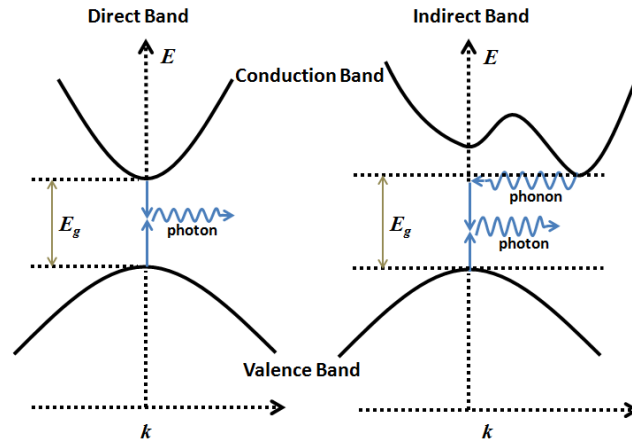


Figure 2.2: Radiative recombination processes in a semiconductor with a direct band (left) and an indirect band (right). The carrier recombination process for a semiconductor with an indirect band structure involves an additional phonon, leading to much slower recombination process than that for a semiconductor with a direct band structure.

According to the band structure of semiconductors, semiconductors can be divided into two types, one with a direct bandgap such as III-nitride materials, and the other one with an indirect bandgap such as silicon (Si) and germanium (Ge). In a direct bandgap semiconductor, the maxima of its valence band and the minima of its conduction band exhibit a same momentum, while for an indirect bandgap semiconductor, their momenta are different. For an indirect bandgap semiconductor, an electron-hole recombination process from the conduction band to the valence band involves an additional phonon in order to meet the momentum conservation, while it does not for a direct bandgap material, as shown in Figure 2.2. The involved phonon finally converts into heat. Since the recombination process for an indirect bandgap semiconductor requires an extra process as a result of involving the phonon, it would take a long time to finish the recombination process, leading to much less efficiency in comparison with an direct bandgap semiconductor. Therefore, a direct bandgap semiconductor is generally used for fabrication of LEDs or laser diodes.

### Wide and tunable bandgap

When a photon is generated through a radiative recombination process, the transitional energy is inversely proportional to the wavelength  $\lambda$  of the emitted photon:

$$\lambda = \frac{hc}{E} \quad (2.4)$$

where  $h$  is the Planck constant and  $c$  is the speed of light in vacuum. The group of III-nitride materials all exhibit a direct bandgap structure with a band gap ranging from 6.0 eV (206 nm) to 0.7 eV (1770 nm), the only material system not only covering the whole visible spectrum range (380-700 nm), but also stretching into the deep ultraviolet and the infrared spectra region.

The Ga atoms in a GaN binary alloy could be replaced by In (Al) atoms, and vice versa, forming an InGaN (AlGaN) ternary alloy structure. This replacement changes the average lattice constants of the ternary alloy, leading the bandgap of InGaN (AlGaN) structure to be different from the binary alloy. For a (0001)-orientated III-nitrides with a ternary alloy structure, the bandgap of such a ternary alloy could be estimated from an empirical equation:

$$E_g(A_xB_{1-x}N) = E_g(A)x + E_g(B)(1 - x) - bx(1 - x) \quad (2.5)$$

where A and B denote different binary alloys of GaN, InN, and AlN;  $x$  is the alloy composition; and  $b$  is a bowing parameter which is positive for III-nitride materials. Although the lattice parameters of ternary alloy is linear to the alloy composition, the band structure exhibits a nonlinear dependence to the strain. Thus, the bowing parameter  $b$  is introduced to quantify this nonlinearity.<sup>135</sup>

## 2.2 Prospects of semi-polar and non-polar III-nitrides

### 2.2.1 Semi-polar and non-polar orientations

As mentioned in section 2.1.2, sheet charges can be formed in a GaN-based heterostructure due to the discontinuities in spontaneous polarization and strain-induced piezoelectric polarization. These internal electric fields formed as a result of both polarizations will lead to the quantum confined Stark effect (QCSE) in InGaN-based LEDs and consequently deteriorates the device performance.<sup>11</sup> A number of ideas have been proposed to resolve this issue. When a large external bias is applied across an InGaN/GaN quantum well, the internal electric fields can be compensated, depending on the direction of the external bias.<sup>12</sup> A heavy Si doping in GaN barrier has been used, which leads to a clear reduction in the QCSE due to the screening effect.<sup>13,14</sup> It can also reduce the QCSE if the strain across an InGaN quantum well region can be relaxed. There are a number of examples which have been used for the growth of InGaN/GaN based visible LEDs, such as increasing  $n$ -GaN thickness,<sup>15</sup> inserting an

extra InGaN layer after an InGaN/GaN quantum well region but before an AlGaIn electron blocking layer,<sup>16</sup> using a *p*-InGaN layer instead of a *p*-GaN layer,<sup>17</sup> and polarization doping around the active region.<sup>18</sup> However, these approaches cannot fundamentally resolve the polarization induced QCSE. For example, heavy doping will affect the material quality seriously and introduce more nonradiative recombination centres; strain relaxation will lead to the generation of defects such as dislocations as non-radiative recombination centres.

To circumvent the polarization issues in a GaN-based hetero-structure, one of the most promising approaches is to grow a GaN crystal along a semi-polar or a non-polar orientation. For the GaN grown along a non-polar orientation, there will be no polarization, while for the GaN grown along a semi-polar orientation the polarizations are significantly reduced. Figure 2.3 illustrates a number of typical crystallographic planes in wurtzite GaN. Non-polar planes, such as *a*-plane {11-20} and *m*-plane {1-100}, are perpendicular to the basal *c*-plane (0001), while semi-polar planes are inclined to the *c*-plane as shown in Figure 2.3b. For example, semi-polar {11-22} plane exhibits an inclination angle of 58.4° to the *c*-plane, and {10-11} plane shows an angle of 62.0°.

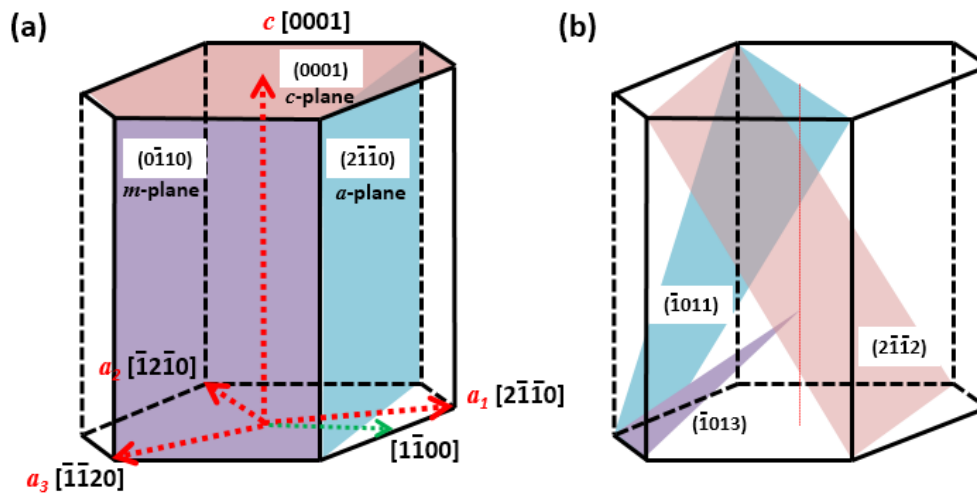


Figure 2.3: Schematic of the crystallographic planes in wurtzite GaN including (a) polar, non-polar and (b) semi-polar planes.

### 2.2.2 Reduced or eliminated piezoelectric field

Theoretical work has been carried out to study piezoelectric polarizations in a strained III-nitride layer grown along a semi-polar or a non-polar orientation.<sup>19,20</sup> This is particularly important for InGaN/GaN quantum well structures. Their calculation work adopted the relationship between piezoelectric fields and piezoelectric coefficients ( $\mathbf{P}_p = e_{ij}\epsilon_{mn}$  ( $ij, mn = xx, yy, zz, yz, zx, xy$ ) as mentioned in section 2.1.2) Using a rotation matrix, piezoelectric coefficients and elastic tensors can be converted from a conventional coordinate system (z-axis parallel to the (0001) direction) into a new coordinate system (z-axis parallel the growth direction). With the new piezoelectric coefficients and elastic tensors of III-nitrides, Northrup has calculated the polarization in an  $\text{In}_x\text{Ga}_{1-x}\text{N}/\text{GaN}$  heterostructure as a function of the angle between the growth direction and the  $c$ -direction, which is shown in Figure 2.4.<sup>21</sup>

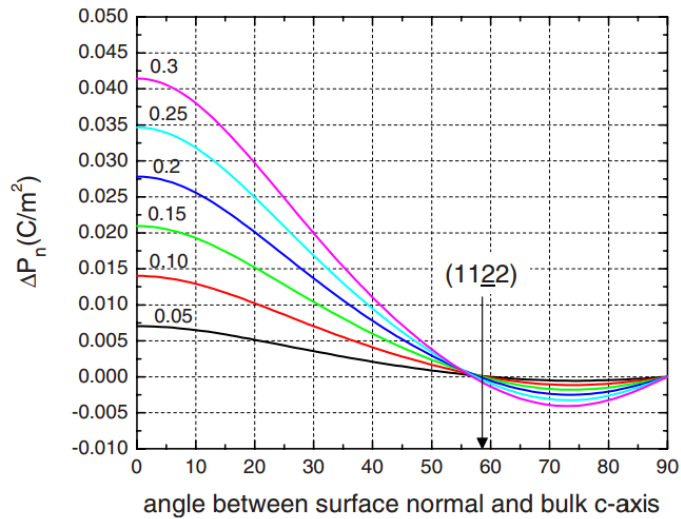


Figure 2.4: Polarization in  $\text{In}_x\text{Ga}_{1-x}\text{N}/\text{GaN}$  heterostructure as a function of the angle between the surface normal and bulk  $c$ -axis. Indium compositions  $x=0.05, 0.1, 0.15, 0.2, 0.25$  and  $0.3$  are denoted at each curve.<sup>21</sup>

When increasing inclination angle from  $0^\circ$ , the polarization starts to decrease and then reaches a zero value at around  $55^\circ$ , followed by moving towards a negative value before going back to zero at  $90^\circ$ . The negative value means that the piezoelectric field has an opposite direction. The zero-polarization points from these curves correspond to two non-polar planes. Semi-polar planes each with a large inclination angle, such as (11-22), (10-11) and (20-21),

show a significant reduction in piezoelectric polarization. The polarization in semi-polar (11-22) plane is almost 10% of that in conventional *c*-plane.

### 2.2.3 Indium incorporation

Due to a large difference in lattice parameter, the solubility of In in GaN is found to be very low at a typical growth temperature (e.g. 800 °C).<sup>136</sup> This difficulty in indium incorporation has become a critical barrier to overcoming the “green/yellow” gap. Atomic arrangements are different between the *c*-plane, semi-polar plane and non-polar plane GaN, leading to the difference in the rate of indium incorporation into the GaN grown along different orientations. First-principles calculations show that indium can be more easily incorporated into semi-polar (11-22) GaN than those on its *c*-plane or non-polar counterparts.<sup>21-23</sup>

Apart from the theoretical calculation, experimental investigation has also been carried out by Wernicke to evaluate the indium incorporation in various orientations, such as (0001), (10-12), (11-22), (10-11), (20-21) and (10-10) orientations.<sup>24</sup> In a large range of growth temperature, it has been found that semi-polar (11-22) and (10-11) orientations exhibit a notably higher indium mole fraction than both the polar and non-polar orientations, while semi-polar (20-21) show a similar indium content to the polar and non-polar orientations. The indium composition in his investigation has been estimated from XRD measurements. Zhao, et al. have reported a systematic study of the emission properties of (11-22), (20-21), (30-31) and (10-10) plane InGaN quantum well.<sup>25</sup> All the samples are grown under the same growth condition. It has been found that (11-22)-orientated InGaN quantum well exhibits a longer emission wavelength than other samples, indicating higher indium composition. Overall, among all the semi-polar and non-polar orientations, (11-22) orientation shows a great potential in obtaining InGaN quantum well with longer wavelength.

### 2.2.4 Doping

Nominally undoped III-nitride materials exhibit n-type as a result of nitrogen vacancies which induce extra electrons. For GaN MOCVD growth, silane (SiH<sub>4</sub>) is widely used as the source of silicon to obtain n-type GaN layer, while cyclopentadienyl magnesium [(Cp)<sub>2</sub>Mg] is chosen as the source of magnesium for p-type GaN. According to the relative density of Ga and N atoms, GaN facets with different orientations are classified as Ga-polar and N-polar GaN.<sup>26</sup> For example, (000-1), (10-11) and (11-22) plane GaN are N-polar GaN with N atoms

being the major atoms on surface. On the other hand, (0001), (20-2-1) and (30-3-1) plane GaN are Ga-polar GaN.<sup>25</sup> It has been reported that there is few difference in the Si incorporation between Ga-polar and N-polar GaN layers under a range of growth conditions.<sup>27</sup> A similar result was also reported for the Mg incorporation in Ga-polar and N-polar layers.<sup>28</sup> Furthermore, N-polar GaN exhibits an abrupt doping profile in a 150 nm p-GaN/150 nm n-GaN multilayer stack, which is attributed to the suppression of Mg memory effect in N-polar GaN.<sup>27,29</sup>

Despite the conclusion of these reports, a number of studies have demonstrated the advantages of p-type doping in GaN along a semi-polar or a non-polar orientations.<sup>30-33</sup> A high hole concentration of up to  $7 \times 10^{18} \text{ cm}^{-3}$  has been obtained in (1-100) GaN film, demonstrating a significant improvement in p-type doping compared with its *c*-plane counterpart.<sup>30</sup> Similar results were also reported for the p-type doping in semi-polar (10-1-1) and non-polar (11-20) GaN.<sup>31,32</sup> Theoretical study shows that subband energy spacing in InGaN/GaN QW structure decreases with increasing the angle between surface normal and bulk *c*-axis, leading to an increase in carrier population in the higher subbands. As a result, the hole effective mass of the higher subbands decreases monotonically with increasing the crystal angle.<sup>33</sup> This means that semi-polar GaN is expected to have a higher hole mobility than its *c*-plane counterpart, resulting in an improvement in the conductivity of a p-type layer along a semi-polar orientation.

### 2.2.5 Development of semi-polar and non-polar III-nitrides

Before 2000 there were only a very limited number of reports on the growth of non-polar and semi-polar GaN, as the major efforts were devoted to the *c*-plane GaN. In the early period, GaN with (11-20) facet grown on (10-12) sapphire substrates was unintentionally observed as a result of attempting to look for a sapphire substrate with a suitable orientation for *c*-plane GaN growth.<sup>34-37</sup> Soon after that, non-polar and semi-polar GaN were also reported on sapphire and silicon substrates.<sup>38-40</sup> At the beginning of 2000, Takeuchi carried out a theoretical study on the orientation dependence of the internal electrical field in wurtzite III-nitrides, revealing the advantage of reduced or eliminated internal electrical fields in InGaN/GaN heterostructure grown along different semi-polar or non-polar orientations.<sup>19</sup> At the same time, Waltereit reported the first non-polar *m*-plane GaN grown on  $\gamma$ -LiAlO<sub>2</sub> substrates by molecular beam epitaxy (MBE). No piezoelectric field has been found in the GaN/AlGaIn quantum wells grown on the *m*-plane GaN.<sup>41</sup> Since then, non-polar and semi-polar orientations started to receive

more and more attention and the study has experienced a rapid development in the past years. Table 2.2 lists a number of reports on the study of non-polar and semi-polar III-nitrides regarding substrate choice, growth method, and demonstration of related devices. During the development of semi-polar and non-polar III-nitrides, major efforts are devoted to improving the material quality, which are essential for the achievement of high-performance devices. Furthermore, a great challenge in non-polar orientation is due to the low indium incorporation efficiency, making it difficult in growth longer wavelength such as green/yellow LEDs, where high indium content is required. Therefore, it is clear that semi-polar orientation such as (11-22) has emerged to be a promising candidate for the fabrication of longer wavelength emitters.

Table 2.2: A summary of reports on the growth of semi-/non- polar GaN in terms of substrate choices, growth methods and devices.

Year	Events	Indicative results	Growth methods	Authors
2000	<i>m</i> -plane GaN/AlGaIn MQW on $\gamma$ -LiAlO <sub>2</sub> substrate	N/A	MBE <sup>a</sup>	Waltreite et al <sup>41</sup>
2002	<i>a</i> -plane GaN/AlGaIn MQW on (10-12) <i>r</i> -plane sapphire	QW emission peak at 352 nm at RT	MBE	Ng <sup>42</sup>
	<i>a</i> -plane GaN on <i>r</i> -plane sapphire	Dislocation density: $2.6 \times 10^{10} \text{ cm}^{-2}$ BSF density: $3.8 \times 10^5 \text{ cm}^{-1}$	MOCVD <sup>b</sup>	Craven et al <sup>43</sup>
	<i>m</i> -plane GaN on bulk GaN	Stimulated emission observed at RT	MOCVD	Chen et al <sup>44</sup>
2003	<i>a</i> -plane GaN on <i>a</i> -plane SiC with HT AlN buffer layer	Dislocation density: $\sim 3 \times 10^{10} \text{ cm}^{-2}$ QW emission peak at 360 nm at RT	MOCVD	Craven et al <sup>45</sup>
	<i>a</i> -plane GaN on <i>r</i> -plane sapphire with ELOG <sup>c</sup>	Wing region: Dislocation density: $\sim 5 \times 10^6 \text{ cm}^{-2}$ BSF density: $3 \times 10^3 \text{ cm}^{-1}$	HVPE <sup>d</sup>	Haskell et al <sup>46</sup>
2004	Micro-facet of (11-22) InGaIn MQW	QW emission peak at 404 nm at RT	MOCVD	Nishizuka et al <sup>47</sup>
	(10-12) GaN on (001) Si with 2 °6 ° miscut angle	N/A	MOCVD	Schulze et al <sup>48</sup>
	<i>a</i> -plane InGaIn/GaN LED on bulk GaN	QW emission peak at 413.5 nm at RT	MOCVD	Chakraborty et al <sup>49</sup>
2005	<i>m</i> -plane InGaIn/GaN LED on bulk GaN	QW emission peak at 450 nm with high injection current at RT	MOCVD	Chakraborty et al <sup>50</sup>
	<i>a</i> -plane GaN on (11-20) 4H-SiC	Dislocation density: $4.4 \times 10^{10} \text{ cm}^{-2}$ BSF density: $1.6 \times 10^6 \text{ cm}^{-1}$	MOCVD	Dmitri et al <sup>51</sup>
	(10-1-1) GaN on (100) MgAl <sub>2</sub> O <sub>4</sub> and (10-1-3) GaN on (110) MgAl <sub>2</sub> O <sub>4</sub>	N/A	HVPE	Baker et al <sup>52</sup>

	(10-1-1) and (10-1-3) InGaN LED on MgAl <sub>2</sub> O <sub>4</sub>	QW emission peak at ~439 nm for both LEDs at RT	MOCVD	Chakraborty et al <sup>53</sup>
2006	(10-1-3) and (11-22) GaN on <i>m</i> -plane sapphire	(10-1-3) GaN film: Dislocation density: $9 \times 10^8 \text{ cm}^{-2}$ BSF density: $2 \times 10^5 \text{ cm}^{-1}$ (11-22) GaN film: Dislocation density: $2 \times 10^{10} \text{ cm}^{-2}$ BSF density: $2 \times 10^5 \text{ cm}^{-1}$	HVPE	Baker et al <sup>54</sup>
	(11-22) InGaN/GaN LED on bulk GaN	QW emission peak at ~580 nm at RT	MOCVD	Funato et al <sup>55</sup>
	Micro-facet of (10-11) InGaN/GaN LED	QW emission peak at 425 nm at RT	MOCVD	Wunderer et al <sup>56</sup>
2007	<i>m</i> -plane GaN on ZnO substrate	N/A	PLD <sup>e</sup>	Kobayashi et al <sup>57</sup>
	(10-1-1) GaN/InGaN LED on bulk GaN	QW emission peak at 411 nm at RT	MOCVD	Tyagi et al <sup>58</sup>
	<i>m</i> -plane InGaN/GaN LD on bulk GaN	Stimulated emission peak at 405.5 nm at RT	MOCVD	Schmidt et al <sup>59</sup>
	(11-22) GaN and AlN on <i>m</i> -plane sapphire	N/A	MBE	Lahourcade et al <sup>60</sup>
	<i>m</i> -plane InGaN/GaN LED on $\gamma$ -LiAlO <sub>2</sub> substrate	QW emission peak at ~515 nm at RT	MOCVD	Liu et al <sup>61</sup>
2008	<i>m</i> - plane GaN on <i>m</i> - plane sapphire	N/A	MOCVD	Armitage et al <sup>62</sup>
	<i>a</i> - plane GaN and (11-26) GaN on <i>r</i> - plane sapphire	<i>a</i> -plane GaN film: Dislocation density: $5 \times 10^{10} \text{ cm}^{-2}$ BSF density: $7 \times 10^5 \text{ cm}^{-1}$ (11-26) GaN film: Dislocation density: $8 \times 10^9 \text{ cm}^{-2}$	MBE	Zhou et al <sup>63</sup>
	(11-22) InGaN/GaN LD on bulk GaN	Stimulated emission peak at 426.9 nm at RT	MOCVD	Asamizu et al <sup>64</sup>
	<i>a</i> -plane GaN on patterned (110) Si	Window region: Dislocation density: $3 \times 10^7 \text{ cm}^{-2}$	MOCVD	Tanikawa et al <sup>65</sup>
2009	(10-12) AlN on (1-102) ZnO substrate	N/A	PLD	Ueno et al <sup>66</sup>
	<i>m</i> -plane GaN on <i>m</i> -plane sapphire	FWHMs of XRC along <i>c</i> -direction and <i>m</i> -direction are 0.87 ° and 0.25 °, respectively.	HVPE	Zhu et al <sup>67</sup>
	(10-11) GaN on patterned (001) Si and (11-22) GaN on patterned (113) Si	N/A	MOCVD	Sawaki et al <sup>68</sup>
	(11-22) GaN on GaN on patterned (113) Si	N/A	HVPE	Suzuki et al <sup>69</sup>
	(20-21) InGaN/GaN LD on bulk GaN	Lasing wavelength of 520 nm at RT	MOCVD	Enya et al <sup>70</sup>
	<i>m</i> -plane GaN on patterned (112) Si	N/A	MOCVD	Ni et al <sup>71</sup>
2010	(30-31) InGaN/GaN LD on bulk GaN	Lasing peak at 444.7 nm at RT	MOCVD	Hsu et al <sup>72</sup>

	(10-11) GaN on (11-23) patterned sapphire substrate	FWHM of XRC ~400 arcsec	MOCVD	Schwaiger et al <sup>73</sup>
	(30-3-1) InGaN/GaN LED on bulk GaN	Emission peak wavelength at 452 nm	MOCVD	Koslow et al <sup>74</sup>
	(11-2 <i>l</i> ) InN on yttria stabilized zirconia (YSZ) substrate	N/A	PLD	Fujii et al <sup>75</sup>
	(10-13) InN on (110) GaAs	N/A	MOCVD	Murakami et al <sup>76</sup>
2011	(20-2-1) InGaN/GaN LED on bulk GaN	Emission peak wavelength at ~423 nm	MOCVD	Zhao et al <sup>77</sup>
	(20-2-1) LD on bulk GaN	Lasing peak wavelength at 505 nm.	MOCVD	Huang et al <sup>78</sup>
2012	(10-14) GaN on <i>a</i> -plane patterned sapphire substrate	FWHM values of (0002) and (01-14) XRCs are 910 and 868 arcsec, respectively,	MOCVD	Hsieh et al <sup>79</sup>
2013	(10-11) GaN on graphene	N/A	MOCVD	Gupta et al <sup>80</sup>
	Micro-facet of (10-15) AlN on (111) Si	Emission peaks from 380 to 550 nm	MBE	Yang et al <sup>81</sup>
2015	(20-21) GaN on patterned (114) Si with 1 ° miscut angle	FWHM values of scanning parallel and perpendicular to the <i>c</i> -direction are 610 and 1490 arcsec, respectively,	MOCVD	Khoury et al <sup>82</sup>
	(20-23) GaN on 3C-SiC/(001)Si	LED emission peak wavelength at ~493 nm at RT.	MOCVD	Dinh et al <sup>83</sup>
	Green to amber (11-22) LEDs on <i>m</i> -plane sapphire	Emission peak wavelength at ~492 nm at RT	MOCVD	Bai et al <sup>84</sup>

- a) MBE: Molecular beam epitaxy  
b) MOCVD: Metalorganic chemical vapour deposition  
c) ELOG: Epitaxial lateral overgrowth  
d) HVPE: Hydride vapour phase epitaxy  
e) PLD: Pulsed laser deposition

## 2.3 Heteroepitaxy of semi-polar and non-polar III-nitrides

### 2.3.1 Substrates for heteroepitaxy

III-nitride materials are typically grown using heteroepitaxy techniques as a result of the lack of affordable substrates. As mentioned in Table 2.2, a wide range of substrates, such as  $\gamma$ -LiAlO<sub>2</sub>, MgAl<sub>2</sub>O<sub>4</sub>, (1-102) ZnO, yttria stabilized zirconia (YSZ), silicon carbide (SiC), sapphire and silicon have been applied for the hetero-epitaxial growth of non-polar and semi-polar III-nitrides. The oxide substrates have small mismatches in both lattice parameters and thermal expansion coefficients with GaN. However, there exists a serious issue, namely, the diffusion of the metallic atoms from the substrate to the overlying GaN under a temperature

required by the growth of GaN using MOCVD.<sup>85,86</sup> SiC substrates also exhibit less lattice mismatch compared with other substrates such as sapphire or silicon, but the cost is very high.<sup>87</sup> Among these foreign substrates, sapphire and silicon have been widely used as substrates for the growth of GaN.

## Sapphire

Sapphire has a wurtzite structure with lattice parameters of  $a=4.758 \text{ \AA}$  and  $c=12.991 \text{ \AA}$ .<sup>88</sup> (0001)  $c$ -plane sapphire is typically used as a substrate for conventional  $c$ -plane GaN growth. Besides the  $c$ -plane GaN, GaN layers with other orientations could also be achieved by using sapphire substrate. For example, non-polar (11-20)  $a$ -plane GaN could be obtained on (10-12)  $r$ -plane sapphire with lattice mismatches of 16.1% and 1.1% for  $[1-100]_{\text{GaN}} \parallel [11-20]_{\text{sapphire}}$  and  $[0001]_{\text{GaN}} \parallel [-1101]_{\text{sapphire}}$  directions, respectively. Semi-polar (11-22) GaN could be grown on (1-100)  $m$ -plane sapphire, where the lattice mismatches are 16.1% and 6.3% for  $[1-100]_{\text{GaN}} \parallel [11-20]_{\text{sapphire}}$  and  $[-1-123]_{\text{GaN}} \parallel [0001]_{\text{sapphire}}$  directions, respectively. Sapphire has a high melting point of around 2050 °C, demonstrating an excellent stability during GaN growth temperature at a high temperature in MOCVD. Furthermore, sapphire is transparent for visible light, and there is no absorption issue if the visible LEDs are grown on it.

Due to the mismatch in both lattice parameters and thermal expansion coefficients between GaN and sapphire, GaN epitaxial film on sapphire usually contains a lot of dislocations. In order to address this issue, a number of growth techniques have been developed to improve the crystal quality of GaN, which will be introduced in next section (section 2.3.2). Furthermore, as sapphire is an insulator, the fabrication of LEDs grown on sapphire have to use a lateral contact configuration.

## Silicon

Silicon is a cubic structure material with a lattice parameter of  $a=5.431 \text{ \AA}$ . (0001)  $c$ -plane GaN can be grown on (111) plane Si with a lattice mismatch of 16.9%. Semi-polar (10-13) and (11-22) plane GaN can be obtained on patterned Si substrates using a selective area growth (SAG) technique.<sup>68</sup> In the past decades, Si has experienced a rapid development due to its excellent physical property and wide availability. The mature fabrication processes for Si have been developed in the semiconductor industry. Compared with other substrates, high quality Si substrate are available in a large size of up to 450 mm diameter, which allows for volume

production at a low cost.<sup>89</sup> As a result, Si has emerged as an attractive alternative for the GaN heteroepitaxial growth.

However, there are several problems for the GaN grown on Si substrate. Firstly, Ga atoms can react with the Si substrate during the growth, forming the so-called Ga melt-back issue which leads to severe etching.<sup>90</sup> This melt-back etching issue will eventually stop the growth of GaN, and thus must be avoided. Secondly, there is a large mismatch in thermal expansion coefficient between GaN and Si. During the cooling process, tensile stress will be introduced in the GaN film grown on Si substrates, leading to severe cracking. Thirdly, Si substrate can absorb visible light due to its small bandgap of 1.12 eV, lowering the EQE of LEDs on it. Finally, being similar to sapphire, Si also has a large lattice mismatch with GaN, which will lead to a high-density of dislocations in GaN.

### **2.3.2 Growth techniques for improving crystal quality**

Due to the large mismatches in lattice parameters and thermal expansion coefficients between GaN and sapphire (or silicon), semi-polar and non-polar GaN directly grown on planar sapphire (or silicon) substrate will contain a large amount of defects. Furthermore, the growth technique of semipolar GaN is far from satisfactory compared with its *c*-plane counterpart. Therefore, so far the crystal quality of semipolar GaN is far from the requirement for growing high-efficiency devices. To address this problem, a number of growth techniques have been proposed.

#### **Selective area growth on patterned substrates**

GaN grown on sapphire along the *c*-plane orientation has a systematic and mature growth technology to control the defects in epitaxial films. Compared with the semi-polar and non-polar orientations, GaN growth along the (0001) polar direction usually exhibits a lower defect density. Selective area growth (SAG) on patterned substrates allows the growth to start at certain areas along the *c*-direction, and then coalesce to reach a flat surface. For example, the angle between *r*- and *c*-direction in sapphire crystal is 57.6°, which is very close to the 58.4° angle of (11-22) and *c*-direction in GaN crystal. This enables us to grow (11-22) GaN on the *r*-plane sapphire with a pattern structure, as shown in Figure 2.5.<sup>91</sup> By standard photolithography and dry etching processes, the sapphire with a grooved pattern can be fabricated, where the inclined facet (i.e., the *c*-plane-like sidewall) is close to the *c*-plane and thus GaN can be grown

on this facet. Growth conditions need to be carefully optimized in order to favour the growth on the  $c$ -plane-like sidewall, and simultaneously suppress the growth from  $r$ -plane sapphire and the opposite sidewall.<sup>91</sup> Tendille, et al. reported a similar method for the growth of (11-22) GaN on patterned  $r$ -plane sapphire, but with SiO<sub>2</sub> layer deposited on the top of ridges in order to avoid the growth on  $r$ -plane sapphire.<sup>92</sup> Moreover, it is also found that  $m$ -plane,  $a$ -plane, (11-22) plane and (10-11) plane GaN could be grown on patterned  $a$ -plane,  $m$ -plane (and  $c$ -plane),  $r$ -plane and (11-23)  $n$ -plane sapphire, respectively.<sup>93</sup>

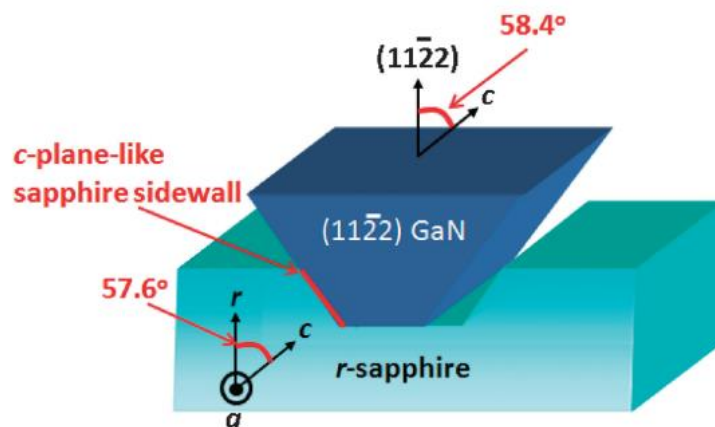


Figure 2.5: Schematic of semi-polar (11-22) GaN on patterned  $r$ -plane sapphire.<sup>91</sup>

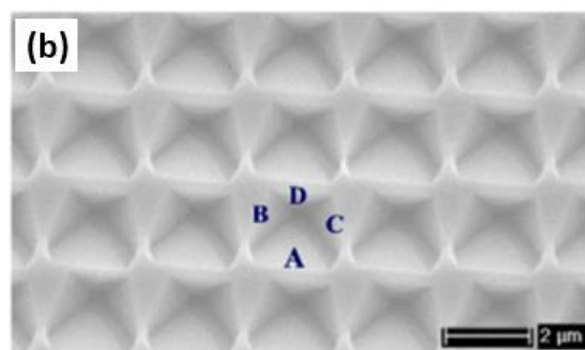
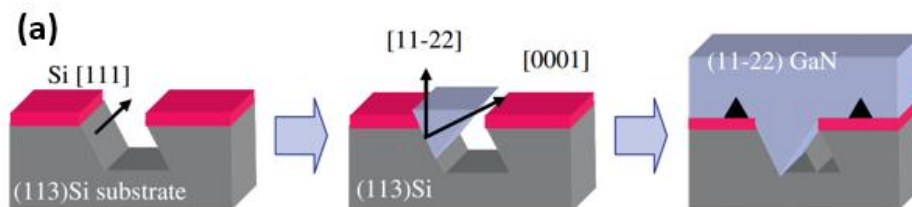


Figure 2.6: (a) Schematic of semi-polar (11-22) GaN on patterned (113) Si substrate. (b) SEM image of (113) Si substrate with another pattern for the growth of semi-polar (11-22) GaN.<sup>68,94</sup>

Si substrate is not suitable for the semi-polar GaN. However, by using a photolithography technique and anisotropic wet-etching processes, patterned (113) Si substrate can be used for the growth of semi-polar (11-22) GaN.<sup>68</sup> As shown in Figure 2.6a, the sidewall with a (111) Si facet can be fabricated using an anisotropic wet-etching process, where facet B, C and D can be deposited with SiO<sub>2</sub> layers and thus leave facet A (i.e., (111) facet) to be exposed for GaN growth.<sup>94</sup> Different wet-etching approaches have been proposed for patterning Si substrates for semipolar GaN growth.<sup>65,69,71</sup>

### Overgrowth on patterned templates

Epitaxial lateral overgrowth (ELOG) technique was firstly employed in the growth of *c*-plane GaN, which demonstrated a significant improvement in the crystal quality of epitaxial films.<sup>95</sup> In 2003, Haskell applied the ELOG technique in the growth of *a*-plane GaN by HVPE, leading to a notable decrease of morphological and structural defects in the overgrown layer.<sup>46</sup> Then, ELOG technique was also used in the growth of *m*-plane and (11-22) plane GaN on sapphire, exhibiting as an effective way to obtain high-quality GaN films.<sup>96-98</sup> All these reports adopted a pattern that typically consists of SiO<sub>2</sub> stripes separated by window regions along the *c*-direction (*c*-projection), with stripes orientated along the *m*-direction. However, due to the anisotropic growth rate within the growth plane, this kind of pattern will lead to a non-uniformity in both surface morphology and crystal quality across the wafer surface.

A nano-rod template fabricated from a self-organized nickel mask approach was established by the Sheffield group for the overgrowth of non-polar and semi-polar GaN on sapphire.<sup>99-101</sup> Figure 2.7 shows the preparation procedure of a nano-rod template. First, a GaN template is directly grown on 2-inch sapphire with a high temperature AlN buffer layer, followed by a deposition of SiO<sub>2</sub> layer on its top. The self-organized nickel islands are fabricated by depositing a thin nickel layer on the SiO<sub>2</sub> layer, followed by a thermal annealing process under a N<sub>2</sub> atmosphere. The sizes and distances of the randomly distributed nickel islands are in the order of hundred nanometers, which could be tuned by the thickness of nickel layer and the annealing process. By a reactive ion etching (RIE) process, the pattern of the self-organized nickel islands is transferred onto the SiO<sub>2</sub> layer. Then the SiO<sub>2</sub> layer is served as a

second mask subsequently for an inductively coupled plasma (ICP) process, which forms GaN nano-rod arrays with SiO<sub>2</sub> on their top. During the overgrowth, GaN layer initiates from the sidewalls and then coalesce to obtain a flat surface. As a result of the small diameters and separations of the nano-rods, a flat surface could be quickly obtained on the nano-rod template with the thickness of the overgrown layer around 4 μm, which is faster than the conventional ELOG technique that cannot reach a good surface until the layer thickness is larger than 10 μm. Furthermore, the random distribution of nano-rods could compensate the anisotropic growth rate within the growth plane, improving the uniformity in crystal quality.<sup>100</sup> Furthermore, a significant improvement has been achieved in both the crystal quality and electrical properties of the semi-polar (11-22) GaN overgrown on the nano-rod template. The experiment indicates that a large diameter will be helpful for further improving the crystal quality.<sup>102</sup> However, due to the limit of the fabrication process, it is difficult to obtain nano-rods with a large diameter (> 1 μm).

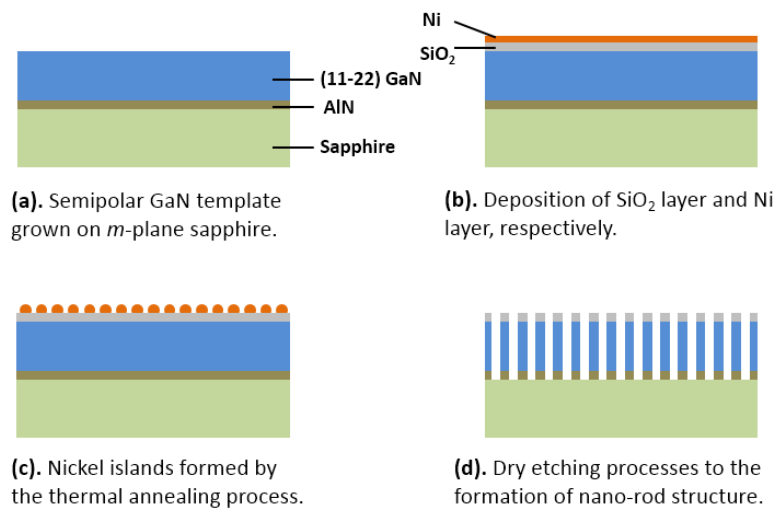


Figure 2.7: A schematic diagram of the fabrication process of nano-rod template.

Instead of using the self-organized nickel islands as the masks, the Sheffield group has developed a regular mask to transfer the designed patterns to the top SiO<sub>2</sub> layer by a standard photolithography process. After following dry etching processes, micro-rods in regular arrays could be obtained. The details of this micro-rod template overgrowth approach will be introduced in section 3.3. The size of the micro-rods and array orientation could be accurately controlled during the fabrication procedure. With this approach, semi-polar (11-22) GaN exhibits a significant improvement in the crystal quality.<sup>103</sup>

## 2.4 Defects in semi-polar and non-polar III-nitrides

Unlike *c*-plane GaN grown on sapphire, where dislocations are the major defects, semi-polar and non-polar GaN on sapphire (or Si) exhibit additional defects. A number of characterization techniques have been employed to study the defects.

### 2.4.1 Defect type

According to dimensionality, defects in a crystal are usually classified as:

(a) Zero dimensional defects: Point defects occur at or around a single atomic site, such as vacancy, interstitial, and substitutional atom.

(b) One dimensional defects: A line of atoms are misaligned in a crystal which is also referred as "line defect", such as perfect and partial dislocations.

(c) Two dimensional defects: A plane of atoms are misaligned such as stacking faults and grain boundaries.

(d) Three dimensional defects: A volume of atoms are absent or appear at some atomic sites such as voids and precipitates.

Among these four types of defects, line and planar defects are the major defects in semi-polar and non-polar III-nitrides with a typical density on the order of  $10^{10}$  cm<sup>-2</sup> for dislocations and  $10^5$  cm<sup>-1</sup> for stacking faults, respectively if they are directly grown on a standard sapphire substrates without involving any extra process. Compared with other types of defects, both dislocations and stacking faults play an important role in determining the optical and electrical properties of semi-polar and non-polar III-nitrides. In this work, it is focused on the dislocation and planar stacking fault.

### Dislocations

To evaluate the lattice distortion caused by the appearance of line defects, a Burgers vector labeled as  $\mathbf{b}$  is used to describe the difference between a distorted lattice and a perfect lattice. A Burgers vector describes the direction and magnitude of the displacement that is required to restore from the distortion. Owing to the principle of minimum energy, dislocations with a Burgers vector which is larger than a unit slip distance ( $|\mathbf{b}| > |\mathbf{a}|$ ) will split into two separate dislocations. As a result, the magnitude of a Burgers vector cannot be larger than the unit slip distance in each orientation. According to the magnitude of a Burger vector, dislocations could be classified as "perfect dislocation" ( $|\mathbf{b}| = |\mathbf{a}|$ ) and "partial dislocation"

( $|\mathbf{b}| < |\mathbf{a}|$ ), respectively.<sup>104</sup> There are three types of perfect dislocations in III-nitrides: edge, screw and mixed dislocations with their Burgers vectors  $\mathbf{b}$  of  $1/3\langle 11-20 \rangle$ ,  $\langle 0001 \rangle$ , and  $1/3\langle 11-23 \rangle$ , respectively. As shown in Figure 2.8, the Burgers vector of an edge dislocation is perpendicular to its dislocation line, while that of a screw dislocation is parallel to its dislocation line. A mixed dislocation is a combination of an edge and a screw dislocation with an inclination angle between the Burgers vector and the dislocation line. In heteroepitaxial GaN films, most of the dislocations exhibit the edge type as a result of small formation energy for the edge dislocation.

Stacking faults are generally associated with partial dislocations in semi-polar and non-polar III-nitrides. Partial dislocations typically with a Burgers vectors  $\mathbf{b}$  of  $1/3\langle 1-100 \rangle$ ,  $1/2\langle 0001 \rangle$  and  $1/6\langle 2-203 \rangle$  are classified as Shockley and Frank partial dislocations, depending on whether the Burgers vectors are parallel or perpendicular to the stacking fault plane. A perfect dislocation could dissociate into two partial dislocations in order to have a lower total energy, such as  $1/3\langle 11-20 \rangle = 1/3\langle 10-10 \rangle + 1/3\langle 01-10 \rangle$ . Consequently, a stacking fault could be formed between the two partial dislocations at the same time.

For III-nitride heterostructures such as an InGaN layer on GaN, misfit dislocations are typically generated at their interface to compensate the misfit between the two layers as a result of the strain induced due to the lattice-mismatch. Misfit dislocations help to release the strain, and are typically generated when the thickness of the strained layer exceeds the so-called critical thickness  $h_c$ , defined below:<sup>105</sup>

$$h_c = \frac{\mathbf{b}}{2\pi f} \frac{(1 - \nu \cos^2 \alpha)}{(1 + \nu) \cos \lambda} \left( \ln \frac{h_c}{\mathbf{b}} + 1 \right) \quad (2.6)$$

where  $\mathbf{b}$ ,  $\nu$  and  $f$  are the Burgers vector of misfit dislocation, Poisson's ratio, and the misfit parameter, respectively. The misfit parameter is determined by the lattice constants of the epitaxial layer and substrate layer ( $f = (a_l - a_{sub})/a_{sub}$ ).  $\alpha$  is the angle between the dislocation line and the burgers vector, and  $\lambda$  is the angle between the slip direction and a line perpendicular to the dislocation line. Misfit dislocations are usually bound by two threading dislocations, forming a half loop. It has been discovered that misfit dislocations in a (11-22) orientated film have a dislocation line along the  $m$ -direction with a burgers vector of  $1/3\langle 11-20 \rangle$ .<sup>106</sup>

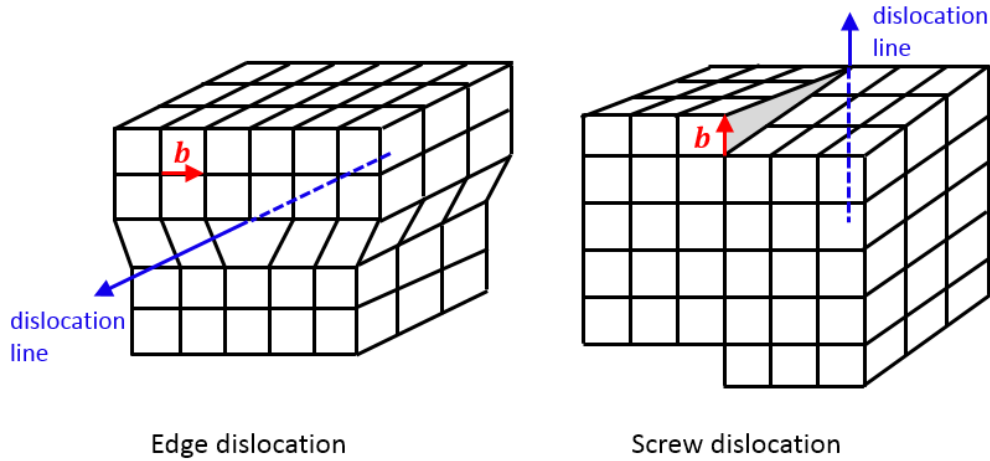


Figure 2.8: Schematic diagrams of edge dislocation and screw dislocation.

### Stacking faults

In a wurtzite structure, the basal planes are stacked in a sequence of ABABAB... In some cases, one layer might be located in a wrong position forming a stacking sequence of ABCBCB... The layer with a position offset is named as "stacking fault". There are two types of stacking faults in an III-nitride wurtzite structure: basal stacking faults (BSF) lying in the (0001) plane and prismatic stacking faults (PSF) lying in either (11-20) plane or (1-100) plane. According to the number of fault layers, BSF could be classified as  $I_1$ -type (ABCBCB),  $I_2$ -type (ABCACA) and  $E$ -type BSFs (ABCABA), as illustrated in Figure 2.9. There are one, two and three cubic bilayers in  $I_1$ -type,  $I_2$ -type and  $E$ -type BSF, respectively. The formation energy of these three types of BSFs has an approximation relationship:  $\gamma_{I1}=1/2 \gamma_{I2}=1/3 \gamma_E$ . with the BSF with  $I_1$ -type having the lowest formation energy. Most of the stacking faults observed in semi-polar and non-polar III-nitrides are  $I_1$ -type. BSFs with  $I_1$ -type can be generated by removing or inserting a bilayer with an offset of  $1/3\langle 1-100 \rangle$ . This means that the  $I_1$ -type BSF cannot be generated during a strain relaxation process, but only during a growth process. On the other hand,  $I_2$ -type BSF can be generated during a strain relaxation process through a basal shear of  $1/3\langle 1-100 \rangle$ .  $E$ -type BSF is produced by the insertion of an extra layer, which can happen during a growth process. The displacement vectors  $\mathbf{R}$  for  $I_1$ -type,  $I_2$ -type and  $E$ -type BSFs are  $1/6\langle 2-203 \rangle$ ,  $1/3\langle 1-100 \rangle$  and  $1/2\langle 0001 \rangle$ , respectively. It has been reported that there is another type of BSF in wurtzite GaN, which is known as  $I_3$ -type BSF.  $I_3$ -type BSF, having a stacking sequence of ABCBAB..., can be formed by replacing a bilayer (A or B) with a wrong bilayer

C. The formation energy of  $I_3$ -type BSF is reported to be slightly larger than that of  $I_1$ -type BSF.<sup>51</sup>

In addition to the BSF in  $c$ -plane, PSF can be observed in the (11-20) or (1-100) plane in III-nitrides with a displacement vector  $\mathbf{R}$  of  $1/2\langle 10-11 \rangle$ . PSF acts as an termination of  $I_1$ -type BSF. Stair-rod dislocations with a Burgers vector of  $\mathbf{b} = 1/6\langle 1-100 \rangle$  are observed at the intersection between BSF and PSF to compensate the difference in displacement vectors. It is calculated that the formation energy of PSF lying in (11-20) plane is  $1153 \text{ erg/cm}^2$  ( $72 \text{ meV/\AA}^2$ ) in GaN,<sup>107</sup> which is significantly larger than the formation energy of BSF ( $40\text{--}4 \text{ erg/cm}^2$ ).<sup>57</sup>

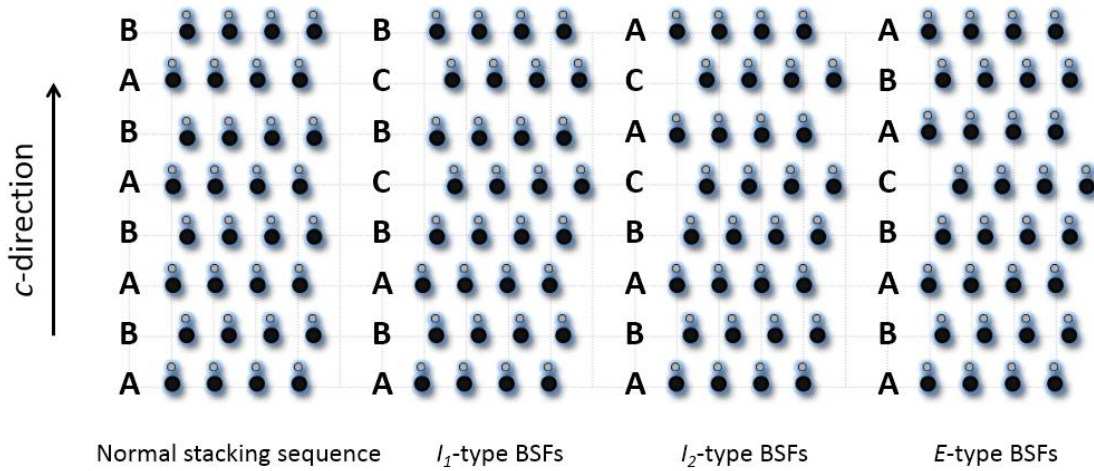


Figure 2.9: Schematic diagrams of a normal stacking sequence of basal plane,  $I_1$ -type,  $I_2$ -type, and E-type BSFs in wurtzite III-nitrides.

#### 2.4.2 Defect observation techniques

A number of techniques have been developed to investigate the defects in III-nitride films. For example, wet-chemical etching is a useful technique to estimate the dislocation density, as the etching process only occurs at dislocation area and produces visible etch pits on the surface.<sup>108</sup> Infrared microscopy could be applied on transparent GaN films to roughly determine the position of defects.<sup>109</sup> Traditionally, X-ray diffraction technique can be employed to evaluate the lattice misorientation that is caused by the defects in a crystal.<sup>110</sup> However, it is difficult to use any of the above-mentioned characterization techniques to quantitatively distinguish the types of defects and determine their accurate locations, as they normally depend on the variation of strain fields around the defect areas. Being different from above techniques, transmission electron microscopy (TEM) technique characterize the atomic

arrangements in a crystal, providing more and detailed information of defects through a contrast analysis. The TEM technique which has been accepted as the most powerful characterization method for defect observation can demonstrate the generation, propagation and termination of various defects in semi-polar and non-polar III-nitride. A detailed introduction of TEM measurement will be presented in section 3.2.

Table 2.3: Summary of the defects in semi-polar and non-polar III nitrides with their Burgers vectors  $\mathbf{b}$  (or displacement vectors  $\mathbf{R}$ ), and the contrast analysis in TEM measurement.

Defect type	Burgers (displacement) vector $\mathbf{b}(\mathbf{R})$	Diffraction vector $\mathbf{g}$						
		0002	11-20	1-100	2-200	3-300	1-101	1-212
$\mathbf{a}$ -type dislocation	$1/3\langle 11-20 \rangle$	-	Visible	-	-	-	-	Visible
$\mathbf{c}$ -type dislocation	$\langle 0001 \rangle$	Visible	-	-	-	-	Visible	Visible
$\mathbf{a}+\mathbf{c}$ mixed dislocation	$1/3\langle 11-23 \rangle$	Visible	Visible	-	-	-	Visible	Visible
Shockley PD *	$1/3\langle 1-100 \rangle$	-	-	Visible	Visible	Visible	Visible	Visible
Frank PD	$1/2\langle 0001 \rangle$	Visible	-	-	-	-	Visible	Visible
Frank-Shockley PD	$1/6\langle 2-203 \rangle$	Visible	-	Visible	Visible	Visible	Visible	Visible
Stair-rod dislocation	$1/6\langle 1-100 \rangle$	-	-	Visible	Visible	Visible	Visible	Visible
$I_1$ -type BSF	$1/6\langle 2-203 \rangle$	-	-	Visible	Visible	-	Visible	-
$I_2$ -type BSF	$1/3\langle 1-100 \rangle$	-	-	Visible	Visible	-	Visible	-
$E$ -type BSF	$1/2\langle 0001 \rangle$	-	-	-	-	-	Visible	-
PSF	$1/2\langle 10-11 \rangle$	-	-	Visible	-	Visible	-	-

\* PD: Partial dislocation

An invisibility criterion is usually employed to analyze defect types in TEM measurements.<sup>111-113</sup> Following a rule of thumb, a dislocation will be invisible when the scalar product of its Burgers vector  $\mathbf{b}$  and the diffraction vector  $\mathbf{g}$  is zero,  $\mathbf{g}\mathbf{b}=0$ , while it will be visible when the product is not zero. For example, an edge dislocation with a Burgers vector of  $1/3\langle 11-20 \rangle$  is invisible under the diffraction condition  $\mathbf{g}=0002$ , but in strong contrast under the diffraction condition  $\mathbf{g}=11-20$ . On the other hand, a stacking fault will be out of contrast when

the scalar product of displacement vector  $\mathbf{R}$  and the diffraction vector  $\mathbf{g}$  is an integer,  $\mathbf{g} \cdot \mathbf{b} = n$ . As a result,  $I_1$ -type BSFs are out of contrast under the diffraction condition  $\mathbf{g} = 0002$ , but they will be observable under  $\mathbf{g} = 1-100$ . It is worth noting that for the observation of a stacking fault, it not only needs to meet the rule of thumb, but also requires an edge-on configuration. In the edge-on configuration, the observation plane is perpendicular to the plane of the stacking fault. Table 2.3 summarizes the defects with different types in semi-polar and non-polar III-nitrides and the visibility information under various diffraction vectors.

### 2.4.3 Initiation, propagation and termination of defects

As mentioned above, defects, such as dislocations and BSFs, can significantly affect the performance of semi-polar or non-polar devices. It is essential to understand the origin, the propagation processes and the termination mechanisms of dislocations and BSFs in order to further improve the crystal quality of semi-polar and non-polar GaN.

For GaN grown on sapphire, the threading dislocations are mainly generated during the coalescence process of GaN islands that form as a result of an initial GaN nucleation layer using a standard two-step growth method on sapphire. As a result of the difference in rotation angle and tilting angle between the GaN islands, edge dislocations and screw dislocations could be formed around grain boundaries.<sup>114</sup> On the other hand, when the shear stress in the strained GaN exceeds a critical value, misfit dislocations can be generated along with two threading dislocations at its ends.<sup>115</sup> During the further growth process, dislocations will propagate along a certain direction to reach a minimum energy per unit growth length.<sup>116</sup> The propagation direction is related to the growth direction and the dislocation Burgers vector. Generally speaking, most of the dislocations will perpendicularly propagate to the film surface.

However, if a lateral overgrowth technique is used, the growth direction of the overgrown GaN layer changes during the overgrowth process, leading to the bending of dislocations occurring around the growth boundary.<sup>117</sup> Dislocations will either propagate to the sidewall of the overgrown layer or be blocked by the growth from other directions. An interaction between dislocations can happen when two dislocations meet each other. Consequently, a new dislocation will be generated with a new Burgers vector:  $\mathbf{b}_3 = \mathbf{b}_1 + \mathbf{b}_2$ . If the two dislocations have opposite Burgers vectors, an annihilation process will occur, thus terminating the two dislocations.<sup>118</sup>

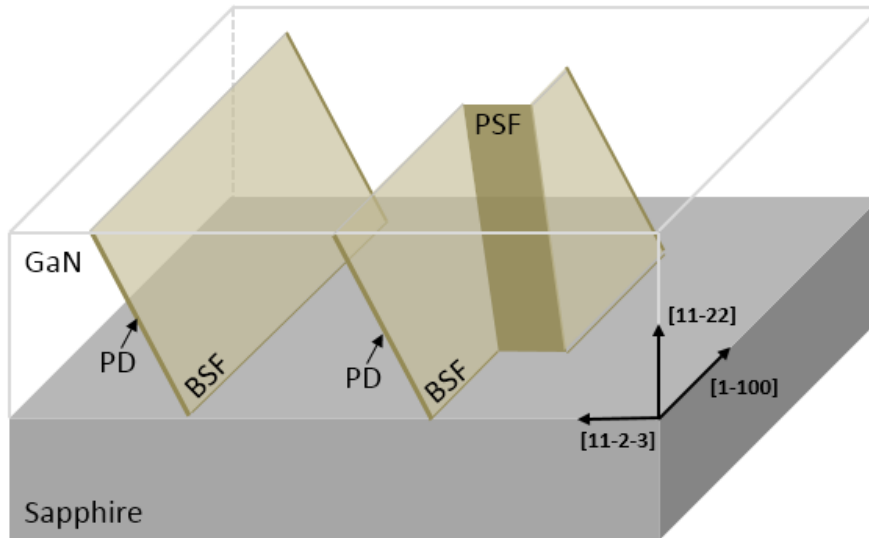


Figure 2.10: Schematic diagram of BSF and PSF in semi-polar (11-22) GaN on  $m$ -plane sapphire.

Stacking faults are formed at the interface between GaN and sapphire as a result of their lattice mismatch, where the BSFs mainly formed exhibit  $I_1$ -type due to the lowest formation energy and are lying in the basal plane. In the case of GaN grown along the  $c$ -direction, the stacking fault cannot propagate to any overlying layer, and thus will not be a problem for  $c$ -plane GaN. However, for semi-polar and non-polar GaN, the basal plane exhibits an inclination angle to the growth direction, allowing the BSF to penetrate to the sample surface. As shown in Figure 2.10, BSFs can be terminated either by partial dislocations (PDs) or PSF. An overgrowth technique which can be used to reduce dislocations is also an effective way to reduce BSFs. However, it is worth highlighting that the inclination angle between the stripe orientation and basal plane will reduce the possibility for BSFs being blocked.<sup>119</sup>

## 2.5 Optical properties of semi-polar and non-polar III-nitrides

### 2.5.1 Radiative recombination and non-radiative recombination

Recombination of electron-hole pairs in a semiconductor can take place in either a radiative recombination process leading to emitting photons or a non-radiative recombination process leading to the release of the energy in a form of lattice vibrations. In order to obtain highly efficient LEDs, the radiative recombination process is preferred while the non-radiative recombination processes need to be suppressed.

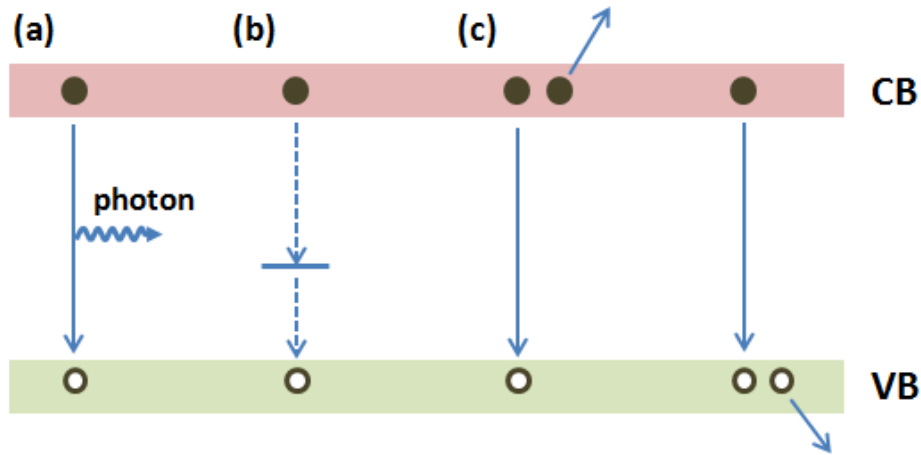


Figure 2.11: Possible recombination processes in III-nitrides. (a) Band-to-band radiative recombination. (b) Nonradiative recombination via extra deep energy level. (c) Auger recombination.

Radiative or non-radiative recombination processes can take place through a number of mechanisms as shown in Figure 2.11. The first one is a radiative recombination with transition between a conduction band and a valence band. A radiative recombination rate per unit time per unit volume can be described by the following equation:<sup>120</sup>

$$R = Bnp \quad (2.7)$$

where  $n$  and  $p$  are the electron and hole density in a semiconductor, and  $B$  is called the bimolecular recombination coefficient with a typical value of  $10^{-11}$ - $10^{-9}$   $\text{cm}^3/\text{s}$  for III-nitrides.

Figure 2.11b shows a non-radiative recombination process via a deep energy level, which is formed by defects such as vacancies, impurities and dislocations. The deep energy level located within the forbidden gap, in particular the one which is close to the middle of a bandgap, can easily trap carriers. A non-radiative recombination process can occur through so-called Auger recombination mechanism as shown in Figure 2.11c. For the Auger recombination, the recombination energy of the electron-hole pair is transferred to a third particle which can be either electron or hole. This particle can be excited into a higher energy level. Furthermore, a non-radiative recombination can take place through a surface recombination mechanism (not shown in figure).<sup>120</sup>

### 2.5.2 Stokes shift in III-nitrides

The Stokes shift is defined as an energy difference between absorption energy and emission energy. An introduction of absorption and emission processes will be given prior to the discussion of Stokes shift in III-nitrides.

#### Absorption

When a semiconductor is excited by a beam of light whose energy is higher than the bandgap of the semiconductor, electrons may be excited from its valence band to its conduction band. The absorption probability of the light depends on the photon energy.

$$\alpha(E) \propto (E - E_g)^{1/2} \quad (2.8)$$

The absorption coefficient exhibits a sharp absorption edge at the bandgap energy, while the absorption is supposed to be zero if the photon energy is lower than that of the bandgap. However, in a real situation, the absorption exhibits an exponential absorption curve (Figure 2.12) below the bandgap edge, which is usually referred as Urbach tail. The Urbach tail follows the equation:

$$\alpha(E) = \alpha_0 e^{(E-E_g)/E_{Urbach}} \quad (2.9)$$

where  $\alpha_0$  is a constant and  $E_{Urbach}$  is the Urbach energy. The Urbach tail absorption is caused by the formation of extended energy levels below the bandgap, which is usually related to the potential fluctuations in a semiconductor.

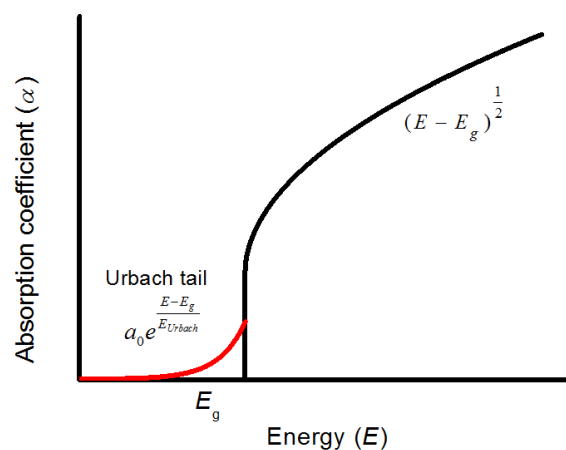


Figure 2.12: Absorption coefficient from a direct bandgap material.

## **Emission**

The electrons which are generated after being excited to the conduction band of a semiconductor will recombine with the holes formed as a result of the excitation process spontaneously, emitting photons if the electron-hole transition follows a radiative recombination process. This is called spontaneous emission. The transition rate via the spontaneous emission process depends on the transition matrix element which is determined by the overlap between electron and hole wave-functions. In a *c*-plane InGaN/GaN quantum well structure which suffers from piezoelectric fields, the band diagram will be tilted, leading the transition energy to be lower than that in a case without involving any internal field. Furthermore, the piezoelectric fields push the electrons and holes in opposite directions within the quantum well, reducing the overlap between electron and hole wave-functions and consequently lowering the radiative recombination rate.

## **Stokes shift**

After an absorption process, electrons are excited into higher energy states in the conduction band, as shown in Figure 2.13. Subsequently, the electrons quickly relax into the minima of the conduction band prior to any recombination process, thus leading to emission whose energy is smaller than the absorption energy in the case of a radiative recombination process. The energy difference between the absorption and emission is defined as Stokes shift as stated above. The Stokes shift in an InGaN/GaN quantum well structure depends on internal electrical fields and alloy fluctuations. The earliest study of the Stokes shift in InGaN/GaN quantum well structures can be dated back to 1996, reporting a large value of 100 meV in a *c*-plane blue LED.<sup>121</sup> For an InGaN/GaN MQW structure with Si doped GaN barriers, the Stokes shift exhibits a decrease with increasing doping concentration.<sup>122</sup> The Stokes shift in InGaN/GaN MQWs increases significantly with increasing quantum well thickness, as a result of increasing piezoelectric fields.<sup>123</sup> When increasing the indium composition in InGaN/GaN MQWs, both the piezoelectric fields and indium fluctuations are enhanced, leading to an increase in Stokes shift.

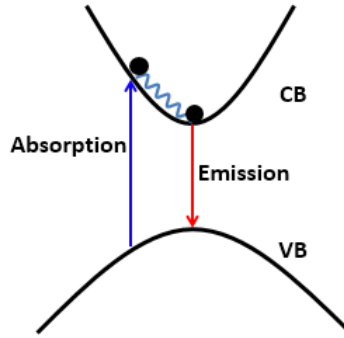


Figure 2.13: Schematic of the absorption and emission processes.

### 2.5.3 Carrier dynamics in InGaN/GaN MQWs along a semi-polar or non-polar orientation

Owing to the great development of GaN growth techniques along semi-polar and non-polar orientations, InGaN/GaN MQWs with impressive performance have been achieved on high quality GaN films, demonstrating some interesting properties such as short lifetime, polarized emission and enhanced carrier localization.

#### Reduced QCSE/lifetime

The most significant advantage of semi-polar or non-polar GaN is due to significant reduction or elimination in piezoelectric fields in InGaN/GaN MQWs. The reduction in internal electrical fields leads to an improvement in the overlap between electron and hole wave-functions and thus a reduction in carrier recombination lifetime. Figure 2.14 shows the comparative decay traces from a semi-polar (11-22) and a *c*-plane InGaN/GaN MQW structure measured at 10 K. A bi-exponential model was used to fit the decay traces. As denoted besides each curve, the fast component of the carrier recombination lifetime for the semi-polar sample is 46 ps, almost two orders of magnitude shorter than the 4.43 ns recombination lifetime for the *c*-plane counterpart, demonstrating a huge reduction in the internal piezoelectric fields in the semi-polar (11-22) sample compared with its *c*-plane counterpart. Furthermore, a fast recombination lifetime is crucial for the application of visible light wireless communications, where a modulation speed is inversely proportional to the recombination lifetime of the emitters used.<sup>124</sup>

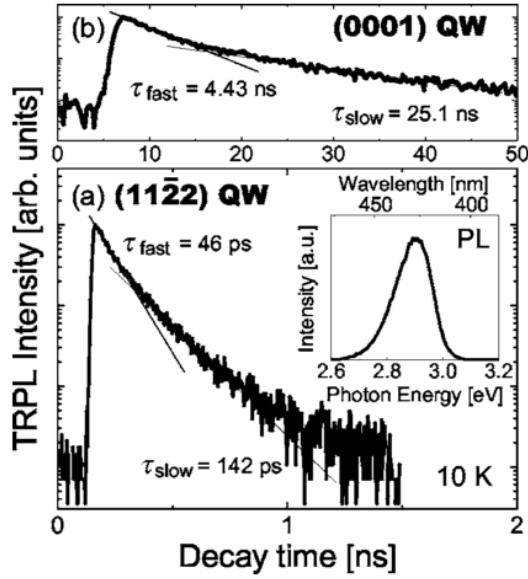


Figure 2.14: PL decay traces of InGaN/GaN MQWs grown on (11-22) plane and (0001) GaN measured at 10 K. Insert: PL spectrum of the semi-polar sample.<sup>125</sup>

Emission wavelengths can also be affected by the internal electrical fields in InGaN/GaN MQWs, leading to an increase in wavelength as a result of the QCSE induced by the piezoelectric fields. An increase in optical pumping can generate more electrons excited from the valence band of the MQWs to the conduction band. In this case, the internal electric fields can be partly screened as a result of the increasing excited carriers, leading to a blueshift in emission wavelength. This optical pumping induced blueshift in emission wavelength has been widely observed in *c*-plane InGaN/GaN MQWs, which is considered as a fingerprint of the existence of the QCSE. Figure 2.15 shows the normalized PL spectra as a function of excitation power density for *a*-plane and *c*-plane InGaN/GaN MQWs.<sup>126</sup> With increasing excitation power from 0.1 to 15 mW, the emission peak of the *c*-plane InGaN/GaN MQWs exhibits a clear blueshift, while the *a*-plane sample exhibits unchanged emission wavelength, demonstrating the absence of QCSE in the quantum well grown along a non-polar orientation. Furthermore, for a same emission wavelength, the indium composition in the *a*-plane sample will be higher than the *c*-plane sample due to the absence of QCSE. Thus, the *a*-plane sample shows broader peaks in the PL spectra than the *c*-plane sample.

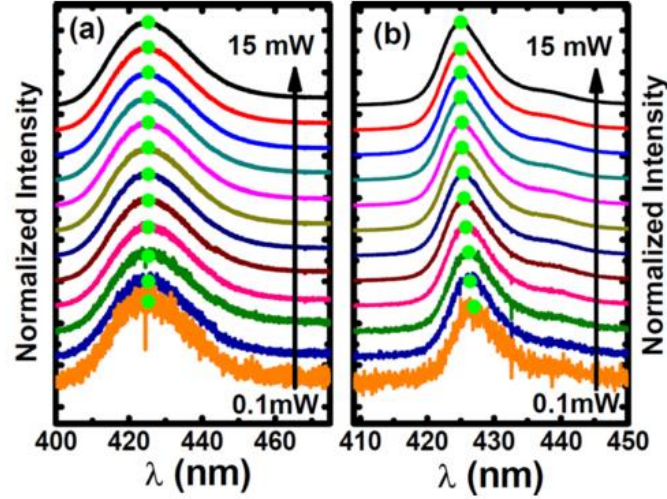


Figure 2.15: Normalized PL spectra of (a) *a*-plane and (b) *c*-plane InGaN/GaN MQWs as a function of excitation power measured at a low temperature.<sup>126</sup>

### Optical polarization

In wurtzite GaN, there exist three sub-bands in its valence bands at the Brillouin zone centre, labeled as  $\Gamma_{9v}$ ,  $\Gamma_{7v}^{\text{upper}}$  and  $\Gamma_{7v}^{\text{lower}}$ , which are referred to as heavy hole (HH), light hole (LH) and split-off hole (CH) sub-bands, respectively.<sup>127</sup> The carrier wave functions in the HH and the LH sub-bands exhibit  $|X \mp iY\rangle$ -like state, while the carriers in the CH sub-band has  $|Z\rangle$ -like state. The selection rule in quantum mechanics allows an interband transition between the conduction band and HH sub-band (or LH sub-band) when the electric field of incident light is perpendicular to the *c*-axis ( $E \perp c$ ). When the electric of the incident light is parallel to the *c*-axis ( $E \parallel c$ ), an interband transition between the conduction band and CH sub-band is allowed.<sup>128</sup> In a *c*-plane InGaN/GaN quantum well structure, the biaxial compressive strain has equal components along two orthogonal directions in a growth plane. As a result, the emission light exhibit isotropic characteristics viewed along the *c*-direction. When the InGaN/GaN quantum well structure is grown along a semi-polar or non-polar orientation, the strain field in the growth plane becomes anisotropic. This will lead to a change in the HH and LH sub-bands, from  $|X \mp iY\rangle$ -like bands into  $|X\rangle$ - and  $|Y\rangle$ -like bands, as shown in Figure 2.16.<sup>129</sup> The  $|X\rangle$ -like band moves up while the  $|Y\rangle$ -band moves down to below the  $|Z\rangle$ -like band. In this case, the interband transition between the conduction band and  $|X\rangle$ -like band (i.e.,  $E \perp c$ ) exhibits a lower emission energy than the transition between the conduction band and  $|Y\rangle$ -like band (i.e.,  $E \parallel c$ ). When the probability for the transition between the  $|X\rangle$ -like band and the conduction

(i.e.,  $E \perp c$ ) is higher than that for the transition between the  $|Y\rangle$ -like band and the conduction band (i.e.,  $E \parallel c$ ), the emission light will exhibit anisotropic characteristics along the growth direction, namely, a lower emission intensity along the  $c$ -direction.

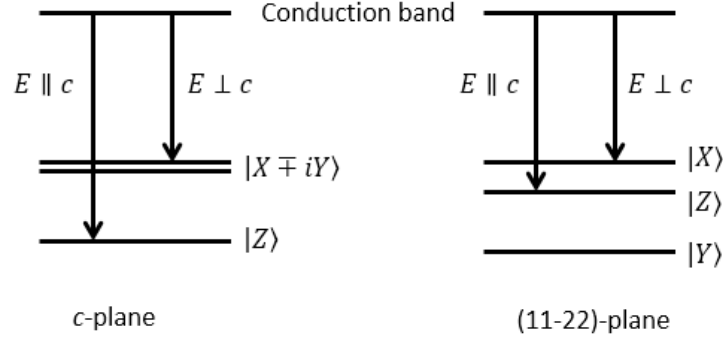


Figure 2.16: Schematic diagrams of conduction band and valence bands in compressively strained  $c$ -plane and semi-polar (11-22) GaN.

The polarization degree  $\rho$  could be evaluated by the following equation:

$$\rho = \left| \frac{I_{90^\circ} - I_{0^\circ}}{I_{90^\circ} + I_{0^\circ}} \right| \quad (2.10)$$

Here,  $I_{90^\circ}$  and  $I_{0^\circ}$  are the integrated PL intensities collected along a direction which is perpendicular and parallel to the  $c$ -axis, respectively. The value of the polarization degree  $\rho$  is in the range of 0 to 1. It is reported that the polarization degree increases with increasing indium composition in semi-polar and non-polar InGaN/GaN MQWs, as a result of the increasing anisotropy in strain field in a growth plane.<sup>130,131</sup> Blue LEDs with polarized emission play an important role in the fabrication of backlighting sources for computers, large displays, etc. The polarization degree in semi-polar (11-22) InGaN/GaN MQWs can be further enhanced by employing a photonic crystal structure.<sup>132</sup>

### Carrier localization

It has been widely accepted that carrier localization can significantly affect the optical properties of InGaN/GaN MQWs. In a semiconductor, carrier could occupy either a localized state or an extended state. The separation between the localized state and the extended state is defined as a mobility edge.<sup>133</sup> There are two kinds of major reasons for the origin of localization in InGaN/GaN MQWs. One is due to alloy compositional fluctuations as a result

of the immiscibility between InN and GaN, leading to indium segregation when the indium content exceeds 6%. The indium segregation is enhanced with increasing indium content. Another reason is due to thickness fluctuation in InGaN quantum wells. Theoretical calculations reveal that a monolayer thickness fluctuation in InGaN-based MQWs could lead to localization with a potential energy of about 60 meV.<sup>134</sup> It has been generally accepted that indium segregation induced localization plays a critical role in obtaining InGaN/GaN MQW based blue LEDs with high efficiency despite a high density existing in GaN grown on high lattice-mismatched sapphire.

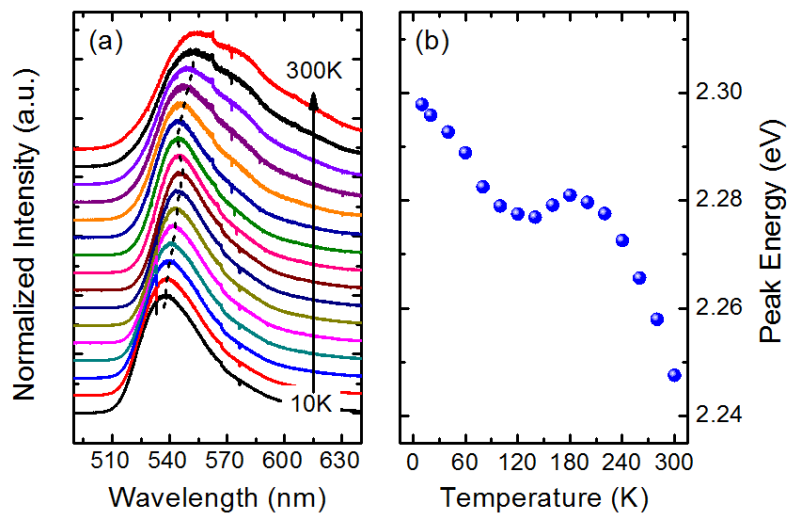


Figure 2.17: (a) Normalized PL spectra of *c*-plane InGaN/GaN MQWs under various temperatures. The spectra have been offset for clarity. (b) Emission peak energy as a function of temperature.

In order to confirm or observe exciton localization in an InGaN/GaN MQWs sample, temperature dependent PL measurements provide a simple but effective approach. Typically, the emission peak usually exhibits an ‘S-shape’ behaviour with increasing temperature, which is a finger-print for exciton localization. For example, Figure 2.17a shows PL emission spectra at different temperatures from a *c*-plane InGaN/GaN MQWs sample with emission peak around 540 nm. All the PL spectra have been normalized and offset for clarity. With increasing temperature from a low temperature (10K) to room temperature, the emission peak starts to red-shift, followed by a blueshift, and then red-shift again. The first redshift is related to the migration of localized carriers from higher energy levels to lower energy levels at low temperature. When the temperature increases to a mediate temperature region, nonradiative

recombination becomes pronounced. Many carriers are able to recombine nonradiatively before reaching a lower energy level, leading to a blueshift in the emission peak. The final stage of the second redshift is a result of the thermal dilation of the crystal lattice at elevated temperature region.

## References

- 1 S. Nakamura, S. Pearton, and G. Fasol, *The Blue Laser Diode* (Springer Berlin Heidelberg, Berlin, Heidelberg, 2000).
- 2 H. Xia, Q. Xia, and A. L. Ruoff, *Phys. Rev. B* **47**, 12925 (1993).
- 3 J. H. Kim and P. H. Holloway, *Appl. Phys. Lett.* **84**, 711 (2004).
- 4 C. H. Wei, Z. Y. Xie, L. Y. Li, Q. M. Yu, and J. H. Edgar, *J. Electron. Mater.* **29**, 317 (2000).
- 5 I. Vurgaftman and J. R. Meyer, *J. Appl. Phys.* **94**, 3675 (2003).
- 6 P. Kidd, *XRD of Gallium Nitride and Related Compounds: Strain, Composition and Layer Thickness* (Panalytical, Almelo, 2009).
- 7 A. Argoitia, J. C. Angus, C. C. Hayman, L. Wang, J. S. Dyck, and K. Kash, *MRS Proc.* **449**, 2411 (1996).
- 8 F. Bernardini, V. Fiorentini, and D. Vanderbilt, *Phys. Rev. B* **56**, R10024 (1997).
- 9 E. T. Yu, X. Z. Dang, P. M. Asbeck, S. S. Lau, and G. J. Sullivan, *J. Vac. Sci. Technol. B Microelectron. Nanom. Struct.* **17**, 1742 (1999).
- 10 M. E. Vickers, J. L. Hollander, C. McAleese, M. J. Kappers, M. A. Moram, and C. J. Humphreys, *J. Appl. Phys.* **111**, 43502 (2012).
- 11 T. Takeuchi, S. Sota, M. Katsuragawa, M. Komori, H. Takeuchi, H. Amano, and I. Akasaki, *Jpn. J. Appl. Phys.* **36**, L382 (1997).
- 12 Y. D. Jho, J. S. Yahng, E. Oh, and D. S. Kim, *Appl. Phys. Lett.* **79**, 1130 (2001).
- 13 G. Franssen, T. Suski, P. Perlin, R. Bohdan, A. Bercha, W. Trzeciakowski, I. Makarowa, P. Prystawko, M. Leszczyński, I. Grzegory, S. Porowski, and S. Kokenyesi, *Appl. Phys. Lett.* **87**, 41109 (2005).
- 14 T. Deguchi, A. Shikanai, K. Torii, T. Sota, S. Chichibu, and S. Nakamura, *Appl. Phys. Lett.* **72**, 3329 (1998).
- 15 C. S. Kim, H. G. Kim, C. H. Hong, and H. K. Cho, *Appl. Phys. Lett.* **87**, 13502 (2005).
- 16 T. Asano, T. Tojyo, T. Mizuno, M. Takeya, S. Ikeda, K. Shibuya, T. Hino, S. Uchida, and M. Ikeda, *IEEE J. Quantum Electron.* **39**, 135 (2003).
- 17 J. H. Ryou, W. Lee, J. Limb, D. Yoo, J. P. Liu, R. D. Dupuis, Z. H. Wu, A. M. Fischer, and F. A. Ponce, *Appl. Phys. Lett.* **92**, 101113 (2008).
- 18 P. Kivisaari, J. Oksanen, and J. Tulkki, *Appl. Phys. Lett.* **103**, 211118 (2013).
- 19 T. Takeuchi, H. Amano, and I. Akasaki, *Jpn. J. Appl. Phys.* **39**, 413 (2000).
- 20 A. E. Romanov, T. J. Baker, S. Nakamura, and J. S. Speck, *J. Appl. Phys.* **100**, 23522 (2006).
- 21 J. E. Northrup, *Appl. Phys. Lett.* **95**, 133107 (2009).
- 22 J. E. Northrup, *Phys. Rev. B* **79**, 41306 (2009).
- 23 A. Strittmatter, J. E. Northrup, N. M. Johnson, M. V. Kisin, P. Spiberg, H. El-Ghoroury,

- A. Usikov, and A. Syrkin, *Phys. Status Solidi* **248**, 561 (2011).
- 24 T. Wernicke, L. Schade, C. Netzel, J. Rass, V. Hoffmann, S. Ploch, A. Knauer, M. Weyers, U. Schwarz, and M. Kneissl, *Semicond. Sci. Technol.* **27**, 24014 (2012).
  - 25 Y. Zhao, Q. Yan, C. Y. Huang, S. C. Huang, P. Shan Hsu, S. Tanaka, C. C. Pan, Y. Kawaguchi, K. Fujito, C. G. Van de Walle, J. S. Speck, S. P. DenBaars, S. Nakamura, and D. Feezell, *Appl. Phys. Lett.* **100**, 201108 (2012).
  - 26 S. C. Cruz, S. Keller, T. E. Mates, U. K. Mishra, and S. P. DenBaars, *J. Cryst. Growth* **311**, 3817 (2009).
  - 27 N. A. Fichtenbaum, T. E. Mates, S. Keller, S. P. DenBaars, and U.K. Mishra, *J. Cryst. Growth* **310**, 1124 (2008).
  - 28 N. A. Fichtenbaum, C. Schaake, T. E. Mates, C. Cobb, S. Keller, S. P. DenBaars, and U. K. Mishra, *Appl. Phys. Lett.* **91**, 172105 (2007).
  - 29 H. Xing, D. S. Green, H. Yu, T. Mates, P. Kozodoy, S. Keller, S. P. DenBaars, and U.K. Mishra, *Jpn. J. Appl. Phys.* **42**, 50 (2003).
  - 30 M. McLaurin, T. E. Mates, and J. S. Speck, *Appl. Phys. Lett.* **86**, 262104 (2005).
  - 31 Y. Tsuchiya, Y. Okadome, A. Honshio, Y. Miyake, T. Kawashima, M. Iwaya, S. Kamiyama, H. Amano, and I. Akasaki, *Jpn. J. Appl. Phys.* **44**, L1516 (2005).
  - 32 J. F. Kaeding, H. Asamizu, H. Sato, M. Iza, T. E. Mates, S. P. DenBaars, J. S. Speck, and S. Nakamura, *Appl. Phys. Lett.* **89**, 202104 (2006).
  - 33 S. Park, *J. Appl. Phys.* **91**, 9904 (2002).
  - 34 H. P. Maruska, L. J. Anderson, and D. A. Stevenson, *J. Electrochem. Soc.* **121**, 1202 (1974).
  - 35 M. Sano and M. Aoki, *Jpn. J. Appl. Phys.* **15**, 1943 (1976).
  - 36 A. Shintani, *J. Electrochem. Soc.* **123**, 1575 (1976).
  - 37 T. Sasaki and S. Zembutsu, *J. Appl. Phys.* **61**, 2533 (1987).
  - 38 R. Madar, D. Michel, G. Jacob, and M. Boulou, *J. Cryst. Growth* **40**, 239 (1977).
  - 39 T. Lei, K. F. Ludwig, and T. D. Moustakas, *J. Appl. Phys.* **74**, 4430 (1993).
  - 40 W. A. Melton and J. I. Pankove, *J. Cryst. Growth* **178**, 168 (1997).
  - 41 P. Waltereit, O. Brandt, A. Trampert, H. Grahn, J. Menniger, M. Ramsteiner, M. Reiche, and K. Ploog, *Nature* **406**, 865 (2000).
  - 42 H. M. Ng, *Appl. Phys. Lett.* **80**, 4369 (2002).
  - 43 M. D. Craven, S. H. Lim, F. Wu, J. S. Speck, and S. P. Denbaars, *Appl. Phys. Lett.* **81**, 469 (2002).
  - 44 C. Q. Chen, M. E. Gaevski, W. H. Sun, E. Kuokstis, J. P. Zhang, R. S. Q. Fareed, H. M. Wang, J. W. Yang, G. Simin, M. A. Khan, H. P. Maruska, D.W. Hill, M. M. C. Chou, and B. Chai, *Appl. Phys. Lett.* **81**, 3194 (2002).
  - 45 M. D. Craven, P. Waltereit, F. Wu, J. S. Speck, and S. P. DenBaars, *Jpn. J. Appl. Phys.* **42**, L235 (2003).

- 46 B. A. Haskell, F. Wu, M. D. Craven, S. Matsuda, P. T. Fini, T. Fujii, K. Fujito, S. P. DenBaars, J. S. Speck, and S. Nakamura, *Appl. Phys. Lett.* **83**, 644 (2003).
- 47 K. Nishizuka, M. Funato, Y. Kawakami, S. Fujita, Y. Narukawa, and T. Mukai, *Appl. Phys. Lett.* **85**, 3122 (2004).
- 48 F. Schulze, A. Dadgar, J. Bläsing, and A. Krost, *Appl. Phys. Lett.* **84**, 4747 (2004).
- 49 A. Chakraborty, B. A. Haskell, S. Keller, J. S. Speck, S. P. Denbaars, S. Nakamura, and U. K. Mishra, *Appl. Phys. Lett.* **85**, 5143 (2004).
- 50 A. Chakraborty, B. A. Haskell, S. Keller, J. S. Speck, S. P. Denbaars, S. Nakamura, and U. K. Mishra, *Jpn. J. Appl. Phys.* **44**, L173 (2005).
- 51 D. N. Zakharov, Z. Liliental-Weber, B. Wagner, Z. J. Reitmeier, E. A. Preble, and R. F. Davis, *Phys. Rev. B* **71**, 235334 (2005).
- 52 T. J. Baker, B. A. Haskell, F. Wu, P. T. Fini, J. S. Speck, and S. Nakamura, *Jpn. J. Appl. Phys.* **44**, L920 (2005).
- 53 A. Chakraborty, T. J. Baker, B. A. Haskell, F. Wu, J. S. Speck, S. P. Denbaars, S. Nakamura, and U. K. Mishra, *Jpn. J. Appl. Phys.* **44**, L945 (2005).
- 54 T. J. Baker, B. A. Haskell, F. Wu, J. S. Speck, and S. Nakamura, *Jpn. J. Appl. Phys.* **45**, L154 (2006).
- 55 M. Funato, M. Ueda, Y. Kawakami, Y. Narukawa, T. Kosugi, M. Takahashi, and T. Mukai, *Jpn. J. Appl. Phys.* **45**, L659 (2006).
- 56 T. Wunderer, P. Brückner, B. Neubert, F. Scholz, M. Feneberg, F. Lipski, M. Schirra, and K. Thonke, *Appl. Phys. Lett.* **89**, 41121 (2006).
- 57 A. Kobayashi, S. Kawano, Y. Kawaguchi, J. Ohta, and H. Fujioka, *Appl. Phys. Lett.* **90**, 41908 (2007).
- 58 A. Tyagi, H. Zhong, N. N. Fellows, M. Iza, J. S. Speck, S. P. DenBaars, and S. Nakamura, *Jpn. J. Appl. Phys.* **46**, L129 (2007).
- 59 M. C. Schmidt, K. C. Kim, R. M. Farrell, D. F. Feezell, D. A. Cohen, M. Saito, K. Fujito, J. S. Speck, S. P. DenBaars, and S. Nakamura, *Jpn. J. Appl. Phys.* **46**, L190 (2007).
- 60 L. Lahourcade, E. Bellet-Amalric, E. Monroy, M. P. Chauvat, and P. Ruterana, *J. Mater. Sci. Mater. Electron.* **19**, 805 (2007).
- 61 B. Liu, R. Zhang, Z. L. Xie, C. X. Liu, J. Y. Kong, J. Yao, Q. J. Liu, Z. Zhang, D. Y. Fu, X. Q. Xiu, H. Lu, P. Chen, P. Han, S. L. Gu, Y. Shi, Y. D. Zheng, J. Zhou, and S. M. Zhou, *Appl. Phys. Lett.* **91**, 253506 (2007).
- 62 R. Armitage and H. Hirayama, *Appl. Phys. Lett.* **92**, 92121 (2008).
- 63 L. Zhou, R. Chandrasekaran, T. D. Moustakas, and D. J. Smith, *J. Cryst. Growth* **310**, 2981 (2008).
- 64 H. Asamizu, M. Saito, K. Fujito, J. S. Speck, S. P. DenBaars, and S. Nakamura, *Appl. Phys. Express* **1**, 91102 (2008).
- 65 T. Tanikawa, D. Rudolph, T. Hikosaka, Y. Honda, M. Yamaguchi, and N. Sawaki, *J. Cryst. Growth* **310**, 4999 (2008).

- 66 K. Ueno, A. Kobayashi, J. Ohta, H. Fujioka, H. Amanai, S. Nagao, and H. Horie, *Phys. Status Solidi - Rapid Res. Lett.* **3**, 58 (2009).
- 67 T. Zhu, D. Martin, and N. Grandjean, *Jpn. J. Appl. Phys.* **48**, 20226 (2009).
- 68 N. Sawaki, T. Hikosaka, N. Koide, S. Tanaka, Y. Honda, and M. Yamaguchi, *J. Cryst. Growth* **311**, 2867 (2009).
- 69 N. Suzuki, T. Uchida, T. Tanikawa, T. Hikosaka, Y. Honda, M. Yamaguchi, and N. Sawaki, *J. Cryst. Growth* **311**, 2875 (2009).
- 70 Y. Enya, Y. Yoshizumi, T. Kyono, K. Akita, M. Ueno, M. Adachi, T. Sumitomo, S. Tokuyama, T. Ikegami, K. Katayama, and T. Nakamura, *Appl. Phys. Express* **2**, 82101 (2009).
- 71 X. Ni, M. Wu, J. Lee, X. Li, A. A. Baski, Ü. Özgür, and H. Morkoç, *Appl. Phys. Lett.* **95**, 111102 (2009).
- 72 P. S. Hsu, K. M. Kelchner, A. Tyagi, R. M. Farrell, D. A. Haeger, K. Fujito, H. Ohta, S. P. DenBaars, J. S. Speck, and S. Nakamura, *Appl. Phys. Express* **3**, 52702 (2010).
- 73 S. Schwaiger, I. Argut, T. Wunderer, R. Rösch, F. Lipski, J. Biskupek, U. Kaiser, and F. Scholz, *Appl. Phys. Lett.* **96**, 231905 (2010).
- 74 I. L. Koslow, J. Sonoda, R. B. Chung, C. C. Pan, S. Brinkley, H. Ohta, S. Nakamura, and S. P. DenBaars, *Jpn. J. Appl. Phys.* **49**, 80203 (2010).
- 75 T. Fujii, A. Kobayashi, J. Ohta, M. Oshima, and H. Fujioka, *Phys. Status Solidi* **207**, 2269 (2010).
- 76 H. Murakami, H. Chol Cho, M. Suematsu, R. Togashi, Y. Kumagai, R. Toba, and A. Koukitu, *J. Cryst. Growth* **318**, 479 (2011).
- 77 Y. Zhao, S. Tanaka, Q. Yan, C. Y. Huang, R. B. Chung, C. C. Pan, K. Fujito, D. Feezell, C. G. Van de Walle, J. S. Speck, S. P. DenBaars, and S. Nakamura, *Appl. Phys. Lett.* **99**, 51109 (2011).
- 78 C. Y. Huang, M. T. Hardy, K. Fujito, D. F. Feezell, J. S. Speck, S. P. DenBaars, and S. Nakamura, *Appl. Phys. Lett.* **99**, 241115 (2011).
- 79 C. Y. Hsieh, B. W. Lin, W. H. Cheng, B. M. Wang, L. Chang, and Y. S. Wu, *ECS J. Solid State Sci. Technol.* **1**, R54 (2012).
- 80 P. Gupta, A. A. Rahman, N. Hatui, M. R. Gokhale, M. M. Deshmukh, and A. Bhattacharya, *J. Cryst. Growth* **372**, 105 (2013).
- 81 J. Yang, F. Yang, T. F. Kent, M. J. Mills, and R. C. Myers, *Appl. Phys. Lett.* **103**, 121105 (2013).
- 82 M. Houry, M. Leroux, M. Nemoz, G. Feuillet, J. Zúñiga-Pérez, and P. Vennéguès, *J. Cryst. Growth* **419**, 88 (2015).
- 83 D. V. Dinh, S. Presa, M. Akhter, P. P. Maaskant, B. Corbett, and P. J. Parbrook, *Semicond. Sci. Technol.* **30**, 125007 (2015).
- 84 J. Bai, B. Xu, F. G. Guzman, K. Xing, Y. Gong, Y. Hou, and T. Wang, *Appl. Phys. Lett.* **107**, 261103 (2015).
- 85 E.S. Hellman, Z. Liliental-Weber, and D. N. E. Buchanan, *MRS Internet J. Nitride*

- Semicond. Res. **2**, e30 (1997).
- 86 W. Wang, W. Yang, H. Wang, and G. Li, *J. Mater. Chem. C* **2**, 9342 (2014).
- 87 A. Elasser and T. P. Chow, *Proc. IEEE* **90**, 969 (2002).
- 88 V. Pishchik, L. A. Lytvynov, and E. R. Dobrovinskaya, *Sapphire* (Springer US, Boston, MA, 2009).
- 89 D. Zhu, D. J. Wallis, and C. J. Humphreys, *Rep. Prog. Phys.* **76**, 106501 (2013).
- 90 H. Ishikawa, K. Yamamoto, T. Egawa, T. Soga, T. Jimbo, and M. Umeno, *J. Cryst. Growth* **189–190**, 178 (1998).
- 91 N. Okada, A. Kurisu, K. Murakami, and K. Tadatomo, *Appl. Phys. Express* **2**, 091001 (2009).
- 92 F. Tendille, P. De Mierry, P. Vennéguès, S. Chenot, and M. Teisseire, *J. Cryst. Growth* **404**, 177 (2014).
- 93 N. Okada and K. Tadatomo, *Semicond. Sci. Technol.* **27**, 24003 (2012).
- 94 J. Bai, X. Yu, Y. Gong, Y. N. Hou, Y. Zhang, and T. Wang, *Semicond. Sci. Technol.* **30**, 065012 (2015).
- 95 T. S. Zheleva, O. H. Nam, W. M. Ashmawi, J. D. Griffin, and R. F. Davis, *J. Cryst. Growth* **222**, 706 (2001).
- 96 B. A. Haskell, T. J. Baker, M. B. McLaurin, F. Wu, P. T. Fini, S. P. DenBaars, J. S. Speck, and S. Nakamura, *Appl. Phys. Lett.* **86**, 111917 (2005).
- 97 X. Ni, U. Özgür, Y. Fu, N. Biyikli, J. Xie, A. A. Baski, H. Morkoç, and Z. Liliental-Weber, *Appl. Phys. Lett.* **89**, 262105 (2006).
- 98 X. Ni, U. Özgür, A. A. Baski, H. Morkoç, L. Zhou, D. J. Smith, and C. A. Tran, *Appl. Phys. Lett.* **90**, 182109 (2007).
- 99 Y. Gong, K. Xing, J. Bai, and T. Wang, *Phys. Status Solidi* **9**, 564 (2012).
- 100 J. Bai, Y. Gong, K. Xing, X. Yu, and T. Wang, *Appl. Phys. Lett.* **102**, 101906 (2013).
- 101 K. Xing, Y. Gong, X. Yu, J. Bai, and T. Wang, *Jpn. J. Appl. Phys.* **52**, 08JC03 (2013).
- 102 B. Xu, X. Yu, Y. Gong, K. Xing, J. Bai, and T. Wang, *Phys. Status Solidi* **252**, 1079 (2015).
- 103 Y. Zhang, J. Bai, Y. Hou, R. M. Smith, X. Yu, Y. Gong, and T. Wang, *AIP Adv.* **6**, 25201 (2016).
- 104 Y. A. Osipiyan and I. S. Smirnova, *Phys. Status Solidi* **30**, 19 (1968).
- 105 J. W. Matthews and A. E. Blakeslee, *J. Cryst. Growth* **27**, 118 (1974).
- 106 A. Tyagi, F. Wu, E. C. Young, A. Chakraborty, H. Ohta, R. Bhat, K. Fujito, S. P. DenBaars, S. Nakamura, and J. S. Speck, *Appl. Phys. Lett.* **95**, 251905 (2009).
- 107 J. E. Northrup, *Appl. Phys. Lett.* **72**, 2316 (1998).
- 108 P. Visconti, K. Jones, M. Reshchikov, R. Cingolani, and H. Morkoc, *Appl. Phys. Lett.* **77**, 3532 (2000).
- 109 C. H. Seager, S. M. Myers, G. A. Petersen, J. Han, and T. Headley, *J. Appl. Phys.* **85**,

- 2568 (1999).
- 110 M. A. Moram and M. E. Vickers, *Reports Prog. Phys.* **72**, 36502 (2009).
  - 111 D. B. Williams and C. B. Carter, *Transmission Electron Microscopy* (Springer US, Boston, MA, 2009).
  - 112 F. A. Ponce, D. Cherns, W.T. Young, and J. W. Steeds, *Appl. Phys. Lett.* **69**, 770 (1996).
  - 113 D. M. Follstaedt, N. A. Missert, D. D. Koleske, C. C. Mitchell, and K. C. Cross, *Appl. Phys. Lett.* **83**, 4797 (2003).
  - 114 X. J. Ning, F. R. Chien, P. Pirouz, J. W. Yang, and M. A. Khan, *J. Mater. Res.* **11**, 580 (1996).
  - 115 Z. Feng, E. Lovell, R. Engelstad, T. Kuech, and S. Babcock, *Appl. Phys. Lett.* **80**, 1547 (2002).
  - 116 A. Sakai, H. Sunakawa, A. Kimura, and A. Usui, *J. Electron Microsc.* **49**, 323 (2000).
  - 117 S. Gradečak, P. Stadelmann, V. Wagner, and M. Ilegems, *Appl. Phys. Lett.* **85**, 4648 (2004).
  - 118 S. K. Mathis, A. E. Romanov, L. F. Chen, G. E. Beltz, W. Pompe, and J. S. Speck, *J. Cryst. Growth* **231**, 371 (2001).
  - 119 Z. Bougrioua, M. Laügt, P. Vennéguès, I. Cestier, T. Günne, E. Frayssinet, P. Gibart, and M. Leroux, *Phys. Status Solidi* **204**, 282 (2007).
  - 120 E. F. Schubert, *Light Emitting Diodes* (Cambridge University Press, London, 2006).
  - 121 S. Nakamura, *Adv. Mater.* **8**, 689 (1996).
  - 122 Y. H. Cho, J. J. Song, S. Keller, M. S. Minsky, E. Hu, U.K. Mishra, and S. P. DenBaars, *Appl. Phys. Lett.* **73**, 1128 (1998).
  - 123 E. Berkowicz, D. Gershoni, G. Bahir, E. Lakin, D. Shilo, E. Zolotoyabko, A.C. Abare, S. P. Denbaars, and L. A. Coldren, *Phys. Rev. B* **61**, 10994 (2000).
  - 124 T. Komine and M. Nakagawa, *IEEE Trans. Consum. Electron.* **50**, 100 (2004).
  - 125 M. Ueda, K. Kojima, M. Funato, Y. Kawakami, Y. Narukawa, and T. Mukai, *Appl. Phys. Lett.* **89**, 211907 (2006).
  - 126 K. Xing, Y. Gong, J. Bai, and T. Wang, *Appl. Phys. Lett.* **99**, 181907 (2011).
  - 127 S. Ghosh, P. Waltereit, O. Brandt, H. Grahn, and K. Ploog, *Phys. Rev. B* **65**, 75202 (2002).
  - 128 S. Chichibu, T. Azuhata, T. Sota, and S. Nakamura, *J. Appl. Phys.* **79**, 2784 (1996).
  - 129 E. Matioli, S. Brinkley, K. M. Kelchner, Y. L. Hu, S. Nakamura, S. DenBaars, J. Speck, and C. Weisbuch, *Light Sci. Appl.* **1**, e22 (2012).
  - 130 H. Yamada, K. Iso, M. Saito, H. Masui, K. Fujito, S. P. DenBaars, and S. Nakamura, *Appl. Phys. Express* **1**, 41101 (2008).
  - 131 N. Fellows, H. Sato, H. Masui, S. P. DenBaars, and S. Nakamura, *Jpn. J. Appl. Phys.* **47**, 7854 (2008).
  - 132 M. Athanasiou, R. M. Smith, Y. Hou, Y. Zhang, Y. Gong, and T. Wang, *Appl. Phys.*

- Lett. **107**, 141110 (2015).
- 133 N. F. Mott, Rev. Mod. Phys. **40**, 677 (1968).
- 134 C. J. Humphreys, Philos. Mag. **87**, 1971 (2007).
- 135 Q. Yan, P. Rinke, A. Janotti, M. Scheffler, and C. G. Van de Walle, Phys. Rev. B **90**, 125118 (2014).
- 136 I. Ho, and G. B. Stringfellow, Appl. Phys. Lett. **69**, 2701 (1996).



## Experimental techniques

---

Multiple characterization techniques were employed in this research project to investigate the semi-polar (11-22) III-nitrides, in terms of optical and structural properties. In this chapter, optical characterization methods including photoluminescence (PL), photoluminescence excitation (PLE), time-resolved PL and micro-PL will be explained, followed by an introduction to the transmission electron microscopy (TEM) characterization technique, and specimen preparation methods as well. Furthermore, an overgrowth technique on regularly arrayed micro-rod templates used in obtaining high-quality semi-polar (11-22) GaN films is also briefly presented.

### 3.1 Optical characterization

#### 3.1.1 Photoluminescence

Photoluminescence (PL) is one of the most powerful characterization techniques for investigating the optical properties of semiconductors. It is a non-destructive characterization method. When a beam of light is incident on a semiconductor sample, the light is absorbed by the semiconductor if the photon energy of the light is larger than the bandgap energy of the semiconductor. After the absorption process, electrons are excited to the conduction band from the valence band, leaving holes in the valence band. The electrons will then recombine with the holes. In the case of a radiative recombination process, photons are emitted. The emission from the semiconductor can be collected and analyzed to study the optical properties of the semiconductor.

Figure 3.1 schematically illustrates a setup of our PL system which is equipped with two lasers, where a 325 nm He-Cd laser is used to study the optical properties of GaN and a 375 nm diode laser with its energy smaller than the GaN bandgap is typically used to characterize InGaN/GaN quantum well structures. Using a reflection mirror and a focus lens, the laser can be focused on a sample with a spot diameter of around 200  $\mu\text{m}$ . A helium closed-cycle cryostat is used for performing temperature dependent PL measurements with a temperature range from

10 K to 300 K. Through a pair of focusing lenses, emission can be focused and then collected by a 500 mm monochromator. Finally, the emission is detected by a thermoelectric (TE) cooled charge-coupled device (CCD) detector with a working temperature at  $-70\text{ }^{\circ}\text{C}$ . Both temperature dependent PL and power dependent PL measurements can be performed on III-nitride samples.

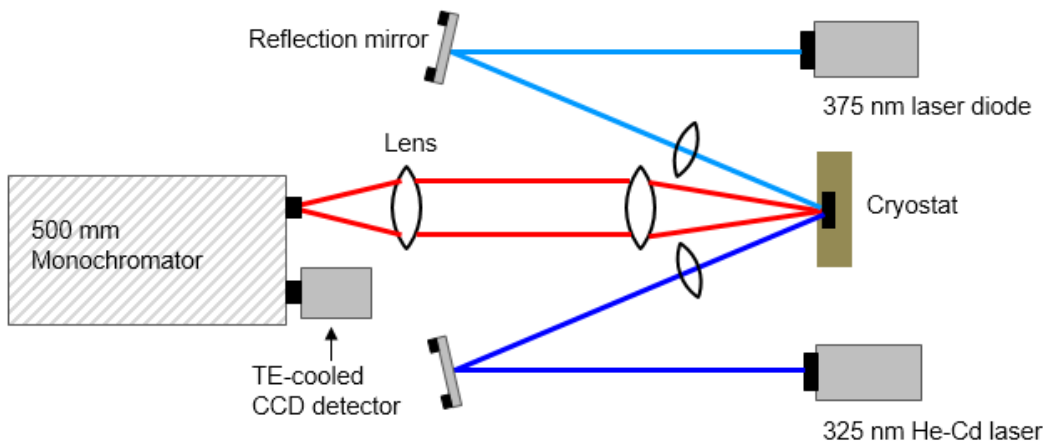


Figure 3.1: Schematic diagram of a PL system equipped with two laser sources.

### 3.1.2 Photoluminescence excitation

Photoluminescence excitation (PLE) spectroscopy is a characterization method allowing us to record the emission intensity at a certain wavelength under a range of excitation energy by fixing a detection wavelength and continuously changing excitation wavelength. Although PLE spectroscopy can be treated as an absorption spectrum to some degree, it is actually different from an absorption spectrum. The relaxation of the photogenerated carriers to lower energy states is notably fast and this process can be finished before any luminescence process. Compared with absorption measurements, a PLE measurement has an advantage of measuring any non-transparent materials. Furthermore, the recorded light intensity at a fixed wavelength comes from a certain luminescent layer, depending on its bandgap. This makes it suitable for measuring the absorption edge of a quantum well. For example, Figure 3.2 shows the PL and PLE spectra from a semi-polar (11-22) InGaN/GaN dual-wavelength multiple quantum wells (MQWs) structure. With a detection wavelength fixed at the yellow emission peak, three absorption edges related to the GaN barrier, blue quantum well and yellow quantum well have been observed in the PLE spectra, as marked by black arrows.

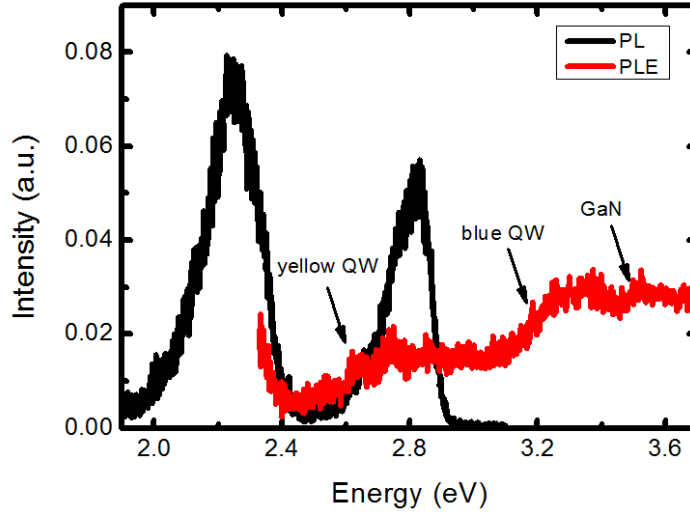


Figure 3.2: PL and PLE spectra from a semi-polar (11-22) InGaN/GaN dual-wavelength multiple quantum well structure.

Figure 3.3 shows a schematic diagram of a PLE system used throughout the research project. A LDLS™ Laser-Driven Light Source is used as an excitation light source. In the light source, a continuous-wavelength (cw) laser is focused onto a Xenon plasma, which radiates high brightness light in a spectral range from 170 nm to 2100 nm, namely, from the ultraviolet through the visible to the infrared.<sup>1</sup> A 320 mm monochromator is used to disperse the bright excitation light into a monochromatic light. Instead of using a lens, a pair of parabolic mirrors are employed to focus the monochromatic light onto a sample, where the influence of chromatic aberration in optical lens can be easily excluded. A certain angle between the incident light and the sample normal is required to minimize Fabry-Perot interference oscillations. The sample is loaded in a helium closed-cycle cryostat with a working temperature from 12 K to 300 K. The emission light is dispersed by another 550 mm monochromator before being detected by a GaAs photocathode photomultiplier tube (PMT) with a cooling system. For each measurement, a silicon photodiode is used to record the excitation light intensity as a function of wavelength to calibrate experimental results.

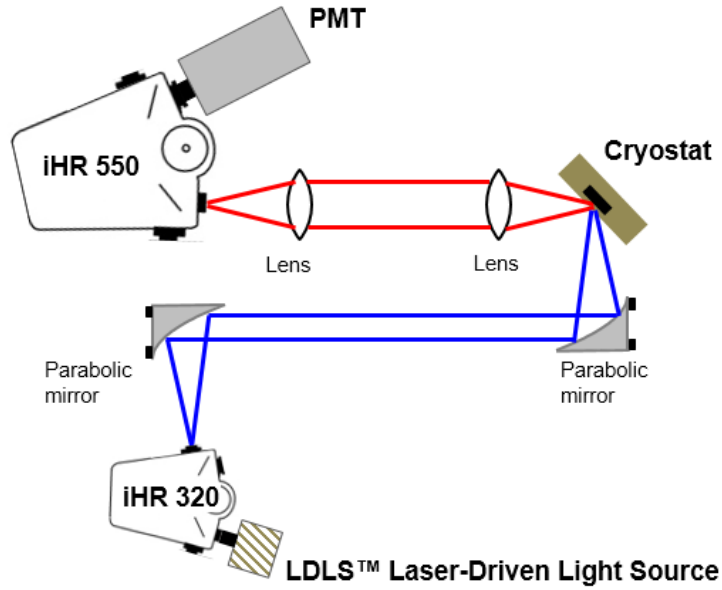


Figure 3.3: A schematic diagram of our PLE system.

### 3.1.3 Time-resolved photoluminescence

Time-resolved photoluminescence (TRPL) is a powerful characterization method for investigating excitonic recombination dynamics in a semiconductor. Considering a time-dependent recombination process, photons with a number of  $A_1$  will be emitted in a certain time interval  $t_1$ , followed by a number of  $A_2$  photons emitted in another time interval  $t_2$ , as a histogram illustrates in Figure 3.4. If the time interval is small enough, the number of the emitted photons as a function of time can be obtained after being excited by a short pulsed laser. The decay profile contains useful information on the emitted photons due to the radiative recombination as a function of time. It is very difficult to record a decay profile from a single pulse excitation as a result of weak signals. Consequently, a TRPL decay profile is typically obtained by using periodic excitations which can be simply obtained using a short-pulse laser as an excitation source (a pulsed diode laser in our case), which allows to record signals over multiple cycles and thus minimize errors as a result of weak signals.

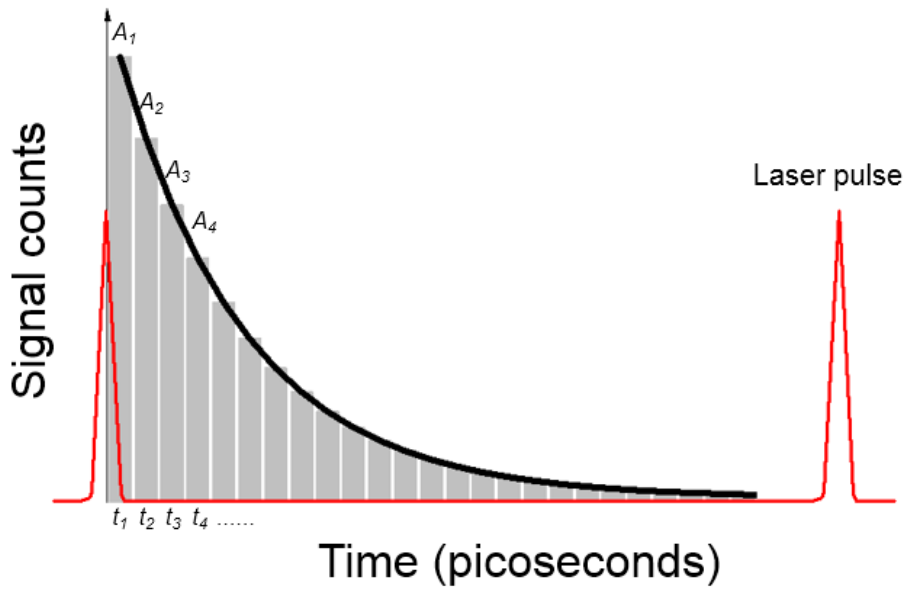


Figure 3.4: Schematic diagram of the decay profile from a luminescence material after a laser pulse.

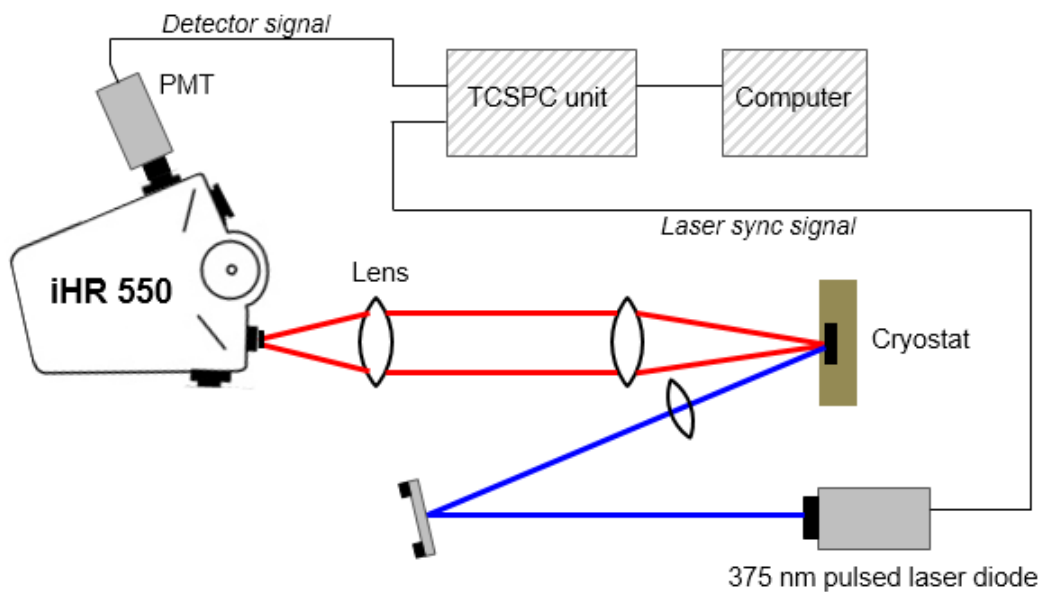


Figure 3.5: A schematic diagram of TRPL system.

Figure 3.5 is a schematic diagram of our TRPL system used in characterizing III-nitride materials and devices. A 375 nm pulsed diode laser with a pulse width of 83 picoseconds, and its power is 0.1 mW for a pulse period of 100 ns. A sample is placed in a helium closed-cycle

cryostat with a temperature range from 7 K to 300 K. Emission light is dispersed by a 550 mm monochromator before being detected by a hybrid photomultiplier detector with a timing resolution of 120 picoseconds. The hybrid photomultiplier detector is a combination of a silicon avalanche photodiode (APD) and a photomultiplier tube (PMT) with a major advantages of using a large active area and good timing resolution. A signal together with a laser synchronization signals is transferred to a time correlated single photon counting (TCSPC) system via a standard 50 Ohms coax cable. The TCSPC system records photon signals as a function of time based on multiple pulsed excitation cycles, providing average results and then a decay profile. Final measurement results are delivered to a computer.

An instrument response function (IRF), the characteristics of the timing precision of a TRPL system, is determined by the timing resolution of each individual component, which could generally be described by the following formula:<sup>2</sup>

$$e_{IRF\ system} = \sqrt{\sum e_{component}^2} \quad (3.1)$$

Our TRPL system has an IRF of around 150 picoseconds (ps) with a timing resolution of around 15 ps, which is much smaller than the typical recombination lifetime in III-nitride semiconductors.

### 3.1.4 Confocal microscopy

Figure 3.6 illustrates the principle of confocal microscopy. In a confocal microscope, an excitation source is focused into an extremely small spot by an objective lens. The emission from the focal plane of the objective lens is collected by the objective lens and then is focused onto a pinhole to reach a detector. However, for any emission which is not from the focal plane (for example, orange dash line labeled), it will be eliminated by the pinhole and cannot reach the detector. As a result, the confocal microscope can obtain a high resolution image with a low background signal. The resolution of a microscope image can be affected by a number of components, such as light source, objective lens and pinhole. Apart from a two dimensional image, a three dimensional image could also be generated as measuring a sample at different depths.

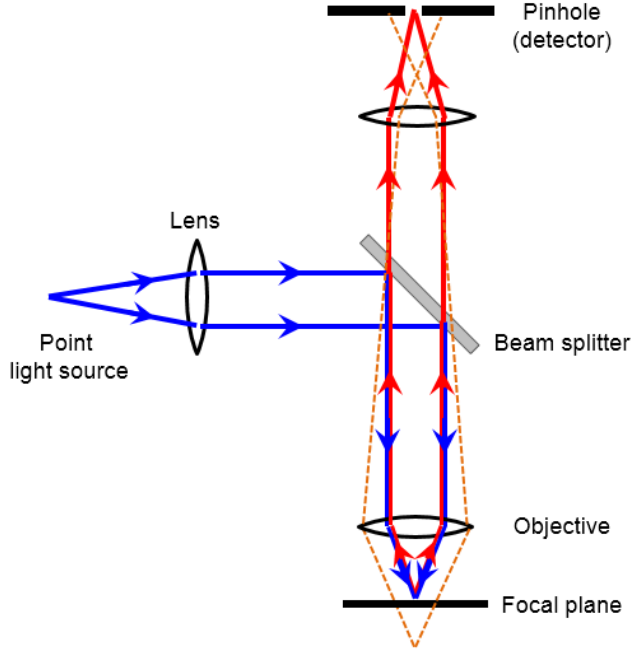


Figure 3.6: Principle of confocal microscopy.<sup>3</sup>

Our confocal microscope system uses a 375 nm continuous wave diode laser as an excitation source. The laser was focused on a sample by an objective lens with a magnification of 100 times and a numerical aperture (NA) of 0.95. Emission from a sample is collected by the same objective lens and is then focused through a pinhole. A 300 nm Princeton Instruments monochromator is employed to disperse the emission, which is finally collected by a TE cooled Andor CCD with a working temperature at -60 °C. A sample is placed in a XYZ piezoelectric stage with a minimum step of around 2 nm. According to the Rayleigh criterion, the lateral resolution  $FWHM_{lateral}$  of our confocal microscope system could be estimated by following equations:

$$FWHM_{lateral} = 0.37 * \frac{\lambda^*}{NA} \quad (3.2)$$

$$\left(\frac{1}{\lambda^*}\right)^2 = \frac{1}{2} * \left[ \left(\frac{1}{\lambda_{excitation}}\right)^2 + \left(\frac{1}{\lambda_{emission}}\right)^2 \right] \quad (3.3)$$

where  $\lambda^*$  is the mean wavelength of the microscope system, which is related to the excitation wavelength  $\lambda_{excitation}$  and the emission wavelength  $\lambda_{emission}$ . For example, in our case of a 375 nm excitation wavelength and a 460 nm emission wavelength, the lateral resolution is estimated to be around 160 nm.

## 3.2 Transmission electron microscopy characterization

### 3.2.1 Transmission electron microscopy

Transmission electron microscopy (TEM) is a powerful technique that is widely used for investigating the defects in semiconductors. For any optical microscope, the resolution is limited by the wavelength of the light used, which is on the order of hundred nanometres.<sup>4</sup> The TEM technique utilizes electrons as a “light” source, where the wavelength of electrons is much smaller than that of any visible light. Consequently, it enables us to observe a specimen with an extremely high spatial resolution on the order of 0.1 nm.<sup>5</sup> In the gun part of a TEM system, electrons generated from a filament are accelerated by an external electric field with a typical accelerating voltage from 100 to 300 kV. The beam of the electrons is then focused by electromagnetic lenses before reaching the specimen.

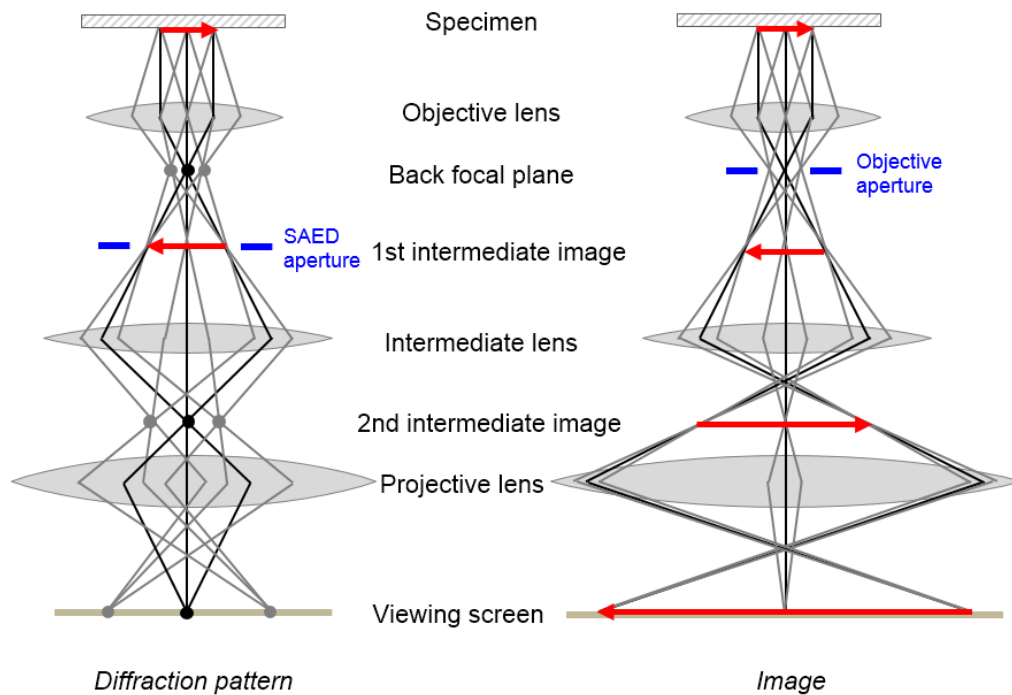


Figure 3.7: Schematic diagrams of two basic operations of diffraction mode (left) and image mode (right) in a TEM system.

When a beam of electrons pass through a thin specimen, the electrons can pass through the specimen and also suffer from scattering as a result of the interaction between the electrons and the specimen. It is worth noting that the transmitted electrons also experience an interaction process with the specimen atoms. As a result of these interactions, a diffraction

pattern will be formed. Therefore, information such as crystal structure and lattice parameters of the specimen can be extracted from the diffraction pattern.

Figure 3.7 shows a schematic diagram for a diffraction mode (left) and an image mode (right). After electrons pass through the specimen, the transmitted electrons (black lines) and the scattered electrons (grey lines) are focused by an objective lens. The diffraction pattern of the electrons is formed on the back focal plane of the objective lens, and the first intermediate image is formed on the image plane of the lens. In the diffraction mode, a selective area electron diffraction (SAED) aperture is inserted in the image plane to select a special region on the specimen which is investigated. After that, an intermediate lens treats the diffraction pattern as its object and regenerates it on its image plane, followed by a projective lens system to magnify the diffraction pattern on the viewing screen. In the image mode, an objective aperture is inserted on the back focal plane of the objective lens to determine which electrons will contribute to the image. The SAED aperture is removed at the same time. By adjusting the strength of the intermediate lens, its focus length will move from the back focal plane to the image plane of the objective lens. As a result of that, the first intermediate image will be used as the object of the intermediate lens, and the image will be presented on the viewing screen by the projective lens system.

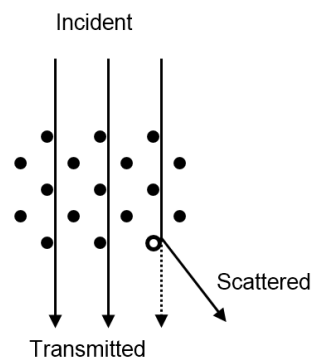


Figure 3.8: Schematic of scattered electrons by a point defect in a crystal.

In a bright field image, only a beam of transmitted electrons is selected to pass through the objective aperture to contribute to the image. In a dark field image, one or more scattered electrons beams are allowed to pass through the objective aperture, while the transmitted electrons beam is blocked. When a beam of electrons pass through a very thin crystalline specimen, most of the electrons will be transmitted electrons. If there is a point defect (for

example, open circles labeled in Figure 3.8) in a crystal, the electrons expected to be transmitted will be possibly scattered. In that case, the area will be slightly weaker than other areas when being viewed in a bright field image. In the case of a dislocation (i.e., line defects) in a crystal, electrons scattering would be significantly enhanced, leading to a dark line (or a dark point in some cases) shown in a bright field image. In summary, any defects and any strain induced distortion in a crystal will lead to the formation of brightness contrast in a TEM image.

### 3.2.2 Specimen preparation

A number of different types of TEM specimens have been prepared throughout the study for different purpose, such as the specimens for observing cross-sectional TEM images, the specimens for observing plane-view images, and the specimen for nanorod structures. A specimen with a large thin area (with a length  $>10\ \mu\text{m}$ ) is suitable for investigating the semi-polar GaN films overgrown on micro-rod templates. Methods that are used for TEM specimen preparation will be introduced in this section.

#### Cross sectional specimen

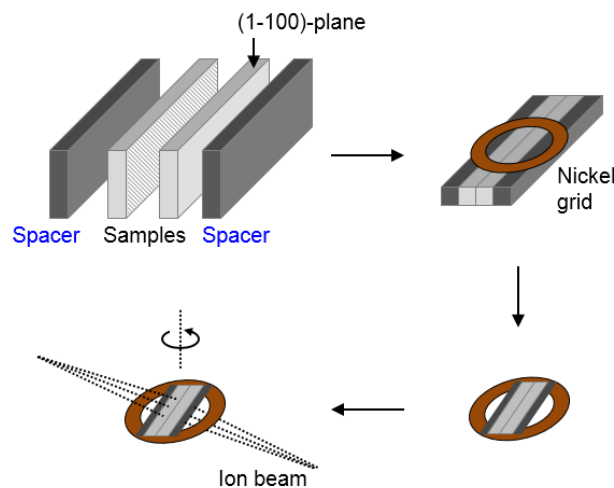


Figure 3.9: Schematic diagram of cross sectional TEM specimen preparation.

Cross-sectional TEM images are used to study the microstructure of GaN sample in terms of generation, propagation and termination of defects. Figure 3.9 shows a schematic diagram of specimen preparation for cross-sectional TEM measurements. A sample, for example, an overgrown semi-polar (11-22) GaN sample, is cut into narrow slices along the

direction which is our interest by using a low speed diamond saw. Two sample slices are glued together with face to face to make the epitaxial layer located in the middle. It is worth noting that the gap between the two sample slices should be as small as possible. An epoxy is typically used to glue the sample slices, which are subsequently subject to ion-milling by an ion beam. A silicon spacer is also glued on the back of each sample slice for protection purposes. This sandwich structure is then mounted onto a flat glass substrate by wax, followed by a mechanical polishing process, where silicon carbide sandpapers with various grit sizes from 60 to 8  $\mu\text{m}$  are used to thin and then polish the specimen. Finally, a fine polishing process is carried out on a Metaserv™ 250 polisher using a diamond paste with a grit size of down to 0.25  $\mu\text{m}$ . When the thickness of the specimen is less than 90  $\mu\text{m}$ , it becomes difficult to thin the specimen further. To circumvent this problem, a nickel grid is glued onto the specimen. With the insertion of the nickel grid, the height of the specimen can be increased by  $\sim 60$   $\mu\text{m}$ , facilitating a lapping process. When the thickness of the specimen is down to around 30  $\mu\text{m}$ , the specimen is put into a Gatan 600A dual ion mill system for an ion milling process in order to achieve electron transparency. The specimen is usually placed at a tilt angle with a low rotation speed ( $\sim 5$  rpm) during the ion mill process.

### **Plane-view specimen**

In order to observe a plane-view TEM image which is useful for investigating a defect, a nickel grid is glued directly on the back side of sample (Figure 3.10a), followed by the lapping, polishing and ion milling processes mentioned above. However, as the thickness of the specimen decreasing, two kinds of problems are likely to appear. One is due to a cracking issue, which is might related to the strain in a heteroepitaxial film grown on a large lattice-mismatched substrate, such as GaN on sapphire. The cracks can destroy the thin areas which will be observed by TEM later on as shown in Figure 3.10c. Another is due to a sample bending issue around the thin area as a result of ion milling performed only on the back side, which will make it difficult for subsequent TEM measurements. To avoid these, a square mesh grid (Figure 3.10e) is applied instead of a slot grid (Figure 3.10b). As shown in Figure 3.10f, even though there are some cracks, there is still a good thin area which can be obtained as a result of the specimen being glued onto the mesh.

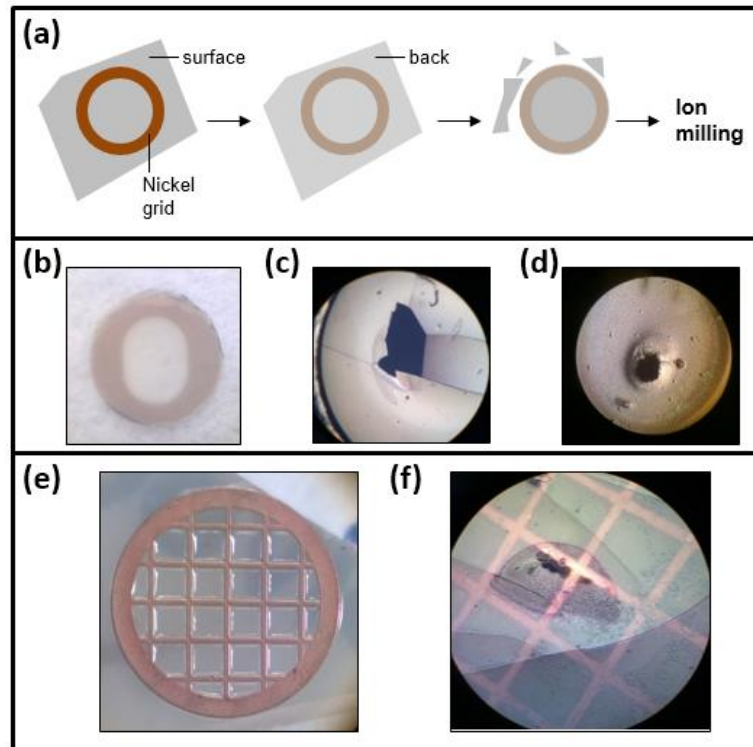


Figure 3.10: (a) Schematic diagram of plane-view TEM specimen preparation. (b) A photo of one sample glued with a slot grid. (c)(d) Photos of specimens on slot grid after ion milling. (e) A photo of one sample glued on a square mesh grid. (f) A photo of specimen on square mesh grid after ion milling.

### Nanowire specimen

Nanowire specimens are usually prepared for investigating nano-structures, such as nanorods fabricated using post-growth etching process from a planar sample and nanorods directly grown on silicon.<sup>6</sup> It is straightforward to prepare such a specimen for TEM measurements, namely, simply cutting nanorods down from a wafer using a blade and then immersing the blade into a liquid, such as isopropyl alcohol. After spinning for several minutes, a square mesh grid is then dropped in the liquid and the specimen will be ready once being dry (Figure 3.10e). Figure 3.11a shows a TEM image of an InGaN/GaN MQW nanorod that is attached to the copper mesh, where a SiO<sub>2</sub> layer should be firstly deposited to protect the nanorods. Figure 3.11b presents a TEM image of GaN nanorods grown on silicon, where a SiO<sub>2</sub> layer covering the nanorods can be observed.

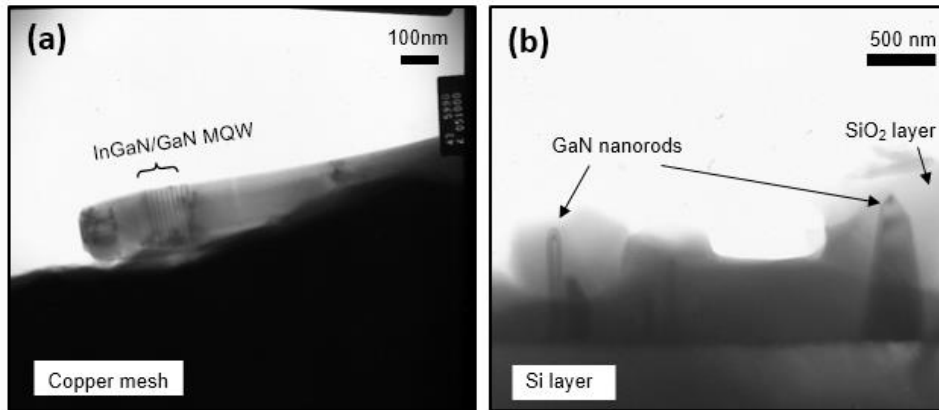


Figure 3.11 (a) TEM image of a nanorod attached to copper mesh. (b) Cross sectional TEM image of GaN nanorods grown on silicon.

### 3.3 Metal organic chemical vapour deposition

Metal organic chemical vapour deposition (MOCVD), also known as metal-organic vapour phase epitaxy (MOVPE) has been widely used in the growth of III-nitride materials. MOCVD method utilizes a chemical reaction for the deposition of a thin crystalline film onto a semiconductor substrate. For example, for GaN epitaxial growth in MOCVD, it undergoes a following chemical reaction process.



Trimethylgallium (TMG) and ammonia (NH<sub>3</sub>) are used as the Ga and N sources, respectively. Furthermore, Trimethylaluminium (TMA) and Trimethylindium (TMI) are employed as the metal sources for the others in group III. These chemical sources are vaporized and then transported into the reactor chamber by a carrier gas. Hydrogen (H<sub>2</sub>) is generally used as the carrier gas for MOCVD growth, as it can be purified very well. However, nitrogen (N<sub>2</sub>), instead of H<sub>2</sub>, is chosen as the carrier gas for InGaN growth due to an extremely low rate of indium incorporating into GaN under H<sub>2</sub> ambient. When the chemical sources enter the reactor chamber and reach the heated substrate, they can be decomposed at a high temperature (~1000-1200 °C for GaN growth). Under a suitable chamber pressure (~10-760 Torr), a layer deposition could be achieved. The growth rate and alloy composition can be accurately controlled by the gas flow rate, chamber pressure and substrate temperature.

### 3.4 Micro-rod template overgrowth approach

As mentioned above, the crystal quality of (11-22) semipolar GaN directly grown on sapphire is far away compared with current *c*-plane GaN grown on sapphire. In order to address this great challenge, our group has developed a cost-effective approach by using overgrowth on regularly arrayed micro-rod templates. With this approach, it has achieved a step-change in the crystal quality of semi-polar (11-22) GaN on sapphire, leading to the first observation of a stimulated emission optically pumped at room temperature.<sup>7</sup> Based on such overgrown semi-polar GaN samples, we have also demonstrated high-performance semi-polar (11-22) InGaN LEDs with an emission wavelength of up to the amber spectral region.<sup>8</sup>

Figure 3.12 illustrates our preparation process of a micro-rod template. Firstly, a single (11-22) GaN layer with a thickness of 1.3  $\mu\text{m}$  (reduced to 400 nm later on) is grown on 2-inch *m*-plane sapphire using our high temperature AlN buffer technique by metal organic chemical vapour deposition (MOCVD).<sup>9</sup> For the subsequent overgrowth, mask-patterned micro-rod arrays need to be fabricated on the semi-polar GaN layer. A  $\text{SiO}_2$  layer is deposited by plasma enhanced chemical vapour deposition (PECVD), followed by a standard photolithography using a mask with our specially designed pattern. After that, a nickel layer is deposited by thermal evaporation before subsequent lift-off processes to remove the photoresist used. The exposed  $\text{SiO}_2$  areas will be then removed by reactive ion etching (RIE) to achieve regularly arrayed  $\text{SiO}_2$  micro-rods. Finally, by using inductively coupled plasma (ICP) etching technique, the  $\text{SiO}_2$  micro-rods are used as a second mask to etch the GaN underneath in order to form regularly arrayed GaN micro-rods with the  $\text{SiO}_2$  remaining on their top. Both the diameter and spacing of the micro-rods can be accurately controlled, which in turn depend on the micro-rod mask used.

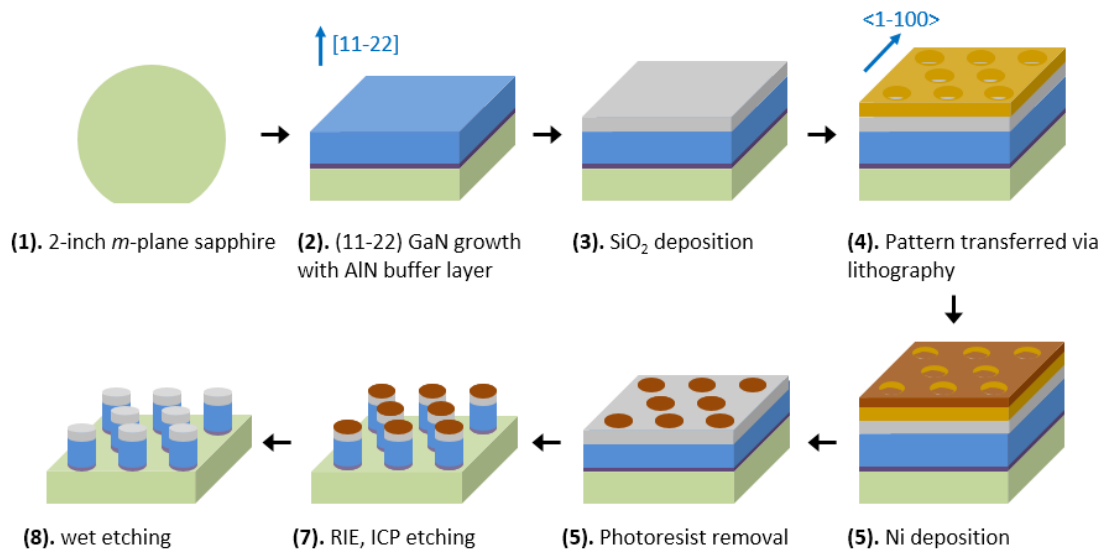


Figure 3.12: Schematic diagram of the micro-rod template fabrication process.

Chemical treatments are also carried out to heal the possible damage on micro-rod sidewalls during the dry etching processes prior to any further overgrowth process by MOCVD. The subsequent overgrowth process is carried out with a typical growth temperature, V/III ratio and pressure at 1120 °C, 1600 and 75 Torr, respectively. A flat surface could be obtained with the thickness of overgrown layer around 4 μm, which is faster than any conventional epitaxial lateral overgrowth (ELOG) techniques.<sup>10,11</sup>

## References

- 1 Data sheet for EQ-99X Laser-driven light sources. <http://www.energetiq.com/DataSheets/EQ99X-Data-Sheet.pdf>
- 2 P. Kapusta, M. Wahl, and R. Erdmann, *Advanced Photon Counting: Applications, Methods, Instrumentation* (Springer 2015)
- 3 <http://www.witec.de/resources-and-education/knowledge-base/show/the-microscope/what-is-confocal-microscopy>
- 4 E. G. Van Putten, D. Akbulut, J. Bertolotti, W. L. Vos, A. Lagendijk, and A. P. Mosk, *Phys. Rev. Lett.* **106**, 193905 (2011).
- 5 S. J. Pennycook, M. Varela, C. J. D. Hetherington, and A. I. Kirkland, *MRS Bull.* **31**, 36 (2006).
- 6 Y. Hou, J. Bai, R. Smith, and T. Wang, *Nanotechnology* **27**, 205205 (2016).
- 7 B. Xu, L. Jiu, Y. Gong, Y. Zhang, L. C. Wang, J. Bai, and T. Wang, *AIP Adv.* **7**, 045009 (2017)
- 8 J. Bai, B. Xu, F. G. Guzman, K. Xing, Y. Gong, Y. Hou, and T. Wang, *Appl. Phys. Lett.* **107**, 261103 (2015).
- 9 T. Wang, K. B. Lee, J. Bai, P. J. Parbrook, R. J. Airey, Q. Wang, G. Hill, F. Ranalli, and A. G. Cullis, *Appl. Phys. Lett.* **89**, 081126 (2006).
- 10 P. De Mierry, N. Kriouche, M. Nemoz, and G. Nataf, *Appl. Phys. Lett.* **94**, 191903 (2009).
- 11 N. Kriouche, P. Vennéguès, M. Nemoz, G. Nataf, and P. De Mierry, *J. Cryst. Growth* **312**, 2625 (2010).

# Chapter 4

## Defect reduction in overgrown semi-polar (11-22) GaN on a regularly arrayed micro-rod array template

---

In this chapter, we demonstrate a great improvement in the crystal quality of our semi-polar (11-22) GaN overgrown on regularly arrayed micro-rod templates fabricated using a combination of industry-matched photolithography and dry-etching techniques. As a result of our specially designed micro-rod configuration, an intrinsic issue on the anisotropic growth rate which is a great challenge in conventional overgrowth technique for semi-polar GaN has been resolved. Transmission electron microscopy measurements show a different mechanism of defect reduction from conventional overgrowth techniques and also demonstrate major advantages of our approach. The dislocations existing in the GaN micro-rods are effectively blocked by both a SiO<sub>2</sub> mask on the top of each GaN micro-rod and lateral growth along the *c*-direction, where the growth rate along the *c*-direction is faster than that along any other direction. Basal stacking faults (BSFs) are also effectively impeded, leading to a distribution of BSF-free regions periodically spaced by BSF regions along the [-1-123] direction, in which high and low BSF density areas further show a periodic distribution along the [1-100] direction. Furthermore, a defect reduction model is proposed for further improvement in the crystalline quality of overgrown (11-22) GaN on sapphire.

### 4.1 Introduction

Currently, the major challenge is due to the crystalline quality of semi-polar GaN, which is far from satisfactory. So far, semi-polar GaN with device performance is exclusively grown on free-standing semi-polar GaN substrates, which are obtained by slicing very thick *c*-plane GaN along semi-polar orientations. This limits the substrate size to a square of 10x10 mm<sup>2</sup>, and thus is extremely expensive.<sup>1-3</sup> Therefore, it would be impractical for industry.

There is a limited number of reports on overgrowth of semi-polar GaN mainly based on conventional epitaxial lateral overgrowth (ELOG),<sup>4,9</sup> which generally leads to a non-uniformity issue and requires a thick overgrown layer (typically  $> 10 \mu\text{m}$ ) in order to achieve an atomically flat surface. In order to address these issues, previously we reported an overgrowth approach based on self-organised nickel nano-masks, leading to a significant improvement in the crystal quality of either semi- or non-polar GaN on sapphire and achieving an atomically flat surface with an overgrown layer of only a few micrometres.<sup>10,11</sup> Very recently, we have developed another cost-effective approach to the overgrowth of semi-polar GaN on mask-patterned micro-rod arrays on 2-inch sapphire, where the diameter of micro-rods with a regular patterning can be accurately controlled. On such high quality semi-polar GaN templates, we have achieved high performance semi-polar light emitting diodes (LEDs) with a wide spectral range of up to amber.<sup>12,13</sup>

In this chapter, we investigate in detail a mechanism of defect reduction in the overgrown semi-polar (11-22) GaN on the regular micro-rod array templates by transmission electron microscopy (TEM) measurements, and a detailed model has been established, essentially allowing us to further improve the crystalline quality of overgrowth semi-polar GaN on sapphire.

## 4.2 Overgrowth process

A single (11-22) GaN layer with a thickness of  $1.3 \mu\text{m}$  is grown on *m-plane* sapphire using our high temperature AlN buffer by metal organic chemical vapour deposition (MOCVD).<sup>14</sup> For subsequent overgrowth, mask-patterned micro-rod arrays have been fabricated on the semi-polar GaN layer. Firstly, a  $500 \text{ nm}$   $\text{SiO}_2$  layer is deposited by plasma enhanced chemical vapour deposition (PECVD), followed by a standard photolithography patterning process and subsequent dry etching processes using Inductively Reactive Plasma (ICP) and Reactive Ion Etching (RIE) techniques. Regularly arrayed  $\text{SiO}_2$  micro-rods can be achieved. Finally, the  $\text{SiO}_2$  micro-rods served as a second mask are used to etch the GaN underneath in order to form regularly arrayed GaN micro-rods with the  $\text{SiO}_2$  remaining on their top. The micro-rod masks with different diameters from  $1.5$  to  $3 \mu\text{m}$  have been employed for the fabrication of micro-rod array templates. As an example, Figure 4.1a shows a top-view scanning electron microscope (SEM) image of a micro-rod array template with a diameter of  $3.5 \mu\text{m}$  and a spacing (edge to edge along  $[1-100]$  direction or  $[-1-123]$  direction) of  $2 \mu\text{m}$ . The

subsequent overgrowth process is carried out by MOCVD with a growth temperature, V/III ratio and pressure at 1120 °C, 1600 and 75 Torr, respectively. Please note that the approach is fundamentally different from our previous method based on self-organised nickel nanomasks,<sup>11</sup> where the rod diameter, the shape, the spacing between rods and the orientation of the rod arrays are all randomly distributed. Due to the anisotropic growth rate of semi-polar GaN, it would be necessary to maximize the spacing along one particular direction (for example, the projection of *c*-direction to the surface), and minimize the spacing along another direction (for example, *m*-direction). These can be achieved only by the present approach. Furthermore, due to an accurate control in the orientation of micro-rod arrays using the present approach, it is expected that the defect reduction mechanism is different from that for the previous self-organized nickel nano-mask approach.

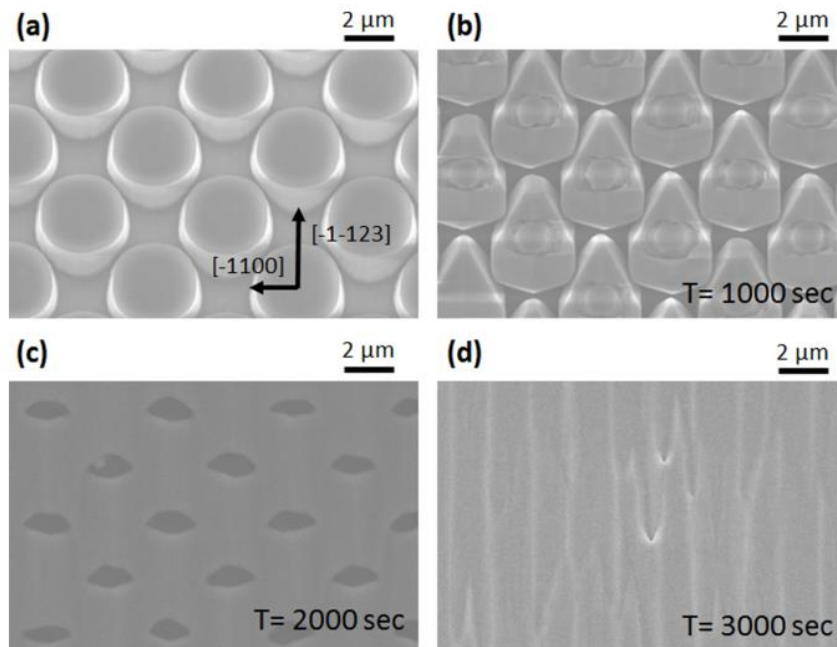


Figure 4.1: (a) Top-view SEM image of micro-rod arrays with a diameter of 3.5  $\mu\text{m}$  and spacing (edge to edge) of 2  $\mu\text{m}$ ; (b)-(d) SEM images of the surface morphology of our (11-22) GaN with overgrowth time of 1000, 2000 and 3000 seconds, respectively.

Figure 4.1 (b)-(d) show an evolution of the surface morphology of the overgrown layer on an initial growth stage, demonstrating a change in surface morphology when the growth time is 1000, 2000 and 3000 seconds, respectively. The overgrowth initiates from the exposed

sidewalls of micro-rods as shown in Figure 4.1b, and the lateral growth is dominated by the growth along the [0001] direction labeled as *c*-direction and the [11-20] direction labeled as *a*-direction. Comparing the lengths of the two growing wings, the *c*-direction growth is faster than the *a*-direction growth. Moreover, the growth along the [-1100] direction labeled as *m*-direction is negligible. After the coalescence of the *c*-direction growth and the *a*-direction growth facets, the GaN growth tends to move upward. When the thickness of the overgrown layer exceeds the height of the micro-rods, the growth begins to extend to cover the SiO<sub>2</sub> masks. Although the *m*-direction growth is slower than the growth along other directions, the specially designed pattern of the micro-rods as shown in Figure 4.1a compensates the anisotropic growth rate, also facilitating another second coalescence occurring over the SiO<sub>2</sub> masks. Eventually a full coalescence is achieved. A smooth surface can be achieved with the overgrowth of about 4 μm, which is faster than any other conventional ELOG techniques.<sup>15,16</sup> Initial X-ray diffraction (XRD) measurements have been performed as a function of azimuth angle, exhibiting that the full width at half maximum (FWHM) of on-axis XRD rocking curves measured along the [1-100] and [-1-123] directions is 320 and 260 arcsec, respectively. These represent the best results on semi-polar GaN with a similar thickness grown on sapphire.

### 4.3 Defect reduction mechanism

#### 4.3.1 Dislocation reduction during the overgrowth

The specimens for both cross-sectional and plane-view transmission electron microscopy (TEM) measurements are prepared by initial mechanical lapping/polishing and then ion milling down to electron transparency. TEM measurements have been performed using a Philips EM430 TEM operating at 200 kV. Based on an invisibility criterion,<sup>16-20</sup> dislocations are out of contrast when the product of a diffraction vector  $\mathbf{g}$  and a dislocation displacement vector  $\mathbf{R}$  equals zero, namely,  $\mathbf{g} \cdot \mathbf{R} = 0$  (It would still be possible to observe a weak contrast of dislocations for a very thin specimen in the case of the dislocation unparallelled to its burger vector. This does not apply in our case.); and stacking faults are invisible when the product is an integer, including zero.

Figure 4.2a shows a typical bright-field cross-sectional TEM image taken along [1-100] zone-axis with  $\mathbf{g} = 0002$ , indicating *c*-type threading dislocations (TDs), *a+c* TDs and Shockley partial dislocations; while Figure 4.2b shows a typical bright-field cross-sectional TEM image taken along [1-100] zone-axis but with  $\mathbf{g} = 11-20$ , demonstrating *a*-type TDs, *a+c* TDs and

Frank partial dislocations. Figure 4.2a and 4.2b show all kinds of the dislocations, demonstrating that the dislocations (with an inclination angle of  $58.4^\circ$  to surface) from the GaN micro-rods under the  $\text{SiO}_2$  masks have been greatly reduced as a result of the overgrowth on our micro-rod arrays.

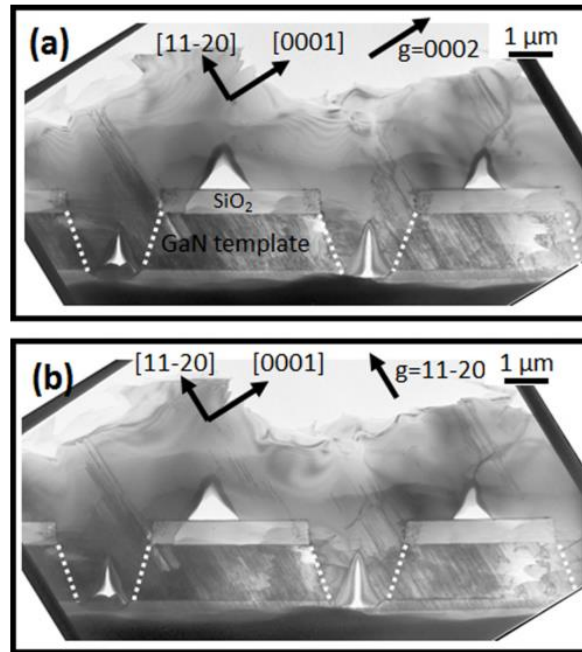


Figure 4.2: Bright field cross-sectional TEM images of our overgrown GaN layer taken along the  $[1-100]$  zone-axis under a diffraction vector of (a)  $g = 0002$  and (b)  $g = 11-20$ .

The voids in a triangular shape observed in the trenches between the micro-rods are formed as a result of the first coalescence of the  $c$ -direction growth facets and the  $a$ -direction growth facets from two neighbouring micro-rods. The voids extend from the sapphire substrate, confirming that the growth initiates from the exposed sidewalls rather than the bottom of the trenches between micro-rods. It is important because the GaN growth from the bottom needs to be suppressed in order to prevent the defects penetrating from the micro-rods to the overlying structures.

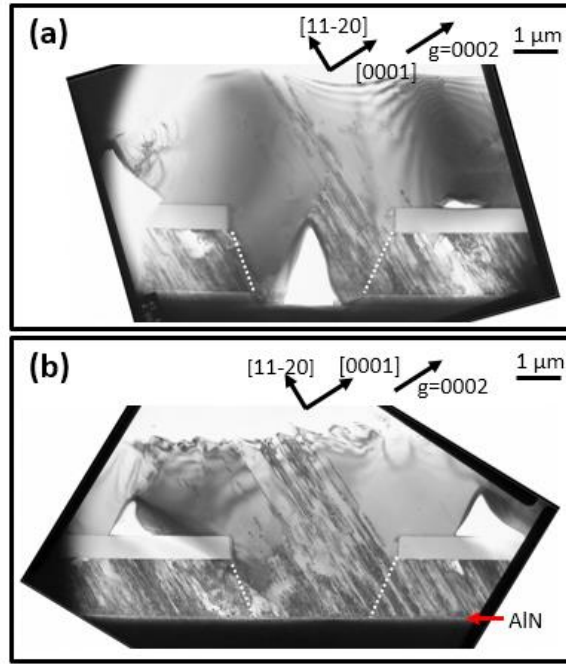


Figure 4.3: Bright field cross-sectional TEM images of two semi-polar (11-22) GaN films overgrown on templates (a) with and (b) without etching through the AlN buffer layer under a diffraction vector of  $g = 0002$ .

Figure 4.3 presents two bright field cross-sectional TEM images of two semi-polar (11-22) GaN films overgrown on templates with and without etching through the AlN buffer layer. In Figure 4.3b, the absence of the void between two micro-rods indicates that GaN initiates from the AlN buffer layer. In this overgrown GaN, a number of dislocations have been formed around the AlN/GaN interface and most of them propagate to the sample surface. In contrast, the other sample in Figure 4.3a exhibits few dislocations in the overgrown GaN layer, owing to the suppression of GaN growth from the buffer layer.

Similar to the other overgrowth techniques, in Figure 4.2, the GaN grown laterally along the  $c$ -direction exhibits approximately free of dislocations, whereas the GaN grown along the  $a$ -direction contains a number of defects.<sup>8,18</sup> Due to the fact that the  $c$ -direction growth rate is faster than the  $a$ -direction growth rate, the  $a$ -direction growth is eventually stopped by the  $c$ -direction growth, terminating the propagation of defects from the  $a$ -direction growth. Therefore, the growth conditions favouring the  $c$ -facet growth are preferred on the early overgrowth stage, leading to an efficient reduction in dislocations and extended defects. As a result, the majority of the pre-existing dislocations in the GaN micro-rods are effectively prevented from

penetrating by both the SiO<sub>2</sub> masks and the *c*-direction growth. Only a small part of the dislocations along the *a*-direction propagate to the surface. Furthermore, another kind of void has also been observed over the SiO<sub>2</sub> mask on the top of each micro-rod as a consequence of the second coalescence along the [-12-10] and [2-1-10] directions as well. It is worth noting that a very small number of extra dislocations are generated due to the 2nd coalescence, as presented in Figure 4.2.

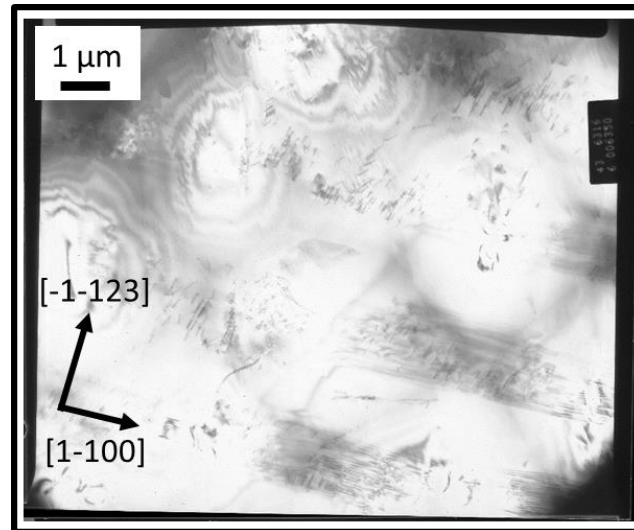


Figure 4.4: Bright field plane-view TEM image of our overgrown (11-22) GaN layer with a diffraction vector  $g=1-212$ .

Dislocations distribution across the (11-22) GaN layer surface is revealed by a bright field plane-view TEM image with a diffraction vector  $g=1-212$ , as shown in Figure 4.4. Our plane-view TEM image indicates that the overall dislocation density in our overgrown semi-polar (11-22) GaN is about  $4.2 \times 10^8 \text{ cm}^{-2}$ , demonstrating a significant reduction in dislocation density from the order of  $10^{10} \text{ cm}^{-2}$  in the as-grown GaN which is used to fabricate into the micro-rod array template.

#### 4.3.2 BSF reduction during the overgrowth

Basal stacking faults (BSFs), as extended defects, can be observed along either the [-12-10] or the [2-1-10] zone-axis by tilting 30° from the [1-100] zone-axis.<sup>19</sup> Figure 4.5a shows a typical bright-field cross-sectional TEM image taken along the [2-1-10] direction with  $g=1-100$ , where BSFs appear as straight dark lines with an inclination angle of 58.4° to the surface. Since the BSFs exist in basal planes, they are impeded by the *c*-direction growth. As denoted

by the red arrows in Figure 4.5a, part of the BSFs along the  $a$ -direction are blocked by the adjacent  $c$ -direction growth (leading to defect-free regions), which are terminated very likely in the form of PDs and prismatic stacking faults (PSFs), while the rest of the BSFs along the  $a$ -direction are found to survive from the first coalescence process and propagate to the surface. This forms the free-BSF regions and the BSF regions distributing in a periodic form along the  $[-1-123]$  direction. What also interests us is the appearance of the BSF clusters over the  $\text{SiO}_2$  masks, as marked by the blue arrows in Figure 4.5a.

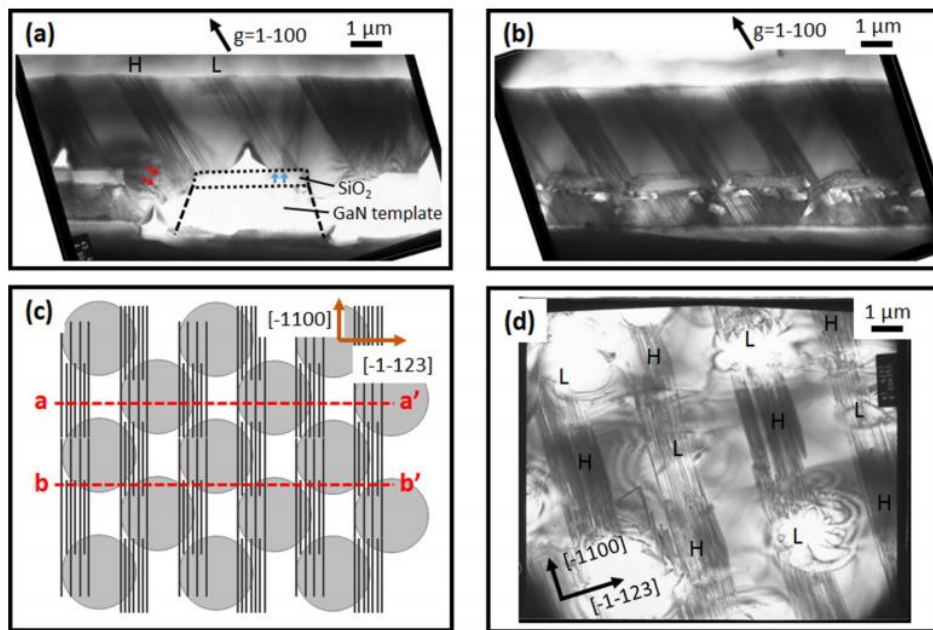


Figure 4.5: (a) and (b) Bright-field cross-sectional TEM images of our (11-22) overgrown GaN layer viewed along the  $[11-20]$  zone-axis with diffraction vector  $g=1-100$ , but with preparing specimens cleaved differently; (c) Schematic diagrams of the BSF distribution on the sample surface and our micro-rod patterning. The dash lines labeled as  $a-a'$  and  $b-b'$  depict the different cleavage directions for preparing the specimens from a same sample used for TEM observation as shown (a) and (b), respectively; (d) Plane-view TEM image of our (11-22) overgrown GaN with a diffraction vector  $g=1-100$ .

To study the origin of these unexpected BSFs, a TEM specimen was particularly prepared by cleaving along a direction schematically illustrated by a dash line labeled as  $b-b'$  as shown in Figure 4.5c. Figure 4.5c also schematically shows a distribution of BSFs indicated

by the vertical dark lines, which will be explained later. In this case, all the micro-rods belonging to the two neighbouring rows can be observed in a cross-sectional TEM image as shown in Figure 4.5b, while the upper and lower voids cannot be observed. By comparing Figure 4.5a and 4.5b, it can be concluded that the BSF clusters observed on the left side of the SiO<sub>2</sub> masks on each micro-rod in Figure 4.5a are from a different micro-rod on a neighbouring row. One solid evidence is that the spacing between these BSF clusters is around 1.5 μm, similar to the distance in Figure 4.5a with the cleavage along micro-rod centre to centre, namely, along a dash line marked as a-a' in Figure 4.5c. This is also confirmed by the plane-view TEM image in Figure 4.5d.

Figure 4.5d clearly demonstrates that BSF clusters with orientation along the *m*-direction, i.e., [-1100], are separated by defect-free regions along the [-1-123] direction. The width of the defect-free areas is around 1.5 μm, consistent with the cross-sectional TEM images as shown in Figure 4.5a. In addition, the distribution of these BSF clusters shows a repeat of high BSF density areas (labeled with H) and low BSF density areas (labeled with L). It means the BSFs can expand within the basal plane, propagating with a component parallel to the *m*-direction during the overgrowth above the SiO<sub>2</sub> masks. During the second coalescence process, some BSFs are terminated by a formation of either PDs or PSFs, leading to a further reduction in BSF density.<sup>20</sup> Consequently, this forms one area with a low BSF density (i.e., L region) and another area with a high BSF density (i.e., H region), appearing in a periodic form along the *m*-direction.

It is worth noting that the locations of the defect-free regions and defect regions depend on layer thickness as schematically shown in Figure 4.5c, as the defects penetrate along the *a*-direction which is 58° with respect to the surface. Our plane-view TEM image shows that the average BSF density of our overgrown GaN on a 3.5 μm micro-rod template has been reduced to  $4.7 \times 10^4 \text{ cm}^{-1}$ .

## 4.4 Defect reduction model

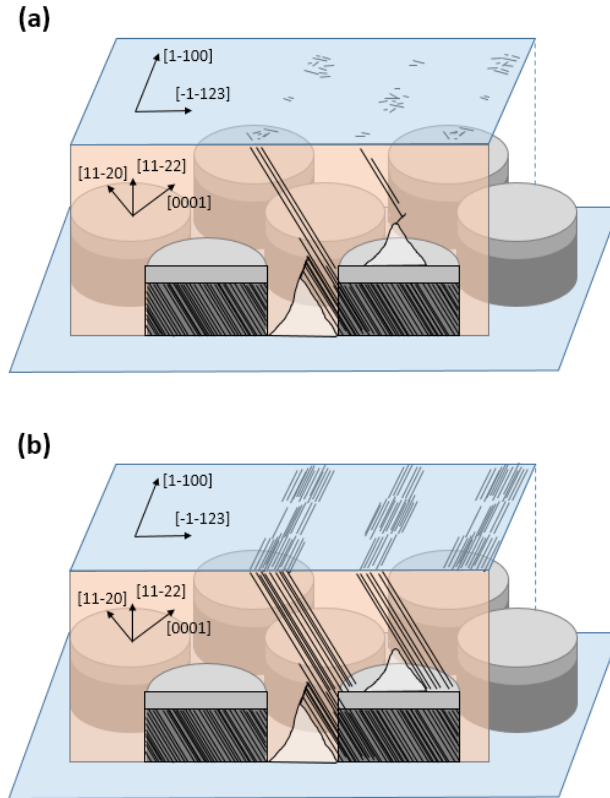


Figure 4.6: Schematic diagrams of (a) dislocation reduction and (b) BSF reduction in semi-polar (11-22) GaN overgrown on regularly arrayed micro-rods.

Based on the above TEM study, two schematic diagrams could be used to illustrate the dislocation reduction and BSF reduction in semi-polar (11-22) GaN layer overgrown on regularly arrayed micro-rod templates, as shown in Figure 4.6. Most of the dislocations existing in the micro-rods are either blocked by the SiO<sub>2</sub> layer on top or covered by the *c*-growth during the first coalescence. After that, only a small part of dislocations can penetrate to the sample surface. This leads to a significant reduction in dislocation density in the overgrown (11-22) GaN films. Furthermore, additional dislocations could be generated during the second coalescence above the micro-rods. BSFs show a property of expanding within the basal plane, with a component of propagation direction along the *m*-direction. As a consequence, BSF stripes could be formed with an orientation along the *m*-direction. The BSF stripes are separated by defect free areas and each stripe contains a periodic distribution of high and low BSF density regions.

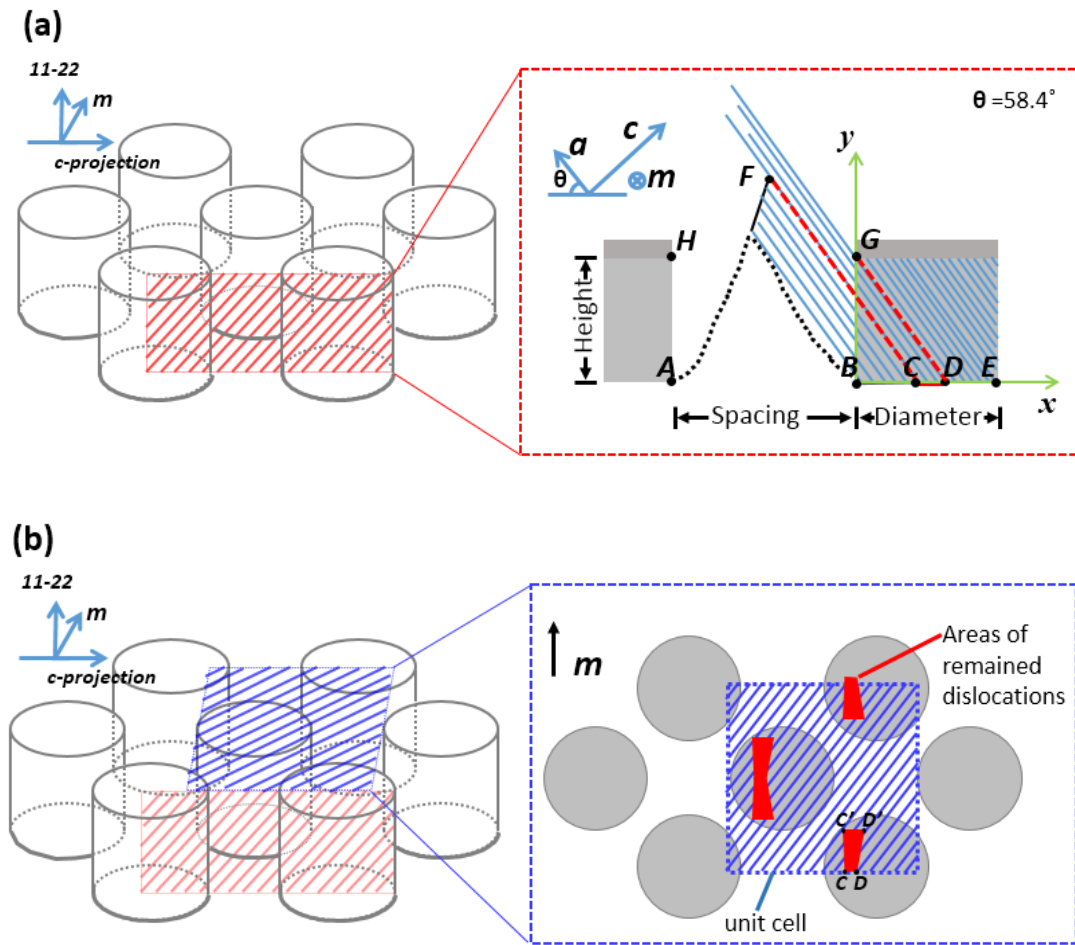


Figure 4.7: (a) Cross-sectional and (b) top-view diagrams of a dislocation reduction model for semi-polar (11-22) GaN overgrown on regularly arrayed micro-rods. The cross-sectional diagram is viewed along the [1-100] direction.

In order to further optimize the design of our micro-rod mask patterning, a model has been built up to understand the influence of the micro-patterning on defect reduction. Figure 4.7a schematically illustrates a cross-sectional diagram of micro-rods along the  $m$ -direction. Segment  $AE$  represents one period of micro-rod and the spacing between two adjacent micro-rods. Point  $F$  is top of first coalesce boundary, which is related to the top (point  $H$ ) of the sidewall (line segment  $AH$ ) where  $c$ -direction growth allowed, and the growth ratio between the  $c$ - and the  $a$ - directions. Point  $C$  and  $D$  are the projections of point  $F$  and point  $G$  on  $x$ -axis, respectively. On the basis of the aforementioned defect reduction mechanism, only the dislocation located in the line segment  $CD$  (marked by red line) have a chance to propagate to the surface, while other dislocations are blocked either during the first coalescence (line

segment **BC**) or by the SiO<sub>2</sub> masks (line segment **DE**). The length of segment **CD** is determined by the following equation:

$$L_{CD} = \frac{1 - \frac{v_c}{v_a} * \frac{1}{\tan\theta}}{1 + \frac{v_c}{v_a} * \tan\theta} * S \quad (4.1)$$

where  $v_c$  and  $v_a$  are GaN growth rates along the  $c$ - and the  $a$ - directions, respectively;  $\theta$  is the angle between the growth surface and basal plane ( $\theta = 58.4^\circ$  in (11-22) orientation); and  $S$  is the spacing between two adjacent micro-rods. According to equation 4.1, a high ratio of growth rate  $v_c/v_a$  is useful for reducing the length of segment **CD**, which could be achieved by either favouring the  $c$ -direction growth or suppressing the  $a$ -direction growth. Meanwhile, it is found that the length of segment **CD** increases with increasing the spacing between micro-rods. When

the spacing  $S$  is very large,  $> \frac{1 + \frac{v_c}{v_a} * \tan\theta}{\tan\theta - \frac{v_c}{v_a}} * h$ , the length of segment **CD** will be determined by

$L_{CD} = \frac{h}{\tan\theta}$ . Here,  $h$  is the height of micro-rods. In that case, the first coalescence process during the overgrowth shows few effects on blocking dislocations. All the dislocations initiating from the sidewall **BG** have a chance to propagate to the sample surface. Furthermore, as the length of segment **CD** decreases with decreasing the spacing  $S$ , it is suggested that micro-rods with a small gap could be used for reducing the dislocation density. However, a pattern with a small gap will make it very difficult for the dry etching processes in practice. Thus, micro-rods with a gap slightly smaller than the diameter have been chosen as compromised by the micro-rod fabrication process. One may notice that the spacing between micro-rods increases when the intersection plane moves from micro-rod centre to edge due to the circle shape. This leads to a slight increase in the length of line segment **C'D'**, as shown in Figure 4.7b. Fortunately, the large spacing between two micro-rod edges is interrupted with the appearance of another micro-rod from the neighbouring row as a result of the small gap between micro-rods.

By integrating the line segment **CD** along the  $m$ -direction, an area where dislocations have a chance to propagate to the surface is obtained, as illustrated by Figure 4.7b. In a unit cell, the ratio of this area to the area of integrated line segment **AE** along the  $m$ -direction can be treated as a dislocation remaining ratio  $\eta$ .

$$\eta = \frac{\int L_{CD}}{\int L_{AE}} \quad (4.2)$$

For simplicity, any decrease in dislocation density due to the lateral overgrowth along the  $a$ -direction and a very small number of extra dislocations generated during the coalescence processes<sup>11,25</sup> are not taken into account.

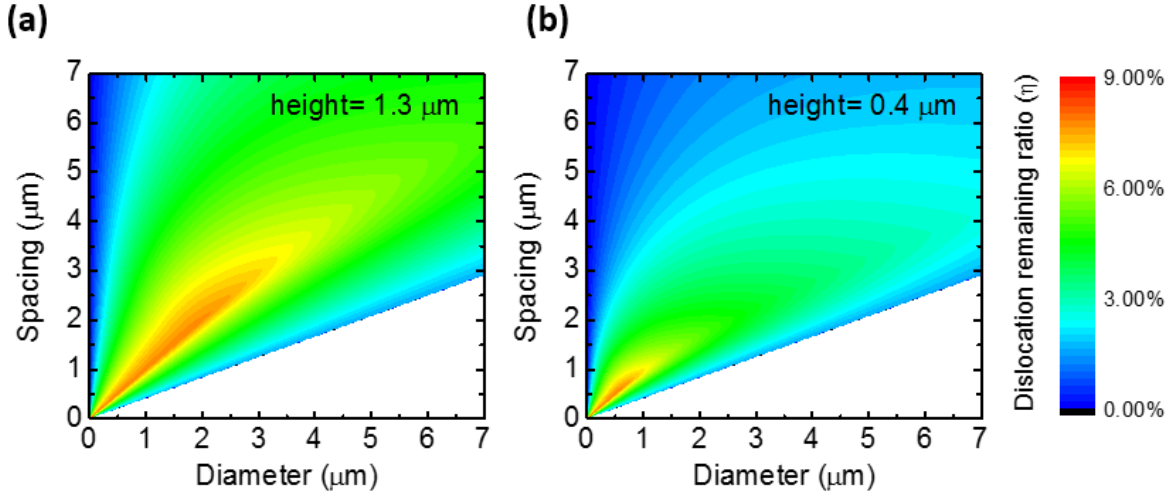


Figure 4.8: Contour plots of the dislocation remaining ratio as a function of micro-rod diameter and micro-rod spacing with a micro-rod height of (a) 1.3 and (b) 0.4  $\mu\text{m}$ , respectively.

Figure 4.8 shows our simulation result, describing the relationship between the dislocation remaining ratio and micro-rod diameter & spacing between micro-rods, where the height of micro-rods is set as 0.4 and 1.3  $\mu\text{m}$  as two examples, respectively. The simulation in both cases is limited to a diameter of micro-rods of below 7  $\mu\text{m}$ , taking into account the difficulty in achieving an atomically flat surface if overgrown on micro-rods with a larger diameter. In Figure 4.8, the blue area represents a low dislocation remaining ratio while the red area represents a high ratio. There are two low ratio areas: one is the upper-left corner with a very small micro-rod diameter of below 0.5  $\mu\text{m}$ , and the other one is in the lower-right with a micro-rod diameter of a few micrometres and a micro-rod spacing from 1.5 to 2.5  $\mu\text{m}$ . From the former one, it seems that micro-rods with a small diameter and a large spacing would be useful for reducing the dislocations. However, one can imagine a 2-inch template with only one micro-rod located in its centre. According to the model, the dislocation density in the overgrown layer would be extremely low. Unfortunately, overgrown on such a template is

impossible even if we have fabricated the template. Furthermore, a conventional photolithography typically uses an ultraviolet lighting source with a wavelength of  $\sim 300$  nm, and thus it would be difficult to fabricate rod arrays with a sub-micron diameter. Consequently, it is worth paying attention to the lower-right blue area, where both micro-rod diameter and micro-rod spacing are on a few micrometer scale.

By carefully examining Figure 4.8, the range for the blue area increases when the micro-rod height reduces from 1.3 to 0.4  $\mu\text{m}$ , enhancing the chance for tuning either micro-rod diameter or micro-rod spacing for effectively blocking defect penetration. On the other hand, this also demonstrates that a decrease in the height of micro-rods potentially leads to a further reduction in dislocation density. It has been confirmed by our very recent experiments which show better crystal quality in the semi-polar GaN overgrown on the micro-rods with a height of 0.4  $\mu\text{m}$  compared to the micro-rods with a height of 1.3  $\mu\text{m}$ . A reduction in micro-rod height leads to a decrease in the exposed areas of the sidewalls of the micro-rods for the growth along the  $a$ -direction which is beneficial for the defect reduction.

## 4.5 Summary

In conclusion, the defect reduction in the overgrown semi-polar (11-22) GaN on regularly arrayed micro-rod arrays has been studied by TEM measurements. It has been found that the majority of the dislocations and BSFs are blocked by the  $\text{SiO}_2$  masks and the coalescence processes during the overgrowth. Owing to the faster growth rate along the  $c$ -direction than along the  $a$ -direction, the defects from the growth along the  $a$ -direction are effectively blocked by the growth along the  $c$ -direction (the  $c$ -direction growth leads to free-defect). In addition, the BSFs have been found to expand within the basal planes, propagating with a component parallel to the  $m$ -direction. After the second coalescence over the  $\text{SiO}_2$  masks, the BSFs distribute in a periodic form consisting of defect-free regions and defect regions along the  $[-1-123]$  direction, where the defect regions compose of low density BSF clusters and high density BSF clusters in a periodic form along the  $m$ -direction.

## References

- 1 P. Fini, L. Zhao, B. Moran, M. Hansen, H. Marchand, J. P. Ibbetson, S. P. DenBaars, U. K. Mishra, and J. S. Speck, *Appl. Phys. Lett.* **75**, 1706 (1999).
- 2 K. Hiramatsu, K. Nishiyama, M. Onishi, H. Mizutani, M. Narukawa, A. Motogaito, H. Miyake, Y. Iyechika, and T. Maeda, *J. Cryst. Growth* **221**, 316 (2000).
- 3 H. Masui, S. Nakamura, S. P. DenBaars, and U. K. Mishra, *IEEE Trans. Electron Devices* **57**, 88 (2010).
- 4 Y. Yoshizumi, M. Adachi, Y. Enya, T. Kyono, S. Tokuyama, T. Sumitomo, K. Akita, T. Ikegami, M. Ueno, K. Katayama, and T. Nakamura, *Appl. Phys. Express* **2**, 92101 (2009).
- 5 H. Zhong, A. Tyagi, N. N. Fellows, R. B. Chung, M. Saito, K. Fujito, J. S. Speck, S. P. DenBaars, and S. Nakamura, *Electron. Lett.* **43**, 825 (2007).
- 6 I. Kidoguchi, A. Ishibashi, G. Sugahara, and Y. Ban, *Appl. Phys. Lett.* **76**, 3768 (2000).
- 7 B. M. Imer, F. Wu, S. P. DenBaars, and J. S. Speck, *Appl. Phys. Lett.* **88**, 61908 (2006).
- 8 X. Ni, U. Özgür, A. A. Baski, H. Morkoç, L. Zhou, D. J. Smith, and C. A. Tran, *Appl. Phys. Lett.* **90**, 182109 (2007).
- 9 D. Iida, M. Iwaya, S. Kamiyama, H. Amano, and I. Akasaki, *J. Cryst. Growth* **311**, 2887 (2009).
- 10 K. Xing, Y. Gong, J. Bai, and T. Wang, *Appl. Phys. Lett.* **99**, 181907 (2011).
- 11 J. Bai, Y. Gong, K. Xing, X. Yu, and T. Wang, *Appl. Phys. Lett.* **102**, 101906 (2013).
- 12 Y. Gong, K. Xing, B. Xu, X. Yu, Z. Li, J. Bai, and T. Wang, *ECS Trans.* **66**, 151 (2015).
- 13 J. Bai, B. Xu, F. G. Guzman, K. Xing, Y. Gong, Y. Hou, and T. Wang, *Appl. Phys. Lett.* **107**, 261103 (2015).
- 14 T. Wang, K. B. Lee, J. Bai, P. J. Parbrook, R. J. Airey, Q. Wang, G. Hill, F. Ranalli, and A. G. Cullis, *Appl. Phys. Lett.* **89**, 81126 (2006).
- 15 P. De Mierry, N. Kriouche, M. Nemoz, and G. Nataf, *Appl. Phys. Lett.* **94**, 191903 (2009).
- 16 N. Kriouche, P. Vennéguès, M. Nemoz, G. Nataf, and P. De Mierry, *J. Cryst. Growth* **312**, 2625 (2010).
- 17 T. Hino, S. Tomiya, T. Miyajima, K. Yanashima, S. Hashimoto, and M. Ikeda, *Appl. Phys. Lett.* **76**, 3421 (2000).

- 18 P. Vennéguès, *Semicond. Sci. Technol.* **27**, 24004 (2012).
- 19 F. Wu, Y. D. Lin, A. Chakraborty, H. Ohta, S. P. DenBaars, S. Nakamura, and J. S. Speck, *Appl. Phys. Lett.* **96**, 231912 (2010).
- 20 C. F. Johnston, M. J. Kappers, and C. J. Humphreys, *J. Appl. Phys.* **105**, 73102 (2009).
- 21 X. Ni, U. Özgür, Y. Fu, N. Biyikli, J. Xie, A. A. Baski, H. Morkoç, and Z. Liliental-Weber, *Appl. Phys. Lett.* **89**, 262105 (2006).

## Microstructure investigation of semi-polar (11-22) GaN overgrown on differently designed micro-rod array templates

---

In order to realize semi-polar (11-22) GaN based laser diodes grown on sapphire, it is necessary to further improve the crystal quality of the (11-22) GaN obtained by using our overgrowth approach developed on regularly arrayed micro-rod templates. This can be achieved by carefully designing micro-rod templates. Based on transmission electron microscopy and photoluminescence measurements, it has been found that the micro-rod diameter plays a vital role in effectively reducing both the dislocation density and the basal stacking fault (BSF) density of the overgrown (11-22) GaN, but in different ways. The BSF density reduces monotonically with increasing the micro-rod diameter from 2 to 5  $\mu\text{m}$ , and then starts to be saturated when the micro-rod diameter further increases. In contrast, the dislocation density reduces significantly when the micro-rod diameter increases from 2 to 4  $\mu\text{m}$ , and then starts to increase when the diameter further increases to 5  $\mu\text{m}$ . Furthermore, employing shorter microrods is useful for removing additional BSFs, leading to further improvement in crystal quality. The results presented provide a very promising approach to eventually achieving (11-22) semi-polar III-nitride laser diodes.

### 5.1 Introduction

Although we have developed a cost-effective approach of overgrowth on regularly arrayed micro-rod templates and thus have achieved semi-polar (11-22) GaN on sapphire with significantly improved crystal quality. Based on such overgrown semi-polar (11-22) GaN, we also demonstrated high performance semi-polar InGaN LEDs with an emission wavelength of up to the amber spectral region.<sup>1</sup>

However, it is still a great challenge to achieve lasing on (11-22) GaN on sapphire. So far, all the semi-polar III-nitride laser structures have been grown exclusively on extremely expensive free-standing semi-polar GaN substrates.<sup>2,3</sup> Therefore, it implies that it is necessary to further improve the crystal quality of any overgrown (11-22) GaN on sapphire in order to achieving lasing. In this chapter, by carefully designing micro-rod templates used for our overgrowth, in particular, the diameter and height of the micro-rods used (two major parameters), we have achieved semi-polar (11-22) GaN with best crystal quality on sapphire, which has been systematically studied as a function of the micro-rod parameters by means of multiple characterization methods including photoluminescence (PL), transmission electron microscopy (TEM) and X-ray diffraction (XRD). Furthermore, it has been found that the reduction of both the dislocation density and the BSF density of the overgrown (11-22) GaN is significantly affected by the micro-rod parameters, in particular, the micro-rod diameter, but in different ways. These studies have directly led to stimulated emission very recently achieved on our semi-polar (11-22) GaN on sapphire which has never been reported previously.<sup>4</sup>

Two kinds of single layers of (11-22) GaN (one with a thickness of 1.3  $\mu\text{m}$  and another with 0.4  $\mu\text{m}$ ), which will be subsequently fabricated into micro-rod array templates, are grown on *m-plane* sapphire using our high temperature AlN buffer approach by metal organic chemical vapour deposition (MOCVD).<sup>5</sup> For the fabrication of the micro-rod templates, a 500 nm SiO<sub>2</sub> layer is initially deposited by plasma enhanced chemical vapour deposition (PECVD), followed by a standard photolithography patterning process. Regularly arrayed SiO<sub>2</sub> micro-rods can be achieved by dry etching processes, and the SiO<sub>2</sub> micro-rods then serve as a second mask to etch the GaN underneath in order to form regularly arrayed GaN micro-rods with the SiO<sub>2</sub> remaining on their top. Both the diameter and the spacing of the microrods can be accurately controlled, which simply depend on the micro-rod mask used. A set of micro-rod masks, whose diameters are 2, 2.5, 3, 4, 5, and 7  $\mu\text{m}$ , respectively, have been employed for the fabrication of the micro-rod array templates which will be used for subsequent overgrowth. A study based on a wide range of micro-rod diameters used helps to draw a clear conclusion on the influence of the micro-rod diameter on the reduction of both dislocation density and BSF density. This cannot be achieved using the micro-rod templates with a micro-rod diameter of  $\leq 3.5$   $\mu\text{m}$ , as reported previously.<sup>6</sup> For details of our overgrowth and micro-rod template fabrication, please refer to section 3.4.

## 5.2 BSF reduction with different micro-rod sizes

### 5.2.1 BSF reduction with different micro-rod diameters

Figure 5.1a shows the low temperature (10 K) photoluminescence (PL) spectra of the semi-polar (11-22) GaN overgrown on the regularly arrayed micro-rods with different diameters ranging from 2 to 7  $\mu\text{m}$ . The samples were held in a helium closed-cycle refrigerator. A 325 nm continuous wave (CW) He-Cd laser was used as an excitation source, and luminescence was dispersed using a 0.5 m monochromator and detected using a thermoelectrically (TE) cooled charge-coupled detector (CCD) which can be cooled down to -70  $^{\circ}\text{C}$ . The spectra have been normalized and offset for clarity. The original PL spectra are plotted in 5.1c. As usual, two emission peaks have been observed in each spectrum, one at 356 nm which is attributed to the near band-edge (NBE) emission, and another at 363 nm which is related to the BSFs.<sup>7,8</sup> NBE emission peak in 7  $\mu\text{m}$  micro-rod diameter sample is much stronger than that in 2  $\mu\text{m}$  sample, while the BSF-related emission peak exhibits a huge reduction. The PL intensity ratio of the NBE emission to the BSF-related emission has been plotted as a function of the micro-rod diameter as shown in Figure 5.1b, indicating that with increasing the micro-rod diameter, the ratio exhibits a huge increase from 0.4 to 7.8. Overall, the rising trend of the intensity ratio indicates a significant reduction in the BSF density of our samples with increasing the micro-rod diameter.<sup>9</sup>

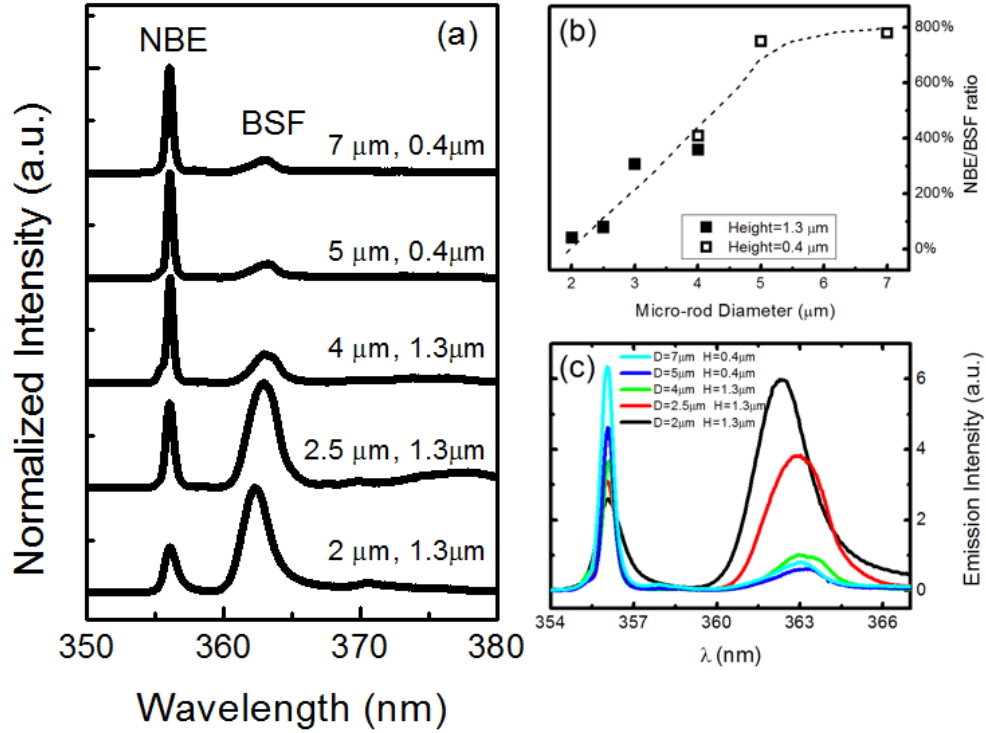


Figure 5.1: (a) Low temperature PL spectra of the (11-22) GaN overgrown on micro-rods with different diameters and heights. The spectra have been normalized and offset for clarity, while the original PL spectra are plotted in (c); (b) PL intensity ratio of the NBE emission to the BSF-related emission is plotted as a function of the micro-rod diameter. The dashed line is a guide to the eye.

TEM measurements have been performed on these samples using a Philips EM430 TEM operating at 200 kV. TEM specimens were prepared by mechanical polishing, followed by an ion beam milling process for electron transparency. Figure 5.2 presents bright field cross-sectional TEM images of semi-polar (11-22) GaN films overgrown on micro-rod templates. All the templates for overgrowth have a same micro-rod height of 1.3 μm, but with different micro-rod diameters of 2, 2.5, 3 and 4 μm, as denoted in the images. Specimens are tilted by 30° to the [-12-10] zone-axis from the [-1100] zone-axis. From the invisibility criterion, BSFs can be observed when the diffraction vector  $\mathbf{g}$  is 1-100. Here, BSFs appear as straight dark lines with an inclination angle of 58.4° to the growth plane. By comparing these samples with different micro-rod diameters, one can find that increasing the micro-rod diameter will decrease the amount of BSFs, hence the BSF-related radiative recombination. This is consistent with the aforementioned low-temperature PL results.

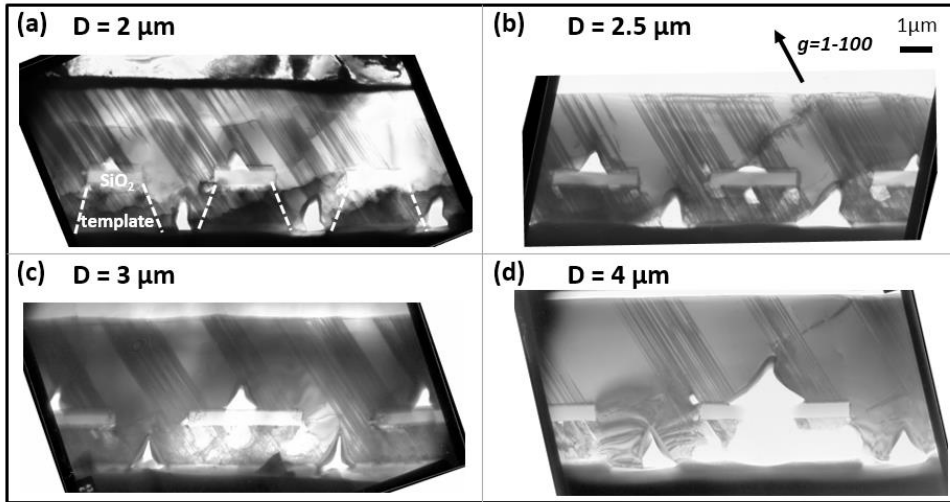


Figure 5.2: Bright field cross-sectional TEM images of overgrown semi-polar (11-22) GaN films viewed along the  $[-12-10]$  zone-axis with  $g = 1-100$ . All these micro-rod templates for overgrowth have a same height of  $1.3 \mu\text{m}$ , but with different diameters ( $D$ : diameter) of 2, 2.5, 3 and  $4 \mu\text{m}$  for (a)-(d), respectively.

Figure 5.3 presents the bright field plane-view TEM images of the overgrown (11-22) GaN on the micro-rod templates fabricated using different micro-rod diameters of 2, 3, 4, and  $5 \mu\text{m}$ , respectively. It should be mentioned that the height of the micro-rods with a micro-rod diameter of 2 or  $3 \mu\text{m}$  ( $D = 2 \mu\text{m}$  and  $D = 3 \mu\text{m}$ ) is  $1.3 \mu\text{m}$ , while those in the other two ( $D = 4 \mu\text{m}$  and  $D = 5 \mu\text{m}$ ) have a height of  $0.4 \mu\text{m}$ . The specimens are tilted around  $32^\circ$  to the  $[-1-120]$  zone-axis from the surface normal. From the invisibility criterion, BSFs can be observed when the diffraction vector  $g$  is  $10-10$ .<sup>10</sup> Figure 5.3 clearly exhibits a periodic distribution of the BSF clusters and BSF-free areas along the  $c$ -projection direction across the surface. The width of the BSF-free area clearly increases with increasing the micro-rod diameter, leading to a reduction in BSF density from  $1.4 \times 10^5 \text{ cm}^{-1}$  in the sample of using a  $2 \mu\text{m}$  micro-rod diameter to  $2.8 \times 10^4 \text{ cm}^{-1}$  in the sample of using a  $5 \mu\text{m}$  micro-rod diameter. It has been understood that the BSFs can penetrate from the micro-rod GaN underneath to the surface only when the overgrowth (starting from the sidewalls of micro-rods) is along the  $a$ -direction, while the growth along the  $c$ -direction leads to free-BSFs.<sup>6</sup> Furthermore, the growth rate along the  $c$ -direction is usually higher than that along the  $a$ -direction. Consequently, the utilization of larger micro-rods along with an increased spacing between micro-rods allows the growth along the  $c$ -direction to more effectively block the penetration of the BSFs caused due to the growth

along the  $a$ -direction. In addition, the width of the BSF clusters does not change significantly with changing the micro-rod diameter as predicted by our defect reduction model. Therefore, the utilization of larger micro-rods for overgrowth can significantly reduce the BSF density, although the overgrowth conditions need to be further optimized in order to maintain quick coalescence.

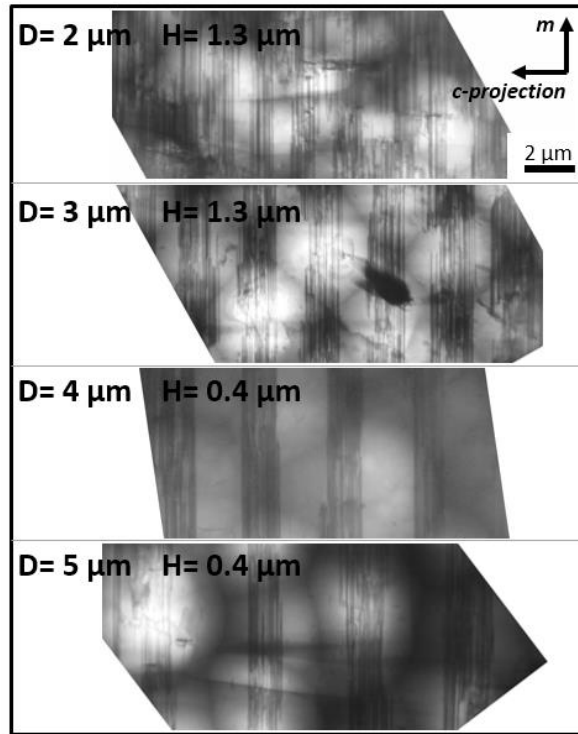


Figure 5.3: Bright field plane-view TEM images of the (11–22) GaN overgrown on micro-rods with different diameters and heights (D: diameter, H: height), as labeled in each figure, where the specimens are viewed along the  $[-1-120]$  zone-axis with the diffraction vector  $g = 10-10$  to show the BSF distribution across the surface;

### 5.2.2 BSF reduction with different micro-rod heights

The relation between the density of BSFs and the micro-rod height has also been investigated. Figure 5.4 shows bright field cross-sectional TEM images of two semi-polar (11–22) GaN films overgrown on the templates with a same micro-rod diameter of  $4 \mu\text{m}$ , but with different micro-rod heights of  $1.3$  and  $0.4 \mu\text{m}$ . Two kinds of BSF clusters can be observed in one period of micro-rod array. The left one (labeled with A) is located around the gap/micro-rod interface, initiating from the left sidewall of the micro-rod. The other one (labeled with B)

is above the SiO<sub>2</sub> layer, originating from the micro-rod in a neighbouring row. As shown in Figure 5.4a, the width of BSF cluster B is thinner than that of cluster A, while in Figure 5.4b, the two BSF clusters appear with a similar width. Comparing the BSF cluster A in two images, one can find that the width of BSF cluster A is clearly reduced by decreasing the height of micro-rod from 1.3 to 0.4 μm, corresponding to a reduction in BSF density from  $4.7 \times 10^4$  to  $3.5 \times 10^4 \text{ cm}^{-1}$ .

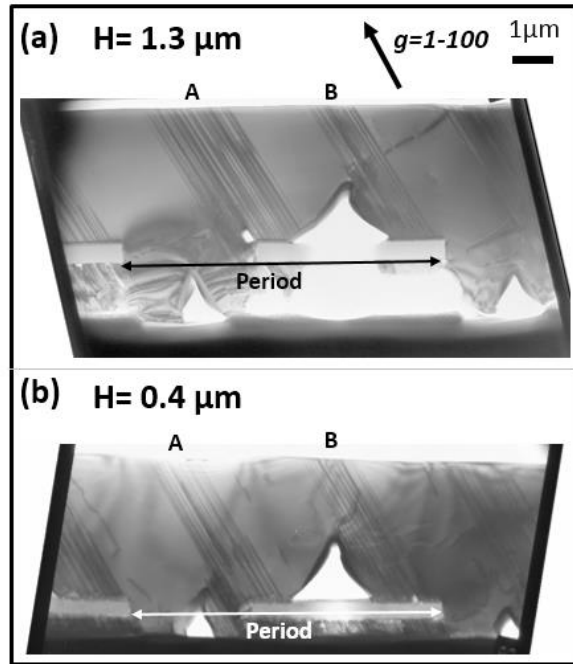


Figure 5.4: Bright field cross-sectional TEM images of semi-polar (11-22) GaN films viewed along the  $[-12-10]$  zone-axis with diffraction vector  $g = 1-100$ . Both the micro-rod templates for overgrowth have a same diameter of 4 μm, but with different heights of 1.3 and 0.4 μm as denoted.

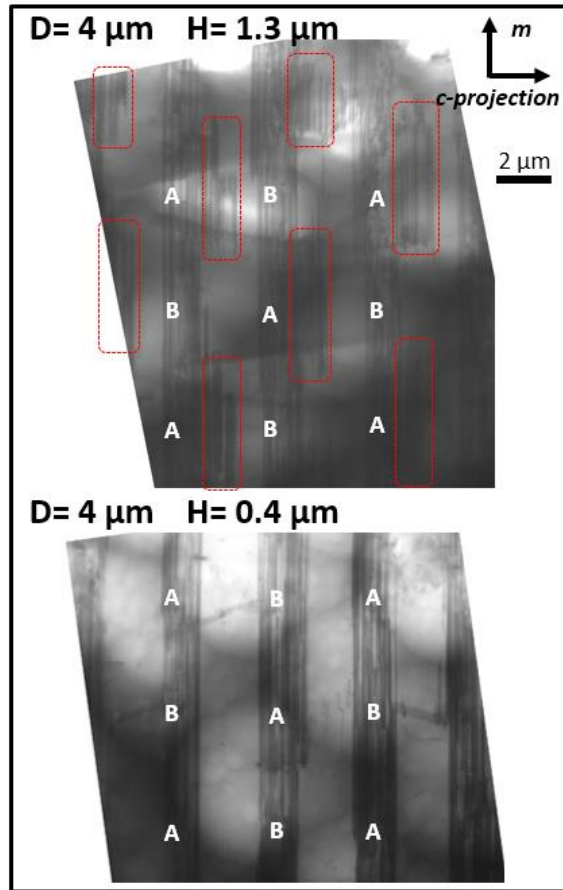


Figure 5.5: Bright field plane-view TEM images of the (11-22) GaN overgrown on the micro-rods with a same micro-rod diameter, but different heights of 1.3 and 0.4  $\mu\text{m}$ , respectively. Specimens are viewed along the  $[-1-120]$  zone-axis with diffraction vector  $\mathbf{g} = 10-10$ .

In order to gain a deeper insight into the mechanism of the influence of the height of the micro-rods, we implemented TEM top-view observation of the two samples. Figure 5.5 shows the plane-view TEM images of two semi-polar (11-22) GaN films overgrown on the micro-rod templates fabricated using a same micro-rod diameter (4  $\mu\text{m}$ ), but with different micro-rod heights (1.3 and 0.4  $\mu\text{m}$ , respectively). In the case of using micro-rods with the 1.3  $\mu\text{m}$  height, beside the long BSF clusters, additional BSF clusters with a periodic distribution have been observed as marked by red dashed lines. From the surface striation direction (parallel to the  $[11-2-3]$ -direction), it can be determined that these additional BSF clusters are distributed along the  $c$ -projection side. However, in the case of using the 0.4  $\mu\text{m}$  height, the TEM image exhibits a sharp interface between the BSF regions and the defect-free areas, namely, there are no such additional BSF clusters. Generally speaking, employing shorter micro-rods for

overgrowth leads to less variation of the diameter of each micro-rod from its bottom to top along the vertical direction. As a result, both the SiO<sub>2</sub> on the top of each micro-rod and the growth along the *c*-direction can effectively stop the penetration of the extra BSFs generated due to the variation of the micro-rod diameter. This is consistent with the low temperature PL results shown above.

Figure 5.6 shows the BSF density of the overgrown (11-22) GaN samples as a function of the micro-rod diameter. Filled and open symbols represent the micro-rods with a height of 1.3 and 0.4 μm, respectively. The BSF density exhibits a clear reduction on the samples grown on larger and shorter micro-rods, agreeing well with our previous prediction based on a model for defect reduction shown by blue dashed lines in the figure. The simulation was made assuming a BSF density of  $4 \times 10^5 \text{ cm}^{-1}$  in the as-grown GaN template used for the fabrication of micro-rod arrays.

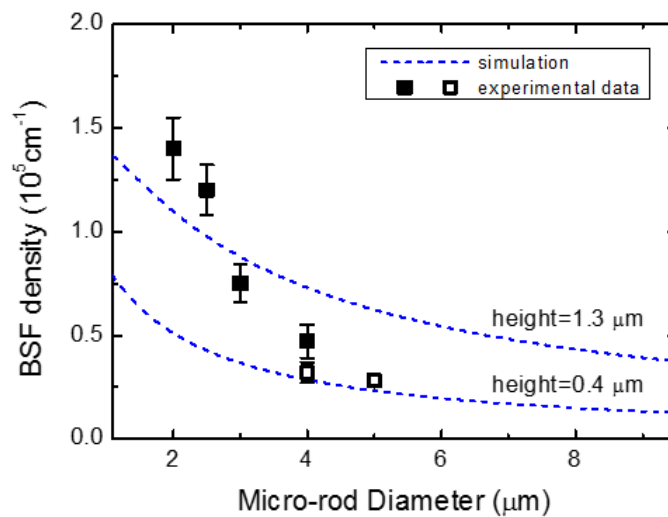


Figure 5.6: BSF density of the overgrown (11-22) GaN as a function of the micro-rod diameter. Filled and open symbols represent the micro-rods with different heights of 1.3 and 0.4 μm, respectively. The dashed lines are the simulation results based on a defect reduction model.

### 5.3 Dislocation reduction with different micro-rod sizes

Figure 5.7 shows cross-sectional TEM images of semi-polar (11-22) GaN films viewed along the [1-100] zone-axis with diffraction vector  $\mathbf{g} = 0002$ , in which case, dislocations with a *c* component can be observed. Micro-rods in Figure 5.7 (a)-(d) have a same micro-rod height

of 1.3  $\mu\text{m}$ , but with different diameters from 2 to 4  $\mu\text{m}$ . It is discovered that the number of dislocations in the overgrown GaN layer presents a clear reduction with increasing the micro-rod diameter. Figure 5.7 (e) and (f) show micro-rods with a same height of 0.4  $\mu\text{m}$ , but with different diameters of 4 and 5  $\mu\text{m}$ . By comparing the samples in Figure 5.7 (d) and (e) with a same micro-rod diameter of 4  $\mu\text{m}$ , the dislocation density shows a slight decrease by reducing the micro-rod height from 1.3  $\mu\text{m}$  to 0.4  $\mu\text{m}$ . In Figure 5.7 (e) and (f), the voids between the micro-rods are located close to the sidewall where the  $a$ -direction GaN growth is allowed, indicating an enhancement in the ratio of GaN growth rate between the  $c$ -direction and the  $a$ -direction. Furthermore, a large void above the  $\text{SiO}_2$  layer is found in the samples overgrown on short micro-rods with large diameter (Figure 5.7 (e) and (f)), which reflects a longer time that is required to reach a second coalescence.

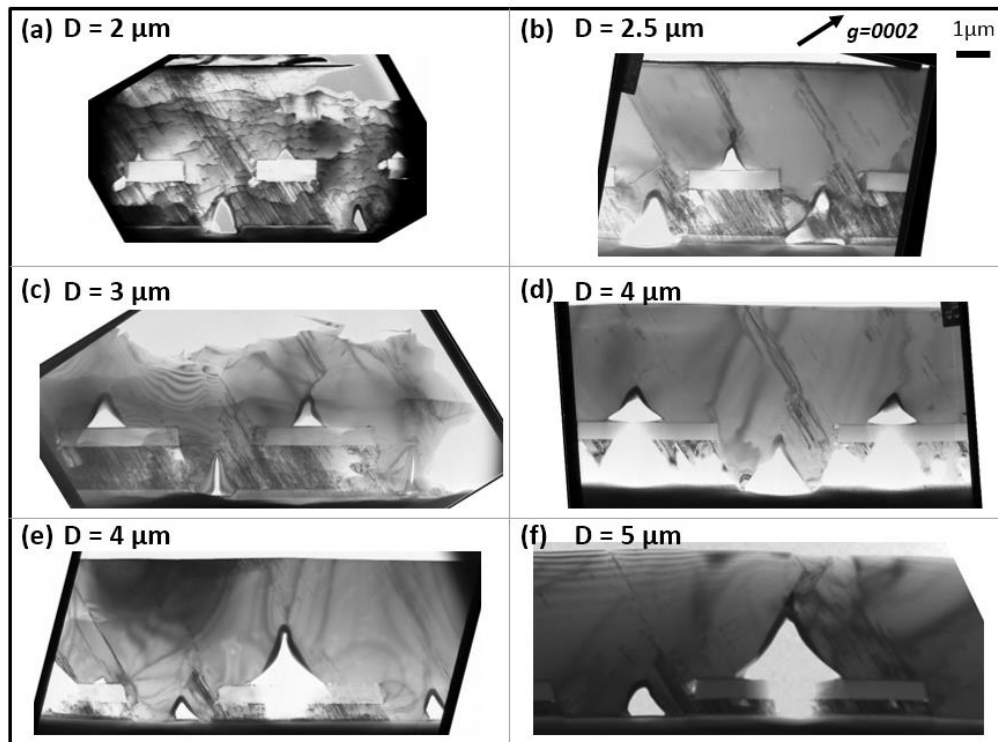


Figure 5.7: Bright field cross-sectional TEM images of semi-polar (11-22) GaN films viewed along the  $[1-100]$  zone-axis with diffraction vector  $g = 0002$ . Micro-rods in (a)-(d) have a same height of 1.3  $\mu\text{m}$ , but with different diameters of 2, 2.5, 3 and 4  $\mu\text{m}$ , while the micro-rods in (e) and (f) have a same height of 0.4  $\mu\text{m}$  and different diameters of 4 and 5  $\mu\text{m}$ .

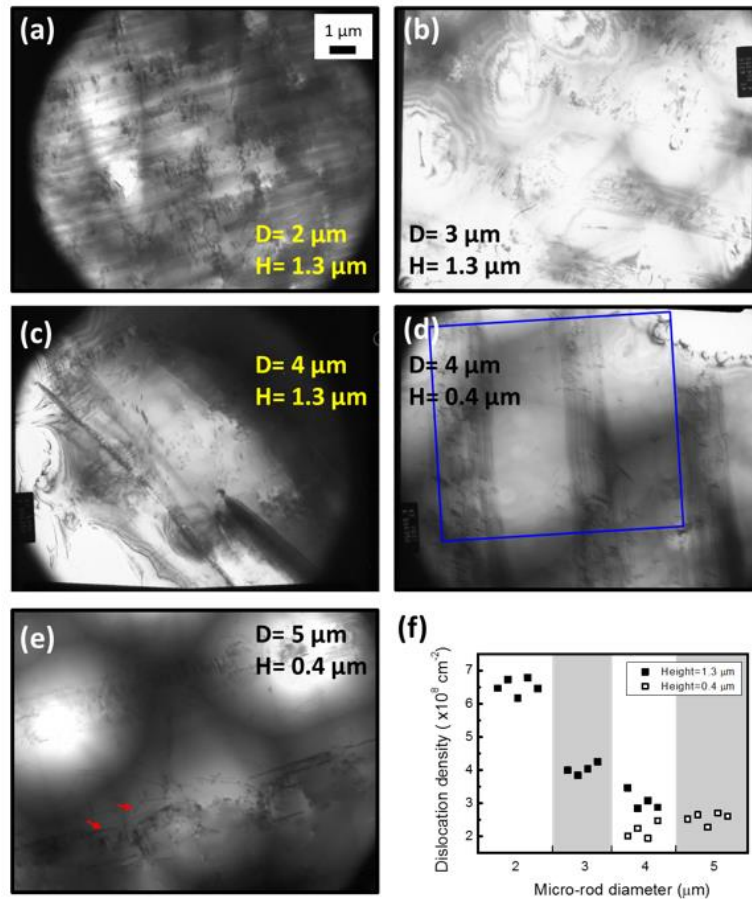


Figure 5.8: (a)-(e) Bright field plane-view TEM images of semi-polar (11-22) GaN films overgrown on the micro-rods with different diameters and heights (D: diameter, H: height), presenting the dislocation distributions across the surface, where the specimens are viewed along the [22-43] zone-axis with the diffraction vector  $\mathbf{g} = 1-212$ ; (f) Dislocation density of the overgrown (11-22) GaN plotted against the micro-rod diameter. Filled and open symbols represent the micro-rods with different heights of 1.3 and 0.4 μm, respectively.

In order to gain a quantitative analysis, dislocation distribution on film surface is also revealed in the TEM observation by tilting the sample at an angle around 7.5 ° from the surface normal to view along the [22-43] zone-axis. In Figure 5.8 (a)-(e) taken with the diffraction vector  $\mathbf{g} = 1-212$ , dislocations including **a**-type, **c**-type, mixed type, and Frank-Shockley partial dislocation ( $\mathbf{b} = 1/6 \langle 20-23 \rangle$ ) are visible, while BSFs are out of contrast. Dislocation density is evaluated by counting dislocations in a large random area which contains both the BSF region and BSF-free region, as the blue square marked in Figure 5.8d. Different areas from the TEM specimen have been investigated to reduce the **statistical** error. The dislocation densities

measured from the TEM observation are plotted against the micro-rod diameter in Figure 5.8f. The dislocation density shows a reduction from  $6.5 \pm 0.4 \times 10^8 \text{ cm}^{-2}$  in the case of using a 2  $\mu\text{m}$  micro-rod diameter down to  $2.2 \pm 0.2 \times 10^8 \text{ cm}^{-2}$  in the case of using a 4  $\mu\text{m}$  micro-rod diameter. Unexpectedly, the dislocation density increases slightly when the micro-rod diameter is further increased to 5  $\mu\text{m}$  with other conditions remaining unchanged. This is different from the BSF behaviours. In addition, threading dislocations with a long dislocation line (marked by red arrows) have been observed in the case of using a 5  $\mu\text{m}$  micro-rod diameter. They are likely generated due to the second coalescence process as a result of using the micro-rods with a larger diameter. Actually, neither BSFs nor dislocations can be observed in the areas between BSF stripes (Figure 5.3 and Figure 5.8), with diffraction vector set either  $g=10\text{-}10$  or  $g=0002$ .

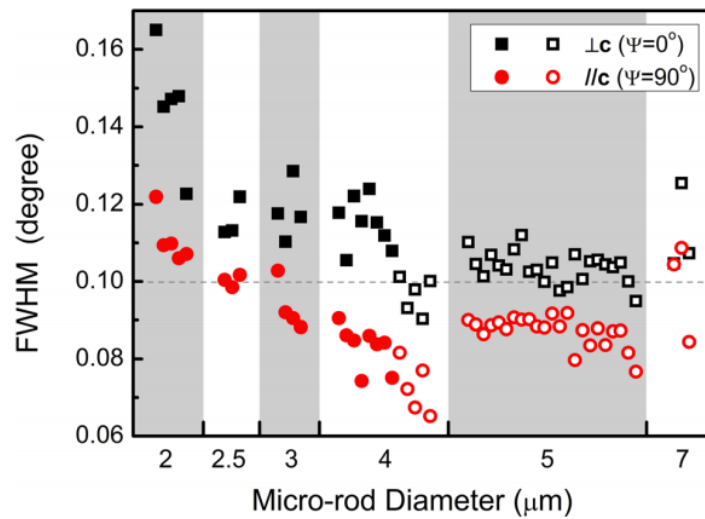


Figure 5.9: A summary of the FWHMs of the on-axis XRD rocking curves of the overgrown (11-22) GaN as a function of the micro-rod diameter. Filled and open symbols represent the micro-rods with different heights of 1.3 and 0.4  $\mu\text{m}$ , respectively.

Furthermore, the crystalline quality of the samples has been characterized by performing X-ray diffraction measurements in order to make a comparison with the above TEM data. Generally speaking, the crystal quality of (11-22) GaN can be evaluated by measuring the full width at half maximum (FWHM) of on-axis X-ray rocking curves as a function of an azimuth angle (labeled as  $\Psi$ ). Typically, the FWHM at the  $0^\circ$  azimuth angle shows the largest value and the FWHM at the  $90^\circ$  azimuth angle the lowest value,<sup>11-13</sup> and these two FWHMs can be used to represent the crystal quality of (11-22) GaN. The azimuth angle is defined as zero when the

projection of the incident X-ray beam is parallel to the *c*-direction of (11-22) GaN. Figure 5.9 provides a summary of the two FWHMs from a large number of the overgrown samples as a function of the micro-rod diameter from 2 to 7  $\mu\text{m}$ . For the as-grown semi-polar GaN templates used for the fabrication of micro-rod templates, the FWHMs are 1345 arc sec ( $0.374^\circ$ ) and 625 arc sec ( $0.174^\circ$ ) at the  $0^\circ$  and  $90^\circ$  azimuth angles, respectively. All the overgrown semi-polar GaN films show a significant reduction in FWHM compared with the as grown templates. With increasing the micro-rod diameter, the FWHMs at both the  $0^\circ$  and the  $90^\circ$  azimuth angles decrease and reach the lowest values in the case of using a 4  $\mu\text{m}$  microrod diameter, demonstrating the FWHMs of 325 and 235 arc sec at the  $0^\circ$  and the  $90^\circ$  azimuth angles, respectively. However, with further increasing the micro-rod diameter to 5 and 7  $\mu\text{m}$ , the FWHMs at both the  $0^\circ$  and the  $90^\circ$  azimuth angles increase slightly, meaning an increase in dislocation density. The slight degradation of the crystal quality in the case of using the larger micro-rod diameters agrees well with the dislocation densities measured by TEM as shown in Figure 5.8f. Compared with a previous report of an average FWHM of 410 arc sec of the rocking curve, our XRD data represent a record crystal quality of (11-22) GaN obtained on sapphire substrates.<sup>15</sup> Overall, these low FWHM values are comparable to those for commercial *c*-plane GaN LEDs, implying a great potential to achieve outstanding optical devices on these semi-polar (11-22) GaN films. Furthermore, our previous report based on the micro-rod templates with a small microrod diameter showed a 346 arc sec FWHM of XRD rocking curve,<sup>14</sup> while the present study provides XRD data as a function of micro-rod diameter including a record narrow FWHM of XRD rocking curve which is 235 arc sec (achieved using a 4  $\mu\text{m}$  micro-rod diameter). This further confirms a step change in crystal quality.

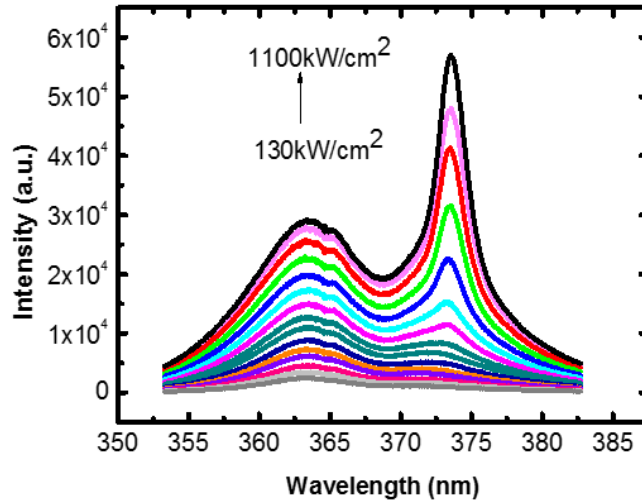


Figure 5.10: Emission spectra of a (11-22) overgrown GaN film with various pumping power densities.<sup>4</sup>

Figure 5.10 shows the emission spectra of a (11-22) overgrown GaN film with different excitation power densities from 130 to 1100 kW/cm<sup>2</sup>.<sup>4</sup> A stimulated emission process is observed as the appearance of an emission peak around 374 nm at a higher pumping power density. It is worth highlighting that this stimulated emission was achieved on semi-polar (11-22) GaN overgrown on the micro-rods with a 4 μm diameter and a 0.4 μm height, despite the fact that the BSF density in the 4 μm sample is not the lowest (while the 4 μm sample shows the lowest dislocation density. This suggests that dislocations instead of BSFs may play a critical role in determining the optical performance of (11-22) semi-polar GaN based emitters.

## 5.4 Summary

In conclusion, semi-polar (11-22) GaN films overgrown on micro-rod arrays with different diameters have been investigated. The PL intensity ratio of the NBE emission to the BSF related emission exhibits a monotonic increase with increasing the micro-rod diameter. TEM measurements further demonstrate that the lower BSF density can be obtained in the (11-22) GaN overgrown on larger and shorter microrods. On the other hand, the dislocation density in the GaN films decreases to the lowest value with increasing the micro-rod diameter of up to 4 μm. The XRD measurements confirms that the best crystal quality of the overgrown (11-22) GaN is achieved by overgrowth on micro-rods with a 4 μm diameter and a 0.4 μm height, leading to achieving stimulated emission.

## References

- 1 J. Bai, B. Xu, F. G. Guzman, K. Xing, Y. Gong, Y. Hou, and T. Wang, *Appl. Phys. Lett.* **107**, 261103 (2015).
- 2 H. Asamizu, M. Saito, K. Fujito, J. S. Speck, S. P. DenBaars, and S. Nakamura, *Appl. Phys. Express* **1**, 91102 (2008).
- 3 Y. Enya, Y. Yoshizumi, T. Kyono, K. Akita, M. Ueno, M. Adachi, T. Sumitomo, S. Tokuyama, T. Ikegami, K. Katayama, and T. Nakamura, *Appl. Phys. Express* **2**, 82101 (2009).
- 4 B. Xu, L. Jiu, Y. Gong, Y. Zhang, L. C. Wang, J. Bai, and T. Wang, *AIP Adv.* **7**, 045009 (2017).
- 5 T. Wang, K. B. Lee, J. Bai, P. J. Parbrook, R. J. Airey, Q. Wang, G. Hill, F. Ranalli, and A. G. Cullis, *Appl. Phys. Lett.* **89**, 81126 (2006).
- 6 Y. Zhang, J. Bai, Y. Hou, R. M. Smith, X. Yu, Y. Gong, and T. Wang, *AIP Adv.* **6**, 25201 (2016).
- 7 R. Liu, A. Bell, F. A. Ponce, C. Q. Chen, J. W. Yang, and M. A. Khan, *Appl. Phys. Lett.* **86**, 21908 (2005).
- 8 P. De Mierry, N. Kriouche, M. Nemoz, and G. Nataf, *Appl. Phys. Lett.* **94**, 191903 (2009).
- 9 S. J. Rosner, E. C. Carr, M. J. Ludowise, G. Girolami, and H. I. Erikson, *Appl. Phys. Lett.* **70**, 420 (1997).
- 10 F. Wu, Y. D. Lin, A. Chakraborty, H. Ohta, S. P. DenBaars, S. Nakamura, and J. S. Speck, *Appl. Phys. Lett.* **96**, 231912 (2010).
- 11 Q. Sun, B. Leung, C. D. Yerino, Y. Zhang, and J. Han, *Appl. Phys. Lett.* **95**, 231904 (2009).
- 12 M. A. Moram, C. F. Johnston, J. L. Hollander, M. J. Kappers, and C. J. Humphreys, *J. Appl. Phys.* **105**, 113501 (2009).
- 13 M. B. McLaurin, A. Hirai, E. Young, F. Wu, and J. S. Speck, *Jpn. J. Appl. Phys.* **47**, 5429 (2008).
- 14 Y. Gong, K. Xing, B. Xu, X. Yu, Z. Li, J. Bai, and T. Wang, *ECS Trans.* **66**, 151 (2015).
- 15 F. Tendille, M. Hugues, P. Vennéguès, M. Teisseire, and P. De Mierry, *Semicond. Sci. Technol.* **30**, 065001 (2015).



## Stokes Shift in Semi-polar (11-22) InGaN/GaN Multiple Quantum Wells

---

The mechanism for the large Stokes shifts of InGaN/GaN structures is under debate. In this chapter, a systematic study was carried out on the Stokes shift of semi-polar (11-22) InGaN/GaN multiple quantum wells (MQWs) with a wide spectral range from green to yellow by means of both photoluminescence excitation (PLE) and time resolved PL measurements in comparison with their *c*-plane counterparts. The semi-polar samples exhibit a lower Stokes shift than their *c*-plane counterparts, although they show stronger localization effects than their *c*-plane counterparts. In the long wavelength region, the Stokes shift of the semi-polar MQWs shows a linear relationship with emission energy, but with a smaller gradient compared with their *c*-plane counterparts. The time-resolved PL measurements confirm a significant reduction in piezoelectric field of the semi-polar samples compared with the *c*-plane counterparts. It is suggested that the piezoelectric field induced polarization is the major mechanism for causing the large Stokes shift. The results presented contribute to better understanding of the long standing issue on the mechanism for the large Stokes shift.

### 6.1 Introduction

Tremendous progress has been made in the field of III-nitride optoelectronics grown on (0001) sapphire within last two decades, represented by high brightness InGaN/GaN based blue emitters, leading to three Nobel Prize Winners in 2014. However, there are still great challenges to be overcome to improve the optical performance of InGaN/GaN based structures when moving towards the longer wavelength, such as the green and yellow spectral region.<sup>1</sup> Due to the large lattice mismatch between InN and GaN, strain-induced piezoelectric fields along the *c*-direction are generated across the InGaN/GaN based active layer, causing the well-known quantum-confined Stark effect (QCSE). This separates the electron and hole wavefunctions in opposite directions, leading to a great decrease in radiative transition rate and thus optical quantum efficiency. On the other hand, the solid immiscibility between InN and GaN

makes it difficult to grow InGaN with high indium content, which is necessary for the emitters with long emission wavelengths.<sup>2</sup> To circumvent the problems caused by the internal electric fields, a promising solution is to grow InGaN/GaN structures along either non-polar or semi-polar orientation in order to eliminate or reduce the polarization fields.<sup>3</sup> Furthermore, in comparison with either polar or non-polar planes, semi-polar (11-22) GaN exhibits a higher indium incorporation ability as a result of a much lower indium chemical potential on its surface than either the non-polar or polar surface.<sup>4</sup> In this case, InGaN grown along the (11-22) direction can accommodate more indium atoms under same growth conditions, potentially allowing us to obtain InGaN layers with high indium content, which is essential for green and yellow emitters.

The difference between emission energy and absorption energy in semiconductor materials, known as Stokes shift, can be measured by photoluminescence excitation (PLE) measurements. Up until now, the issue on the large Stokes shift in *c*-plane InGaN/GaN structures (polar) has been studied extensively,<sup>5-10</sup> but the mechanisms for the large Stokes shifts are controversial, as two major issues, both QCSE and indium segregation induced localization effects existing in *c*-plane InGaN/GaN structures simultaneously, cannot be clearly separated. Furthermore, it is very difficult to achieve emission with long wavelengths using *c*-plane InGaN/GaN structures. Therefore, it is a great challenge to draw a clear and universal conclusion for the cause of the large Stokes shifts of InGaN/GaN structures. In order to address the challenging issue, it is necessary to investigate the Stokes shift of semi-polar InGaN/GaN structures with high crystal quality, and also compare with *c*-plane InGaN/GaN structures. (A non-polar InGaN/GaN structure would be ideal, but as mentioned above it would be almost impossible to achieve emission with long wavelengths using non-polar InGaN/GaN structures. Therefore, it would be difficult to draw a universal conclusion if we would use non-polar InGaN/GaN structures).

However, owing to great technological challenges in growing high quality semi-polar (11-22) GaN, there is almost an absence of reports on the study of the Stokes shift of semi-polar (11-22) InGaN/GaN multiple quantum well (MQW) structures. Recently, we have developed a number of cost-effective approaches to the overgrowth of semi-polar GaN.<sup>11-13</sup> On such high crystal quality semi-polar GaN, our group has grown a number of semi-polar (11-22) InGaN/GaN MQW samples with high optical performance by metalorganic chemical vapour deposition (MOCVD), allowing us to systematically investigate the optical properties of semi-

polar InGaN/GaN MQWs. This chapter presents a systematic study of the Stokes shifts of a series of high-quality semi-polar (11-22) InGaN/GaN MQWs with a wide spectral range by both PLE and time resolved PL measurements, and then compare with *c*-plane InGaN/GaN MQWs. Although the semi-polar InGaN/GaN MQWs demonstrate deeper localized states than the *c*-plane counterparts over a wide spectral range, the Stokes-shifts of the semi-polar InGaN/GaN MQWs are generally much smaller than those of the *c*-plane counterparts. This clearly demonstrates the piezoelectric field induced polarization would be the major mechanism for causing the large Stokes shifts of InGaN/GaN MQWs, even with high indium content, where the localization effect is also very strong.

## **6.2 Stokes shift in semi-polar (11-22) MQWs**

### **6.2.1 Semi-polar (11-22) InGaN/GaN MQWs**

High quality semi-polar (11-22) GaN films have been achieved by a micro-rod template overgrowth approach that was introduced in section 3.4. Based on these GaN wafers, a number of InGaN/GaN MQWs samples with a wide spectral range have been obtained. The growth temperatures for barrier layer are all 900 °C, while those for well layer vary from 815 °C to 788 °C to tune the emission wavelength. The emission wavelengths of these semi-polar samples span from 497 to 591 nm, covering the whole green and yellow spectral ranges. Figure 6.1 shows PL spectra of several semi-polar (11-22) InGaN/GaN MQWs excited by a 375 nm pulsed laser at low temperature (7 K). The linewidth of the PL spectra increases with emission peak moving towards longer wavelength, which is attributed to the increasing fluctuation in indium composition. The indium compositions in these semi-polar samples range from 27% to 47%, demonstrating a great enhancement in indium incorporation over either *c*-plane or non-polar orientation. For comparison, a number of standard *c*-plane InGaN/GaN MQWs samples with indium composition varying from 13% to 32% have also been used for PLE measurements.

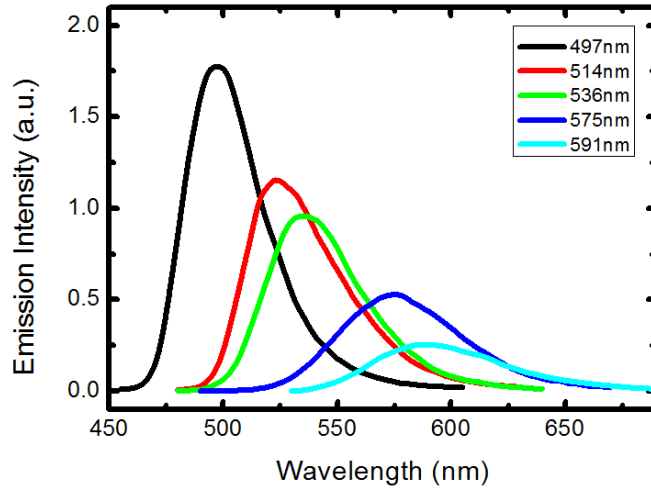


Figure 6.1: PL spectra of several semi-polar (11-22) InGaN/GaN MQWs at low temperature (7K).

### 6.2.2 Stokes shift

PLE measurements have been carried out on all the samples loaded in a closed cycle helium cryostat at 12 K. A laser pumped plasma broadband light source with a high density (Energetiq LDLS EQ-99) dispersed by a 320 mm Horiba monochromator is employed as a tunable optical excitation source. The luminescence is dispersed by a 550 mm monochromator and detected by a cooled GaAs photocathode photomultiplier tube (PMT).

As an example, Figure 6.2 shows PL and PLE spectra from a pair of *c*-plane (polar) and semi-polar (11-22) InGaN/GaN MQWs samples, both measured at 12 K. The PL measurements were carried out with an excitation wavelength of 350 nm, and the PLE measurements have been conducted using their emission peak energies. The two samples show similar peak emission energies located at 2.304 eV (538 nm) and 2.322 eV (534 nm), respectively. The full width at half maximum (FWHM) of the PL spectrum from the semi-polar sample is 187 meV, which is slightly larger than the 166 meV for the *c*-plane sample. The contribution to the PL linewidth broadening as a result of a fluctuation in quantum well thickness can be safely excluded by performing detailed transmission electron microscopy (TEM) measurements, in which flat quantum wells with a uniform thickness have been demonstrated. Therefore, it is suggested that the broadening of the emission peak in the semi-polar MQWs results from a potential fluctuation caused by an indium segregation within the InGaN quantum wells.<sup>14</sup> Due to the reduced piezoelectric polarization along the semi-polar orientation compared to the *c*-

direction, semi-polar InGaN/GaN MQWs require higher indium content than their *c*-plane counterparts in order to achieve a similar emission wavelength. This is expected to lead to stronger localized states in semi-polar MQWs than their *c*-plane counterparts.

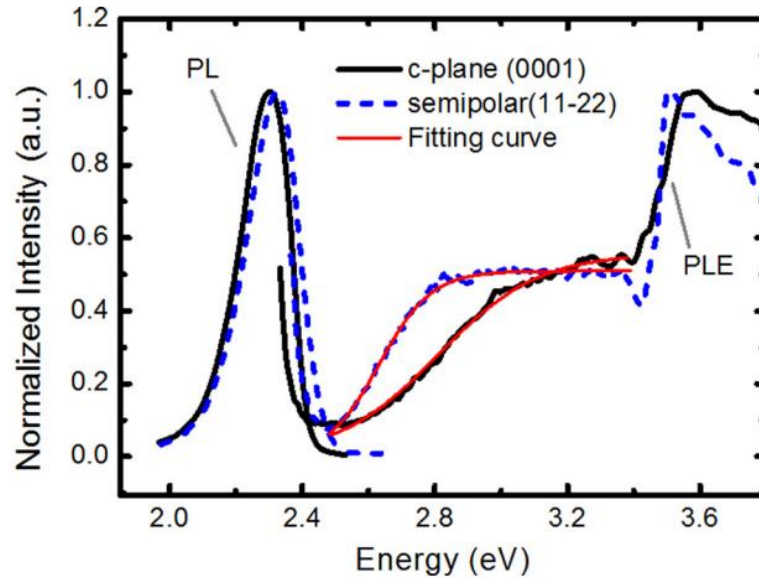


Figure 6.2: Low temperature (12 K) PL/PLE spectra of one polar (solid line) and one semi-polar (11-22) (dashed line) InGaN/GaN MQW samples with emission energy of 2.304 eV (538 nm) and 2.322 eV (534 nm), respectively.

PLE measurements were carried out at 12 K with a detection wavelength fixed at each PL peak wavelength. Two absorption edges, associated with the GaN barriers at around 3.43 eV and InGaN quantum wells at the low energy side respectively, can be seen in both PLE spectra. Comparing the InGaN-related absorption edge in two samples, it is found that the InGaN-related absorption process in the *c*-plane sample covers a wider range of energy (from 3.2 to 2.5 eV) than that in the semi-polar sample (from 2.87 to 2.5 eV) despite the fact that the PL spectrum of the *c*-plane sample is narrower than that of the semi-polar sample. The broadening of the quantum well absorption edge in the *c*-plane sample can be attributed to the quantum confined Franz-Keldysh (QCFK) effects.<sup>15</sup> Due to the internal electric fields, some optical transitions that are normally forbidden may have an chance to become allowed in an absorption process, broadening the quantum well absorption edge.<sup>16</sup> The steep absorption edge in the semi-polar sample is an evidence for the reduced QCFK effects, resulting from the reduced piezoelectric fields in the quantum wells. In order to quantitatively analyze the Stokes shift, the InGaN-related absorption edges can be extracted by fitting with a sigmoidal formula:<sup>9</sup>

$$a = a_0/[1 + \exp\left(\frac{E_B - E}{\Delta E}\right)] \quad (6.1)$$

where  $E_B$  is the effective absorption edge;  $\Delta E$  is a broadening parameter related to the Urbach tailing energy; and  $a_0$  is a constant. The fitted absorption edges are 2.813 eV and 2.634 eV for the  $c$ -plane and semi-polar samples, respectively. Therefore, the Stokes shift in the  $c$ -plane sample is 509 meV, which is larger than the 312 meV for the semi-polar sample.

By comparing the barrier GaN-related absorption edge in two samples, it is found the absorption edge in semi-polar (11-22) InGaN/GaN MQWs is slightly smaller than that in the  $c$ -plane sample. This shows the bandgap of the semi-polar GaN is smaller than that of conventional  $c$ -plane GaN on sapphire, indicating a strain relaxation in the overgrown semi-polar GaN layer, which is ascribed to the formation of regularly distributed air voids during the overgrowth.<sup>17</sup>

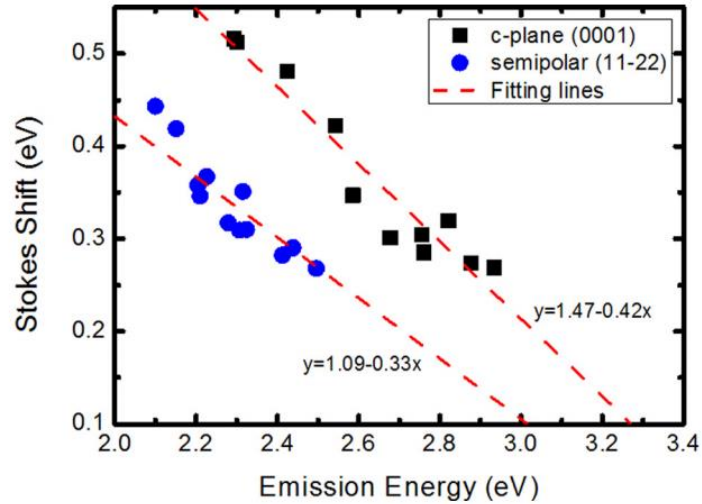


Figure 6.3: Stokes Shift as a function of emission energy in polar (0001) and semi-polar (11-22) InGaN/GaN MQWs measured at 12 K.

PL and PLE measurements have been carried on a wide range of polar and semi-polar (11-22) MQWs samples under the same conditions in order to find a universal rule. The obtained Stokes shift values of the  $c$ -plane and semi-polar samples as a function of the emission energy are shown in Figure 6.3. Among these  $c$ -plane samples, the Stokes shift values linearly decrease with increasing emission energy, and tend to zero at 3.50 eV (i.e., around the GaN bandgap), which is consistent with the previous work reported by other groups.<sup>10</sup> In

contrast, all the semi-polar MQW samples show a lower Stokes shift than their *c*-plane counterparts with same emission wavelengths in a wide spectral range of up to yellow. Figure 6.3 shows a linear relationship between the Stokes shift and the emission energy for both the semi-polar samples and the *c*-plane samples. However, the gradient of the fitting line for the semi-polar samples is smaller than that for the *c*-plane MQWs samples, as denoted beside the fitting lines in Figure 6.3. Moreover, the fitting line intercepts with the x-axis at 3.30eV, a slight deviation from the GaN bandgap, for which the mechanism is still on investigation.

### 6.2.3 QCSE in InGaN/GaN MQWs

Since the Stokes shift of InGaN/GaN quantum well structures can be affected by either the piezoelectric field or exciton localization effects or both, low temperature Time-resolved PL (TRPL) measurements have been performed on these polar and semi-polar samples in order to further investigate the issue. TRPL measurements were performed utilizing a time-correlated single photon counting (TCSPC) technique with a 375nm pulsed diode laser with a pulse width of 83 picoseconds as an excitation source and a hybrid Hamamatsu PMT as a single photon detector. Due to the QCSE caused by the electric fields across the quantum wells, the probability of optical transitions is reduced. With a widely accepted assumption that non-radiative recombination can be effectively suppressed at a low temperature, such as ~10 K, it is expected that the QCSE leads to an increase in PL decay lifetime. Furthermore, the stronger the QCSE, the longer the recombination lifetime of carriers at a low temperature.

As an example, Figure 6.4 shows the PL decay traces of two pairs of polar and semi-polar InGaN/GaN MQWs samples with similar emission wavelengths in the green spectral region. The PL decay traces were monitored at their respective emission peak wavelength and can be fitted typically using a bi-exponential equation below:<sup>18</sup>

$$I = A_1 e^{-\frac{t}{\tau_1}} + A_2 e^{-\frac{t}{\tau_2}} \quad (6.2)$$

where  $\tau_1$  and  $\tau_2$  are the decay lifetimes of fast and slow components, respectively;  $A_1$  and  $A_2$  are constants. The fitting curves are plotted in dashed lines, and the fast decay lifetimes from the fitting are also denoted beside the curves in Figure 6.4.

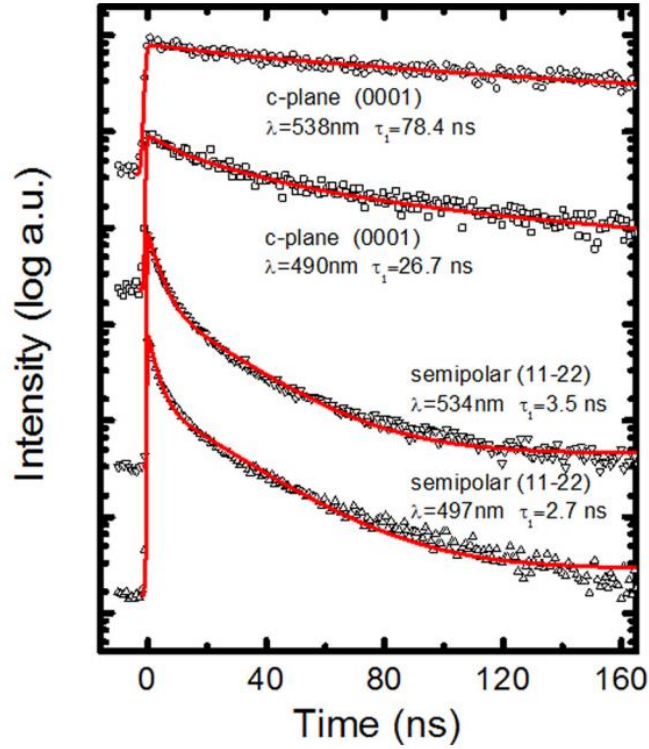


Figure 6.4: Decay traces of two polar (0001) and two semi-polar (11-22) InGaN/GaN MQW samples with different emission wavelengths measured at 7 K (data are offset for clarity). The dashed lines are the fitting curves with two exponential components model.

As usual a very long lifetime is generally found in the *c*-plane samples, indicating the existence of extremely strong QCSE caused by the internal electric field across the quantum wells. However, the recombination lifetimes of the semi-polar InGaN/GaN MQW samples is approximately one order of magnitude shorter than those observed for the *c*-plane samples, proving a significant decrease in QCSE. A calculation based on a theoretical modelling and analysis made by Brown *et al.* shows that the piezoelectric fields in semi-polar InGaN samples are approximately four times smaller than those in their *c*-plane counterparts with similar emission wavelengths.<sup>19,20</sup> As the QCSE increases with increasing indium composition in both polar and semi-polar samples, the sample with a longer emission wavelength exhibits a longer PL lifetime, which is true for the *c*-plane samples. For an example, the recombination lifetime of the *c*-plane sample ( $\lambda = 490$  nm) is 26.7 ns, three times shorter than the 78.4 ns of the *c*-plane sample ( $\lambda = 538$  nm). In contrast, for the semi-polar samples, the lifetime changes from 2.7 ns at 497 nm to 3.5 ns at 534 nm, being less sensitive to a change in indium composition

compared with the *c*-plane samples. This means that the change of the QCSE with increasing emission wavelength becomes smaller for the semi-polar sample compared with their *c*-plane counterparts, which can lead to a reduced slope of the fitting line in Figure 6.3 if the piezoelectric field induced polarization dominates the mechanism for the Stokes shift.

#### 6.2.4 Localization in InGaN/GaN MQWs

Carrier localization is another major factor that affects the Stokes shift in InGaN/GaN MQWs. Wavelength-dependent TRPL measurement has been widely used in evaluating carrier localization energy. As schematized in Figure 6.5, carriers can move among the potential minima caused by potential fluctuations.<sup>21</sup> As a result of the presence of these migration processes, radiative recombination from a low energy level would take a longer time than that from a high energy level. Thus, carrier lifetime will change as a function of the emission energy.

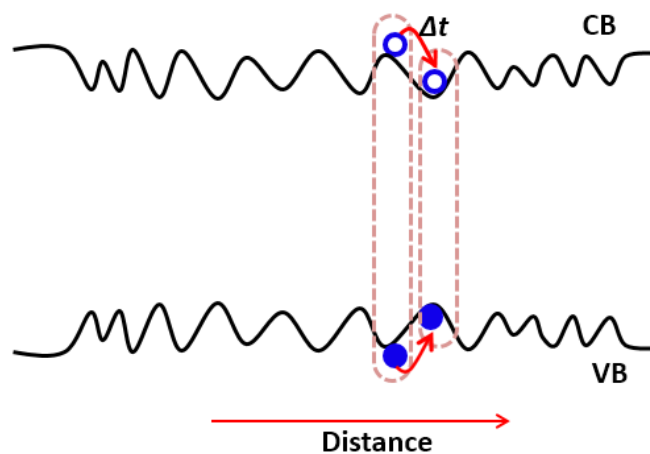


Figure 6.5: Schematic diagram of recombination processes for carriers at different energy levels.

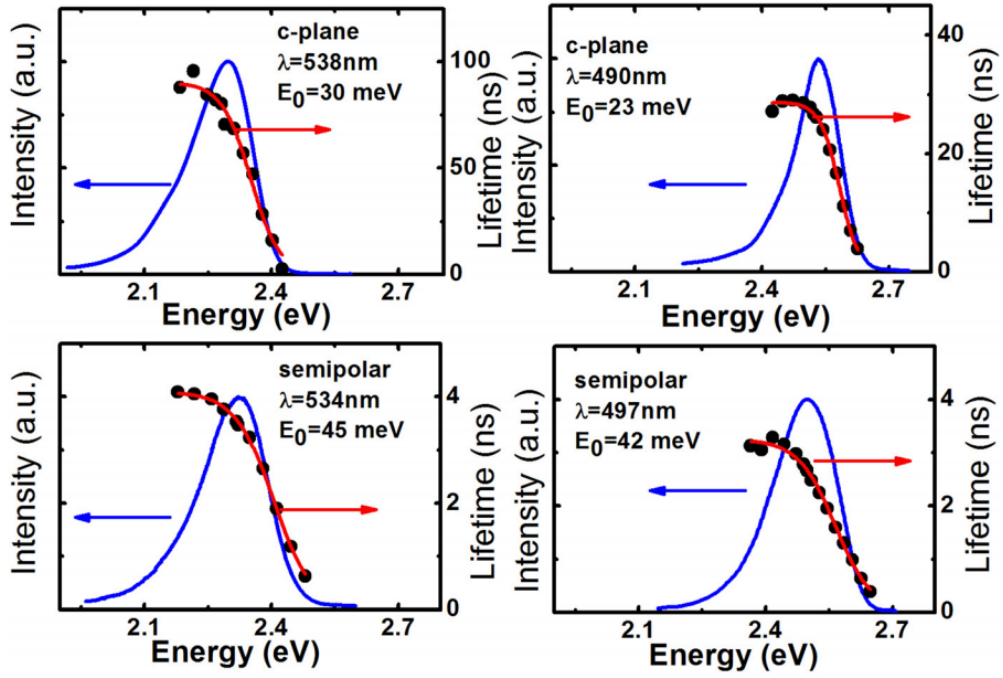


Figure 6.6: PL decay time as a function of emission energy for two polar (0001) and two semi-polar (11-22) InGaN/GaN MQW samples with different emission wavelengths measured at 7 K. The red lines are the fitting results.

Wavelength-dependent TRPL measurements have been conducted at a low temperature (7 K) to study the localization effects in these samples. Figure 6.6 presents the fast decay lifetime as a function of the monitored photon energy of the four samples as examples mentioned above. The recombination lifetime decreases with increasing detection energy, indicating the existence of localized excitons in exponential-tail density of states.<sup>22</sup> This can be described by:

$$\tau = \tau_{rad} / [1 + \exp\left(\frac{E - E_m}{E_0}\right)] \quad (6.3)$$

where  $\tau_{rad}$  and  $E_m$  are the radiative lifetime and the energy of the mobility edge, respectively;  $E_0$  represents the exciton localization depth. For the *c*-plane samples, the obtained localization depths are 30 meV and 23 meV for the emission wavelengths at 538 nm and 490 nm, respectively, while the semi-polar samples exhibit localization depths of 45 meV at 534 nm, and 42 meV at 497 nm. Although the Stokes shift values in the semi-polar samples are much smaller than those in the *c*-plane samples, the localization depths in the semi-polar samples are larger than those in the polar samples. This demonstrates that carrier localization effects only

contribute a small part to the Stokes shift, compared with the presence of piezoelectric fields.<sup>23</sup> The small Stokes shift for the semi-polar samples results from the significant reduction of the piezoelectric fields. The smaller gradient of fitting line in semi-polar samples results from the fact that the change of the piezoelectric field at different emission wavelengths in semi-polar samples is smaller than that of the *c*-plane samples.

### **6.3 Summary**

In summary, both PLE and TRPL measurements have been performed on a large number of semi-polar (11-22) InGaN/GaN MQWs with a wide spectral range of up to yellow grown on our high crystal quality semi-polar GaN, allowing us to systemically investigate the mechanism for the large Stokes shift. Although the semi-polar InGaN/GaN MQWs exhibit larger exciton localization than their *c*-plane counterparts, they display a lower Stokes shift compared with the corresponding *c*-plane counterparts. Furthermore, the Stokes shift values for both the semi-polar samples and their counterparts exhibit a linear relationship with their emission energy, but the semi-polar samples with a reduced gradient. All these demonstrate that the piezoelectric field induced polarization is the major mechanism for causing the large Stokes shift.

## References

- 1 F. Scholz, *Semicond. Sci. Technol.* **27**, 24002 (2012).
- 2 I. Ho and G. Stringfellow, *Appl. Phys. Lett.* **69**, 2701 (1996).
- 3 M. Beeler, E. Trichas, and E. Monroy, *Semicond. Sci. Technol.* **28**, 74022 (2013).
- 4 J. E. Northrup, *Appl. Phys. Lett.* **95**, 133107 (2009).
- 5 H. C. Yang, P. F. Kuo, T. Y. Lin, Y. F. Chen, K. H. Chen, L. C. Chen, and J. I. Chyi, *Appl. Phys. Lett.* **76**, 3712 (2000).
- 6 H. S. Kwack, B. J. Kwon, J. S. Chung, Y. H. Cho, S. Y. Kwon, H. J. Kim, and E. Yoon, *Appl. Phys. Lett.* **93**, 161905 (2008).
- 7 Y. H. Cho, J. J. Song, S. Keller, M. S. Minsky, E. Hu, U. K. Mishra, and S. P. DenBaars, *Appl. Phys. Lett.* **73**, 1128 (1998).
- 8 Z. C. Feng, L. H. Zhu, T. W. Kuo, C. Y. Wu, H. L. Tsai, B. L. Liu, and J. R. Yang, *Thin Solid Films* **529**, 269 (2013).
- 9 K. P. O'Donnell, R. W. Martin, and P. G. Middleton, *Phys. Rev. Lett.* **82**, 237 (1999).
- 10 R. W. Martin, P. G. Middleton, K. P. O'Donnell, and W. Van der Stricht, *Appl. Phys. Lett.* **74**, 263 (1999).
- 11 K. Xing, Y. Gong, J. Bai, and T. Wang, *Appl. Phys. Lett.* **99**, 181907 (2011).
- 12 J. Bai, Y. Gong, K. Xing, X. Yu, and T. Wang, *Appl. Phys. Lett.* **102**, 101906 (2013).
- 13 Y. Gong, K. Xing, B. Xu, X. Yu, Z. Li, J. Bai, and T. Wang, *ECS Trans.* **66**, 151 (2015).
- 14 N. P. Hylton, P. Dawson, C. F. Johnston, M. J. Kappers, J. L. Hollander, C. McAleese, and C. J. Humphreys, *Phys. Status Solidi* **6**, S727 (2009).
- 15 S. F. Chichibu, A. C. Abare, M. S. Minsky, S. Keller, S. B. Fleischer, J. E. Bowers, E. Hu, U. K. Mishra, L. A. Coldren, S. P. DenBaars, and T. Sota, *Appl. Phys. Lett.* **73**, 2006 (1998).
- 16 D.A.B. Miller, D.S. Chemla, and S. Schmitt-Rink, *Phys. Rev. B* **33**, 6976 (1986).
- 17 Y. Zhang, J. Bai, Y. Hou, R. M. Smith, X. Yu, Y. Gong, and T. Wang, *AIP Adv.* **6**, 25201 (2016).
- 18 S. F. Chichibu, K. Hazu, Y. Ishikawa, M. Tashiro, H. Namita, S. Nagao, K. Fujito, and A. Uedono, *J. Appl. Phys.* **111**, 103518 (2012).
- 19 W. Chow, M. Kira, and S. Koch, *Phys. Rev. B* **60**, 1947 (1999).

- 20 I. H. Brown, P. Blood, P. M. Smowton, J. D. Thomson, S. M. Olaizola, A. M. Fox, P. J. Parbrook, and W. W. Chow, *IEEE J. Quantum Electron.* **42**, 1202 (2006).
- 21 H. He, Q. Yu, H. Li, J. Li, J. Si, Y. Jin, N. Wang, J. Wang, J. He, X. Wang, Y. Zhang, and Z. Ye, *Nat. Commun.* **7**, 10896 (2016)
- 22 S. F. Chichibu, T. Azuhata, H. Okumura, A. Tackeuchi, T. Sota, and T. Mukai, *Appl. Surf. Sci.* **190**, 330 (2002).
- 23 E. Berkowicz, D. Gershoni, G. Bahir, E. Lakin, D. Shilo, E. Zolotoyabko, A. C. Abare, S. P. Denbaars, and L. A. Coldren, *Phys. Rev. B* **61**, 10994 (2000).



# Confocal photoluminescence investigation on semi-polar (11-22) InGaN/GaN single quantum well overgrown on regularly arrayed micro-rods

---

Room temperature confocal photoluminescence (PL) measurements were performed on semi-polar (11-22) InGaN/GaN single quantum well (SQW) samples overgrown on regularly arrayed micro-rods to spatially investigate the optical properties of quantum well regions with and without basal stacking faults (BSFs). A periodic distribution of the BSF clusters in the active region leads to a periodic behaviour of the PL spectra across a large scanning area ( $80 \times 80 \mu\text{m}^2$ ). The PL spectrum from the quantum well region with high BSF density shows a strong low energy shoulder and consequently a long centre of mass (COM) wavelength, which is attributed to a higher indium composition around the BSF regions. The spatially periodic behaviour of the PL spectra becomes weaker in semi-polar samples with higher indium compositions, as a result of the suppression from the increasing indium fluctuation. Meanwhile, the emission intensity from the BSF regions is found to be slightly lower than that from the BSF-free regions, which is assigned to the non-radiative recombination centres within the BSF regions.

## 7.1 Introduction

Semi-polar and non-polar GaN-based light emitting diodes (LED) have been developed rapidly in the past decades owing to the advantages of reduced or eliminated piezoelectric fields in InGaN/GaN heterostructure.<sup>1,2</sup> The quantum confined Stark effect (QCSE) caused by the internal electrical fields can be effectively suppressed in the quantum wells grown along these directions.<sup>3</sup> Moreover, the semi-polar (11-22) surface is revealed to have a lower indium

chemical potential than other orientations, demonstrating an ability to incorporate more indium atoms into GaN crystal.<sup>4</sup> This allows for the growth of InGaN layers with higher indium content along semi-polar (11-22) orientation, and finally achieving high-performance InGaN-based emitters in the long wavelength region. However, despite a range of growth techniques applied, basal stacking faults (BSF), and associated partial dislocations are widely observed in semi-polar (11-22) orientated GaN heteroepitaxial films.<sup>5-8</sup> BSF can be considered as a quantum well structure in which one or more zinc-blende layers are embedded in the wurtzite matrix.<sup>9</sup> In semi-polar (11-22) bulk GaN film, the emission peak (3.29 ~ 3.42 eV) with an energy lower than the GaN bandgap is attributed to the BSF-related recombination.<sup>10,11</sup> Although BSFs act as radiative recombination centres, it is reported that the luminescence efficiency of the GaN films decreases with increasing the density of BSFs.<sup>12</sup> Recently, simulated emission was observed at room temperature on semi-polar (11-22) overgrowth GaN with a significant reduction in dislocation density, revealing the crucial role of dislocations in affecting the material optical performance. Here, we reported a spatially-resolved PL study on semi-polar (11-22) InGaN/GaN SQW samples overgrown on regularly arrayed micro-rods, to investigate the optical properties from the regions of quantum well intersected with BSFs and the regions free of BSFs.

A series of high-quality semi-polar (11-22) GaN on *r*-plane sapphire were overgrown on regularly arrayed micro-rod templates by metal organic chemical vapour deposition (MOCVD). The templates used for overgrowth have a micro-rod diameter of 4  $\mu\text{m}$  and a micro-rod spacing of 4  $\mu\text{m}$ . The overgrown (11-22) GaN layer exhibits a periodic distribution of BSF regions and BSF-free regions from previous TEM measurements.<sup>13</sup> An InGaN/GaN single quantum well was then grown on the (11-22) GaN layer followed by the growth of a 150 nm Mg-doped GaN layer. The quantum well growth temperature ranges from 780 to 756  $^{\circ}\text{C}$  to tune the emission wavelength of these (11-22) samples from 489 to 570 nm at room temperature. Confocal micro-PL measurements were carried out at room temperature using a 375 nm continuous wave laser diode as the excitation source. The laser was focused on the sample by a 100 $\times$  magnification objective with a 0.95 numerical aperture (NA). Sample emission is focused through a 10  $\mu\text{m}$  pinhole. The lateral spatial resolution of the confocal microscopy system is around 160 nm, which is significantly smaller than the width of BSF regions and the width of BSF-free regions ( $\sim 2$   $\mu\text{m}$ ). This is sufficient to map the difference in optical properties from

the regions with and without BSFs. Confocal PL maps were created by scanning  $80 \times 80 \mu\text{m}^2$  areas of the samples.

## 7.2 Results and discussion

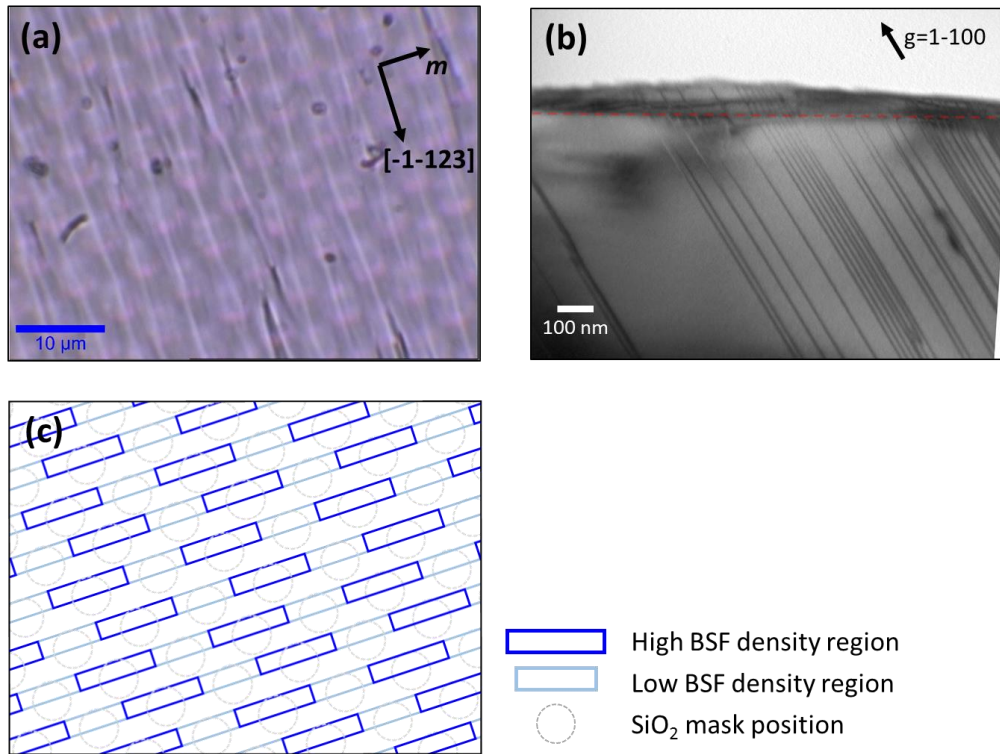


Figure 7.1: (a) Optical image of one semi-polar (11-22) InGaN/GaN SQW sample surface where the underlying micro-rods could be clearly observed. (b) Bright field TEM image showing the BSFs penetrating through the quantum wells in a semi-polar (11-22) InGaN/GaN MQWs sample. (c) A schematic diagram illustrating the periodic distribution of BSFs in the active region of our semi-polar (11-22) InGaN/GaN SQW samples.

Figure 7.1a shows an optical image of one semi-polar (11-22) InGaN/GaN SQW sample, where the underlying micro-rod arrays could be clearly observed. The fabricated micro-rods are regularly distributed along both the  $m$  direction and the  $[-1-123]$  direction with a period of  $8 \mu\text{m}$ . Striation-like features can also be found on the sample surface with an orientation opposite to the  $[-1-123]$  direction, which is due to the coalescence boundary between two growth fronts. Transmission electron microscopy (TEM) has discovered that there is a periodic distribution of BSF clusters in the surface of semi-polar (11-22) GaN using the micro-rod template

overgrowth approach.<sup>13</sup> Figure 7.1b presents a bright field TEM image of a semi-polar (11-22) InGaN/GaN sample with three quantum well layers. The image was taken along the [11-20] zone axis with a diffraction vector of 1-100, to observe the BSF distribution around the quantum well regions. The location of the InGaN/GaN quantum wells is marked by the red dash line, as the contrast of the quantum wells is very weak in this configuration. It is discovered that BSFs could penetrate through the quantum well regions and to the sample surface. As a result, the periodic distribution of the BSF clusters in the GaN film could be transferred to the InGaN/GaN quantum well region, forming areas of planar quantum well free from BSFs and areas of quantum well intersected with BSFs. Figure 7.1c illustrates a schematic diagram of the BSF distribution in the quantum well region viewed from top, where BSF stripes orientated along the *m*-direction are separated by BSF-free areas. For each BSF stripe, it consists of high and low BSF density regions. This allows us to investigate the optical properties of semi-polar (11-22) InGaN/GaN quantum well between the areas with and without BSF, and under identical growth conditions.

Figure 7.2a shows an integrated PL intensity map of the semi-polar (11-22) InGaN/GaN SQW sample with an emission wavelength of 489 nm. The scanning area is an  $80 \times 80 \mu\text{m}^2$  square, which is much larger than the size of the micro-rods ( $\sim 4 \mu\text{m}$  diameter). The light area represents the region with a strong emission intensity while the dark area corresponds to a weak emission. The integrated PL intensity map presents a regular distribution of light and dark stripes with orientation along the *m*-direction. The mean integrated intensity of the scanning area is  $3.8 \times 10^5$  CCD counts, but with a standard deviation of  $1.0 \times 10^5$  CCD counts. This large deviation is attributed to the uniformity in such a large scanning area, as the average PL intensity of the top left area is considerably larger than other areas.

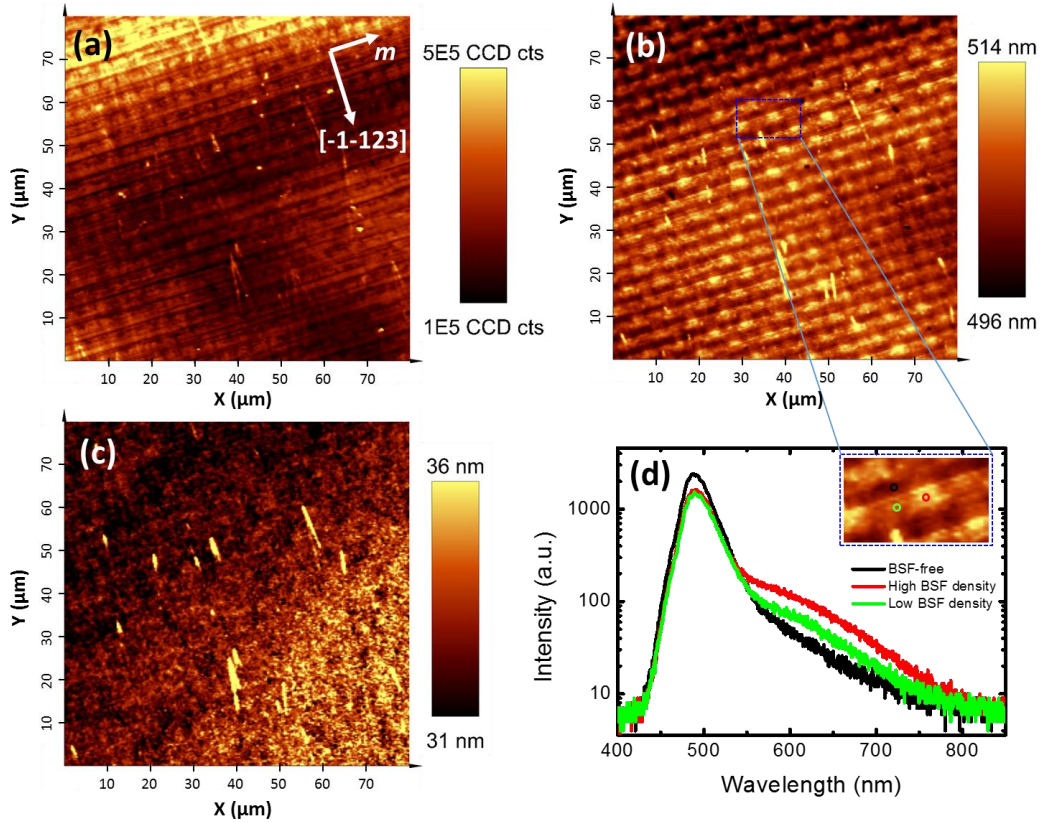


Figure 7.2: Maps of (a) integrated PL intensity, (b) COM wavelength and (c) FWHM of a semi-polar (11-22) InGaN/GaN SQW sample excited by a 375 nm laser at room temperature. (d) PL spectra from three typical regions as denoted by the coloured circles in insert.

Figure 7.2b shows a COM wavelength map of the same scanning area. In this map of weighted wavelength, one can find a periodic distribution of the light areas (long COM wavelength), which is similar to the distribution of high (or low) BSF density regions as showed in Figure 7.1c. The light areas, together with the medium light areas (medium COM wavelength) between them, form  $m$ -orientated stripes that are separated by the dark areas (short COM wavelength). The mean COM wavelength of this scanning area is 505.1 nm with a standard deviation of 4.4 nm. This periodic distribution of the COM wavelength matches the BSF distribution observed in our previous TEM study.<sup>13</sup> A long COM wavelength emission is supposed from the regions with a high BSF density, while a short COM wavelength emission is from the regions free of BSF. Figure 7.2d shows the PL spectra from three typical regions corresponding to long, medium and short COM wavelengths, as marked by the coloured circles in insert. The PL spectrum of the semi-polar sample exhibits an asymmetric shape with a

broadening low energy shoulder, which is also reported in the quantum wells along semi-polar and non-polar orientations.<sup>14,15</sup> Therefore, the COM wavelength (weighted wavelength) is slightly longer than the quantum well emission peak in the semi-polar (11-22) sample. The COM wavelengths are 512.0, 508.5 and 500.8 nm for the red, green and black circle regions, respectively.

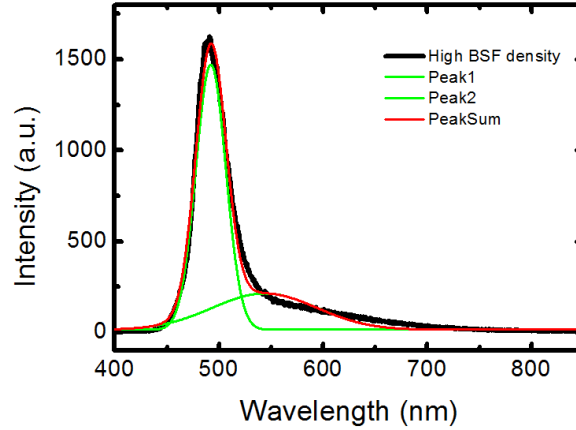


Figure 7.3: Two-peak fitting of a PL spectrum from the high BSF density area.

Two peaks could be observed by fitting the PL spectra with multiple peaks fitting, as shown in Figure 7.3. The intensity ratios between the long wavelength peak and short wavelength peak are 17% for the high BSF density region, and 11% for the low BSF density region. On the other hand, the PL spectrum from the BSF-free region cannot be fitted by the multiple peaks fitting, due to a low intensity of the low energy shoulder. The increase in the low energy shoulder is attributed to the appearance of BSFs in the quantum well regions.<sup>16</sup> Indium content around BSF region was reported to be larger than the surrounding region in InGaN/GaN quantum well structure, leading to a redshift in the emission spectrum.<sup>17</sup> As a consequence, emission spectrum from the region with a higher BSF density would exhibit a stronger low energy shoulder, and hence a longer COM wavelength. Furthermore, the emission spectrum is dominated by the peak from the quantum well, whose intensity is almost an order of magnitude higher than that of low energy shoulder. This means the full width at half maximum (FWHM) shows no strong correlation with the intensity of low energy shoulder in this (11-22) sample. Figure 7.2c shows the FWHM of the emission spectra from the same scanning area, where no periodic distribution is observed. The mean FWHM of the map is 32.8 nm with a standard deviation of 2.0 nm. Furthermore, the relatively low intensity of low energy shoulder reflects a low overall BSF density in the sample.

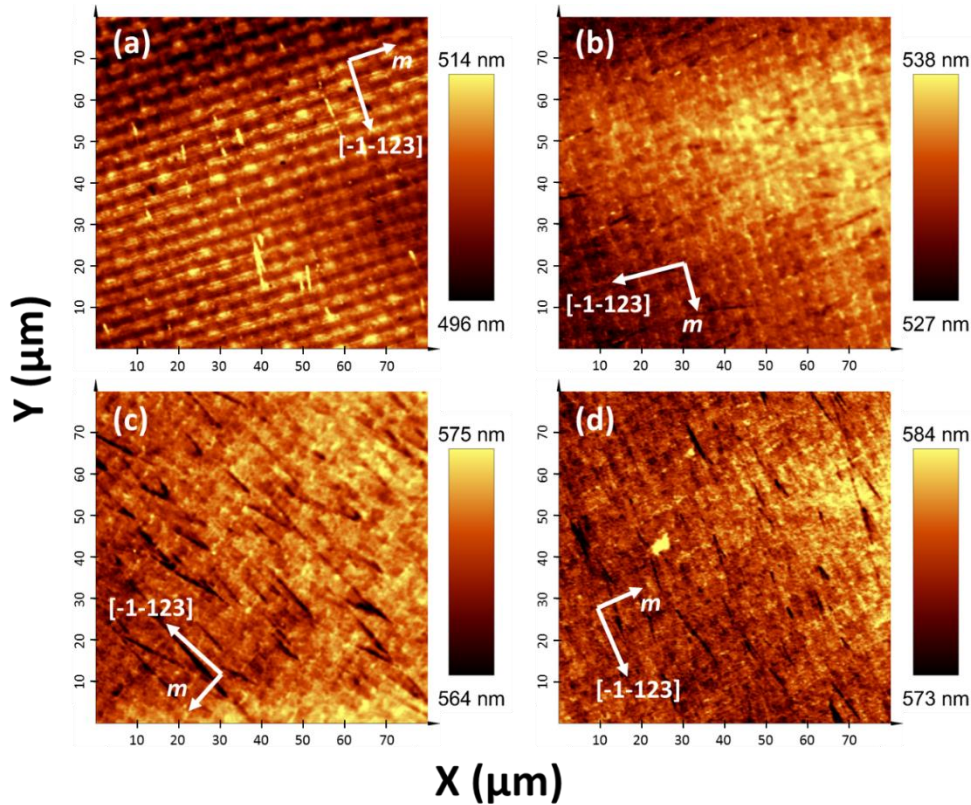


Figure 7.4: Maps of COM wavelength from semi-polar (11-22) InGaN/GaN SQW samples with different emission wavelengths.

The low energy shoulder in the PL spectra due to the indium fluctuations was further confirmed by confocal measurements on other semi-polar (11-22) InGaN/GaN SQW samples. Figure 7.4 (b)-(d) present the maps of COM wavelength from (11-22) SQW samples with emission peak wavelengths from 489 to 570 nm using the same scanning range. It can be found from the images that the periodic behaviour of the COM wavelength becomes weaker as the emission wavelength moves to longer wavelength. A large indium composition fluctuation is expected in high indium content quantum well, making the potential fluctuations within the BSF regions less pronounced. As a result of that, the difference in the PL lower energy shoulder between the BSF regions and BSF-free regions will be suppressed, resulting in a weak contrast in the COM wavelength.

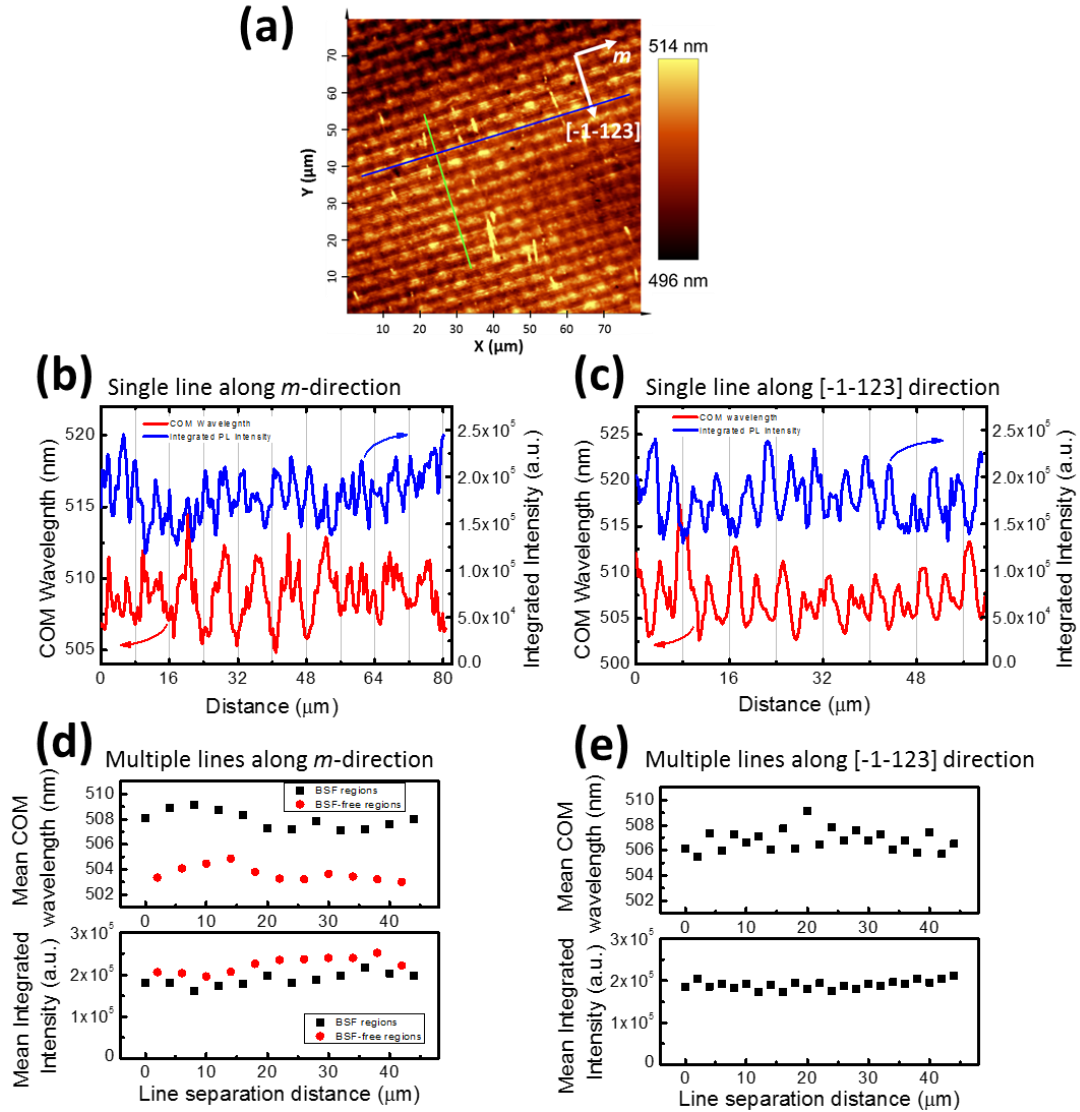


Figure 7.5: (a) PL spectra scanned along the *m*-direction (blue line) and the [-1-123] direction (green line). Profiles of COM wavelength and integrated PL intensity as a function of distance are plotted in (b) and (c) for single line scanning along the *m*-direction and the [-1-123] direction, respectively. The mean COM wavelength and mean integrated PL intensity of multiple scanning lines along the *m*-direction and the [-1-123] direction are plotted in (d) and (e), respectively.

Line scanning was also carried out on the 489 nm sample along the *m*-direction (blue line) and the [-1-123] direction (green line), as denoted in Figure 7.5a. For example, Figure 7.5b presents a COM wavelength (red line) a function of distance for a typical single line scanned along the *m*-direction and on BSF regions. The COM wavelength exhibits a periodic behaviour when it scans through the high and low BSF density regions. The period of COM wavelength

is 8  $\mu\text{m}$ , which is consistent with the period of high (or low) BSF density regions observed in TEM measurement. However, the integrated PL intensity (blue line in Figure 7.5b) changes faster than the COM wavelength, with an irregular distribution along the  $m$ -direction on the BSF regions. This weak correlation between the emission intensity and the BSF density reflects that BSFs in the quantum wells might not play an important role in lowering the emission intensity. The fluctuation in the emission intensity may be related to some non-radiative recombination centres within the BSF regions. The non-radiative recombination centres could be related to the dislocations that originate from three different mechanisms. Firstly, during the GaN overgrowth, threading dislocations could form around the coalescence boundary above the micro-rods and then propagate to the quantum well region.<sup>13</sup> Secondly, it is found that dislocations could be generated around the regions of quantum well intersected by BSFs.<sup>18</sup> Furthermore, partial dislocations bounding BSFs are discovered to have a random distribution within the BSF regions due to the random length of the BSFs.<sup>19</sup> All these make the location of non-radiative recombination centres less regular than that of BSFs, leading to a significant fluctuation in the integrated PL intensity with distance along the stripe. In contrast, for the scanning line along the  $[-1-123]$  direction (Figure 7.5c), both the COM wavelength and the integrated PL intensity show a clear periodic fluctuation against the distance, when scanning on the BSF regions and BSF-free regions. It can be found that each maximum of COM wavelength corresponds to a minimum in integrated PL intensity.

More lines were measured on the semi-polar sample along the  $m$ -direction with a separation of 2  $\mu\text{m}$ , with these multiple scanning lines located on BSF regions and BSF-free regions consecutively. As shown in Figure 7.5d, the mean COM wavelengths and mean integrated PL intensities show a clear difference between the quantum well with and without BSFs. Emission from BSF-free regions shows a low COM wavelength and slightly higher integrated PL intensity. However, for the scanning lines along the  $[-1-123]$  direction through BSF regions and BSF-free regions, both the mean COM wavelengths and mean integrated PL intensities exhibit a small fluctuation.

### 7.3 Summary

In conclusion, a correlation between the optical properties and BSF-regions in semi-polar (11-22) InGaN/GaN SQW has been investigated by confocal PL measurement at room temperature. Laterally periodic distributions of the COM wavelength and the integrated

intensity have been observed in the semi-polar (11-22) InGaN/GaN SQW that is overgrown on regularly arrayed micro-rod arrays. The regions of quantum well intersected by the BSFs exhibit an emission spectrum with a strong low energy shoulder, but with a slight decrease in integrated intensity. The low energy shoulder emission is attributed to the higher indium content around the BSFs, while the reduction in emission intensity is related to the non-radiative recombination centres within the BSF-regions.

## References

- 1 J. S. Speck and S. F. Chichibu, *MRS Bull.* **34**, 304 (2009)
- 2 T. Wang, *Semicond. Sci. Technol.* **31**, 093003 (2016).
- 3 T. Takeuchi, H. Amano, and I. Akasaki, *Jpn. J. Appl. Phys.* **39**, 413 (2000).
- 4 J. E. Northrup, *Appl. Phys. Lett.* **95**, 133107 (2009).
- 5 F. Tendille, M. Hugues, P. Vennéguès, M. Teisseire, and P. De Mierry, *Semicond. Sci. Technol.* **30**, 065001 (2015).
- 6 T. J. Baker, B. A. Haskell, F. Wu, J. S. Speck, and S. Nakamura, *Jpn. J. Appl. Phys.* **45**, L154 (2006).
- 7 B. Leung, Y. Zhang, C. D. Yerino, J. Han, Q. Sun, Z. Chen, S. Lester, K. Y. Liao, and Y. L. Li, *Semicond. Sci. Technol.* **27**, 024016 (2012).
- 8 T. Zhu, C. F. Johnston, M. J. Kappers, and R. A. Oliver, *J. Appl. Phys.* **108**, 83521 (2010).
- 9 P. P. Paskov, R. Schifano, B. Monemar, T. Paskova, S. Figge, and D. Hommel, *J. Appl. Phys.* **98**, 093519 (2005).
- 10 R. Liu, A. Bell, F. A. Ponce, C. Q. Chen, J. W. Yang, and M. A. Khan, *Appl. Phys. Lett.* **86**, 021908 (2005).
- 11 J. Lähnemann, U. Jahn, O. Brandt, T. Flissikowski, P. Dogan, and H. T. Grahn, *J. Phys. D. Appl. Phys.* **47**, 423001 (2014).
- 12 A. Y. Polyakov, N. B. Smirnov, A. V. Govorkov, H. Amano, S. J. Pearton, I. H. Lee, Q. Sun, J. Han, and S. Y. Karpov, *Appl. Phys. Lett.* **98**, 072104 (2011).
- 13 Y. Zhang, J. Bai, Y. Hou, R.M. Smith, X. Yu, Y. Gong, and T. Wang, *AIP Adv.* **6**, 25201 (2016).
- 14 M. D. Mensi, D. L. Becerra, R. Ivanov, S. Marcinkevičius, S. Nakamura, S. P. DenBaars, and J. S. Speck, *Opt. Mater. Express* **6**, 39 (2016).
- 15 T. Wernicke, L. Schade, C. Netzel, J. Rass, V. Hoffmann, S. Ploch, A. Knauer, M. Weyers, U. Schwarz, and M. Kneissl, *Semicond. Sci. Technol.* **27**, 024014 (2012).
- 16 D. Kundys, S. Schulz, F. Oehler, D. Sutherland, T. J. Badcock, P. Dawson, M. J. Kappers, R. A. Oliver, and C. J. Humphreys, *J. Appl. Phys.* **115**, 113106 (2014).
- 17 F. C. P. Massabuau, S. L. Sahonta, L. Trinh-Xuan, S. Rhode, T. J. Puchtler, M. J. Kappers, C. J. Humphreys, and R. A. Oliver, *Appl. Phys. Lett.* **101**, 212107 (2012).
- 18 Y. Huang, K. W. Sun, A. M. Fischer, Q. Y. Wei, R. Juday, F. A. Ponce, R. Kato, and T. Yokogawa, *Appl. Phys. Lett.* **98**, 261914 (2011).

- 19 Y. Zhang, J. Bai, Y. Hou, X. Yu, Y. Gong, R. M. Smith, and T. Wang, *Appl. Phys. Lett.* **109**, 241906 (2016).

## Summary and future work

---

### 8.1 Summary

This thesis has presented an investigation on defect reduction in semi-polar (11-22) GaN overgrown on regularly arrayed micro-rods by MOCVD, and the influence of the micro-rod sizes on crystal quality. Owing to the optimization of growth conditions and template fabrication, it has achieved a series of high quality semi-polar (11-22) GaN films with the lowest dislocation density of  $2.0 \times 10^8 \text{ cm}^{-2}$ . It also presents a study on the optical property of semi-polar (11-22) InGaN/GaN quantum well overgrown on micro-rod templates, demonstrating the advantages of semi-polar (11-22) orientation for long wavelength emitters.

The micro-rod template used for overgrowth is fabricated using a combination of industry-matched photolithography and dry-etching techniques. It is found that the micro-rod arrays with a specially designed pattern effectively resolve the challenge of anisotropic growth rate in conventional overgrowth technique for semi-polar GaN. TEM characterization technique was employed to investigate the defect reduction in the overgrown semi-polar (11-22) GaN. It is discovered that most of the dislocations are blocked either by the SiO<sub>2</sub> masks, or the coalescence processes due to a faster growth rate along the *c*-direction than that along the *a*-direction. In addition, BSFs tend to expand within the basal plane, propagating with a component parallel to the *m*-direction. After the second coalescence over the SiO<sub>2</sub> masks, BSF stripes are regularly separated by defect-free regions along the [-1-123] direction, with each stripe consisting of high and low BSF density clusters in a periodic distribution along the *m*-direction. Based on this study, a defect reduction model has been used to evaluate the defect density in overgrown films with different designs of the micro-patterning.

For our micro-rod template overgrowth technique, micro-rod diameter plays a vital role in effectively reducing both the dislocation density and the BSF density of the overgrown (11-22) GaN, but in different ways. The PL intensity ratio of NBE emission to BSF related emission exhibits a monotonic increase with increasing the micro-rod diameter. TEM

measurements further confirm this reduction in BSF density in the samples overgrown large micro-rods. In contrast, the dislocation density reduces significantly when the micro-rod diameter increases from 2 to 4  $\mu\text{m}$ , and then starts to increase when the diameter further increases to 5  $\mu\text{m}$ . The XRD measurements demonstrate that the best crystal quality of the overgrown (11-22) GaN is achieved by an overgrowth on micro-rods with a 4  $\mu\text{m}$  diameter and a 0.4  $\mu\text{m}$  height, leading to the achievement of stimulated emission in semi-polar (11-22) GaN at room temperature.

A systematic study was carried out on the Stokes shift of semi-polar (11-22) InGaN/GaN MQWs with a wide spectral range from green to yellow by means of both PLE and TRPL measurements in comparison with their *c*-plane counterparts. Semi-polar InGaN/GaN MQWs samples show a lower Stokes shift than their *c*-plane counterparts. The Stokes shift values for both the semi-polar samples and their counterparts exhibit a linear relationship with their emission energy, and semi-polar samples show a reduced gradient in the fitted curve. TRPL measurements reveal that the semi-polar samples display a significant reduction in piezoelectric fields in comparison with their *c*-plane counterparts. Meanwhile, there exists a large exciton localization in semi-polar samples, which is attributed to the increasing indium fluctuation in high indium content. All these demonstrate that the piezoelectric fields induced polarization is the major mechanism for causing the large Stokes shift in conventional *c*-plane InGaN/GaN MQWs samples. The presented results contribute to a better understanding of the long standing issue on the mechanism for the large Stokes shift.

Confocal PL measurements have been performed on semi-polar (11-22) InGaN/GaN SQW samples overgrown on micro-rod templates to spatially investigate the optical properties of quantum well regions with and without BSFs. The PL spectrum from the BSF regions exhibits a strong low energy shoulder, which is related to a higher indium composition around the BSF regions. A slight decrease in emission intensity is attributed to the non-radiative recombination centres within the BSF regions. It is suggested that compared with dislocations, BSFs might not play a crucial role in lowering the emission intensity of semi-polar (11-22) InGaN/GaN SQW.

## 8.2 Future work

### 8.2.1 Defect reduction in non-polar $a$ -plane GaN overgrown on regularly arrayed micro-rod template

Much attention have been paid to non-polar orientation, due to its advantage of eliminated piezoelectric fields in InGaN/GaN heterostructures. Using photolithography and dry-etching techniques, regularly arrayed micro-rod template can be fabricated from  $a$ -plane GaN that directly grows on  $r$ -plane sapphire. The template is then put back into MOCVD chamber to carry out the overgrow process. It is essential to understand the defect reduction in overgrown  $a$ -plane GaN to further improve the crystal quality.

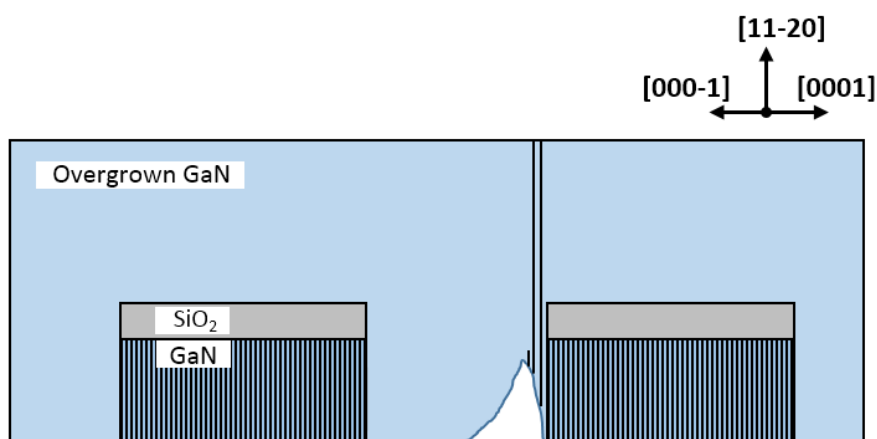


Figure 8.1: Schematic diagram of the non-polar  $a$ -plane GaN overgrown on micro-rod template.

For non-polar  $[11-20]$  orientation, basal plane of GaN crystal is perpendicular to the growth plane. Overgrowth starts from the micro-rod sidewalls along  $+c$  and  $-c$  directions. As the  $+c$  direction growth leads to defect free region, it is necessary to favouring the growth along the  $+c$  direction, which is easy to be achieved in practice. In that case, most of the dislocations existing in the GaN micro-rods are supposed to be blocked by the SiO<sub>2</sub> layer deposited on top, and few dislocations from the  $-c$  direction growth could probably propagate to sample surface. Meanwhile, further work is required in optimizing the template design and the second coalescence above the SiO<sub>2</sub> layer to reduce the BSF density, since BSFs tend to propagate with a component parallel to the  $m$ -direction.

## 8.2.2 Optical characterization of semi-polar (11-22) InGaN/GaN single quantum well by using a novel nano-patterning approach

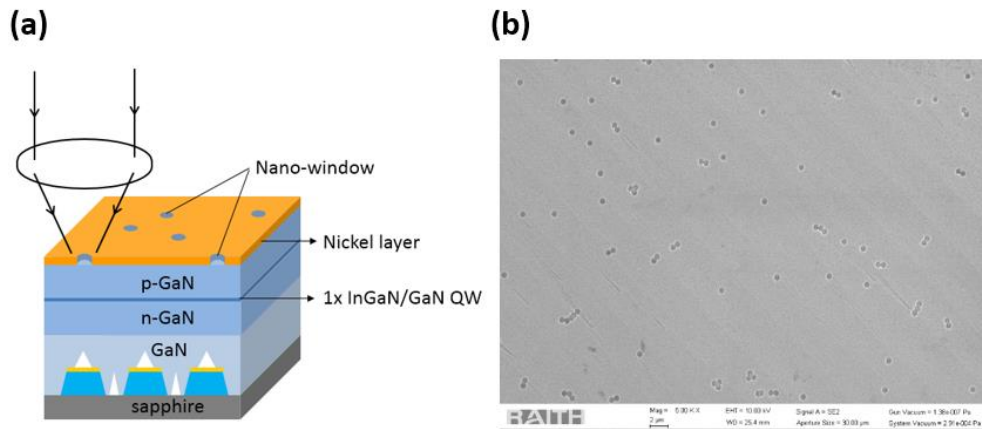


Figure 8.2: (a) Schematic of semi-polar (11-22) InGaN SQW with nano-windows on surface; (b) Top-view SEM image of one sample showing the randomly distributed nano-windows.

It has developed a novel nano-patterning approach, which allows us to fabricate a number of individual areas which are smaller than the areas of either any BSF free regions or any BSF-containing region. Based on this approach, we have carried out a systematic study of the optical properties of the semi-polar (11-22) InGaN single quantum well (SQW) structures on the overgrown GaN in order to study the influence of BSF on optical properties of the semi-polar InGaN SQW. A series of semi-polar (11-22) InGaN/GaN SQW LED structures with an emission wavelength from blue to yellow have been grown on our GaN. As shown in Figure 8.2a, a number of nano-windows are fabricated by randomly spin-coating nanosphere silica particles with a diameter of 500 nm on the surface of each sample, followed by depositing a nickel layer. After that, the nanosphere particles are removed, leaving a number of sparsely distributed nano-windows with a diameter of 500 nm. As presented in Figure 8.2b, both the nano-windows and the spacing of the nano-windows are randomly distributed. The separations of these nano-windows are large enough, allowing us to perform optical measurements on the SQW within such a nano-window area by using our micro-photoluminescence system equipment. An optical study is based on a large number of measurements on these individual nano-windows, where some nano-windows are on the BSF free regions, and some on BSF-containing regions. The results measured at room temperature have not shown significant difference, meaning that unlike dislocation which generally acts as non-radiative

recombination centre BSF might not play an important role in the optical performance of semi-polar InGaN SQW. Further investigation to understand the influence of BSF on exciton dynamics at a low temperature is on-going, demonstrating a completely different role to dislocations.



# Abbreviations

---

<b>AlGaN</b>	Aluminium gallium nitride	<b>RIE</b>	Reactive ion etching
<b>AlN</b>	Aluminium nitride	<b>RT</b>	Room temperature
<b>APD</b>	Avalanche photodiode	<b>SEM</b>	Scanning electron microscopy
<b>BSF</b>	Basal stacking fault	<b>SAED</b>	Selective area electron diffraction
<b>COM</b>	Centre of mass	<b>Si</b>	Silicon
<b>CCD</b>	Charge-coupled device	<b>SiC</b>	Silicon carbide
<b>ELOG</b>	Epitaxial lateral overgrowth	<b>SiO<sub>2</sub></b>	Silicon dioxide
<b>EQE</b>	External quantum efficiency	<b>SQW</b>	Single quantum well
<b>FWHM</b>	Full width at half maximum	<b>TD</b>	Threading dislocations
<b>GaN</b>	Gallium nitride	<b>TCSPC</b>	Time-correlated single photon counting
<b>HVPE</b>	Hydride vapour phase epitaxy	<b>TRPL</b>	Time-resolved photoluminescence
<b>InGaN</b>	Indium gallium nitride	<b>TEM</b>	Transmission electron microscope
<b>InN</b>	Indium nitride	<b>XRD</b>	X-ray diffraction
<b>ICP</b>	Inductively coupled plasma		
<b>IRF</b>	Instrument response function		
<b>IQE</b>	Internal quantum efficiency		
<b>LD</b>	Laser diode		
<b>LED</b>	Light-emitting diode		
<b>LT</b>	Low temperature		
<b>MOCVD</b>	Metal organic chemical vapour deposition		
<b>MBE</b>	Molecular beam epitaxy		
<b>MQW</b>	Multiple quantum well		
<b>NBE</b>	Near band edge		
<b>NA</b>	Numerical aperture		
<b>PD</b>	Partial dislocation		
<b>PMT</b>	Photocathode photomultiplier tube		
<b>PL</b>	Photoluminescence		
<b>PLE</b>	Photoluminescence excitation		
<b>PECVD</b>	Plasma enhanced chemical vapour deposition		
<b>PSF</b>	Prismatic stacking fault		
<b>PLD</b>	Pulsed laser deposition		
<b>QCSE</b>	Quantum confined stark effect		



# Acknowledgements

---

It is delightful to write the acknowledgement, as it is the last part of this thesis. At this moment, I would like to take this opportunity to express my sincere gratitude to the people who have helped me in completing this research project.

First and foremost, I would like to thank my supervisor, Professor Tao Wang. Without his support, I would not have the chance to pursue my PhD degree here in Sheffield. He spent a lot of time with me in discussing my research plan, experimental results and manuscript writing, guiding me to carry out my research project. Lots of time, I was convinced by his broad knowledge and physical insights on research work. I also gained many opportunities in our III-nitride group to develop the academic skills. He encouraged me to read more and think critically. I cannot forget the academic and life experiences that he kindly shared with me, which are so interesting and meaningful.

I wish to thank Dr. Jie Bai for the training of specimen preparation and TEM operation, as well as the fruitful discussion. My gratitude also goes to Dr. Rick Smith for his enormous help and training in optical characterization instruments, and lengthy discussions on my research project. I would be always thankful to Dr. Yaonan Hou for providing valuable comments and suggestion on my research. I would like to thank Dr. Modestos Athanasiou for his kind assistance in fabrication and optical characterization.

I would like to acknowledge Dr. Yipin Gong and Dr. Xiang Yu for providing the samples for me to carry on my project. I also like to thank other people in the growth team: Dr. Benbo Xu, Dr. Kun Xing, Mr. Zhi Li, Mr. Ling Jiu, Dr. Liancheng Wang, Mr. Shuoheng Shen, Mr. Xuanming Zhao, for their kind help and discussion.

I am grateful for all of the trainings and assistance from the staff in the III-V national centre and the Sorby Centre.

Finally, I would like to thank my parents for their constant support, and also my wife, who quitted her job in China and came here to support me to finish my study. She and my little daughter have brought me a lot of happiness and joy in my life.